NOVEL CONCEPTS IN HIGH POWER SEMICONDUCTOR LASERS

A DISSERTATION SUBMITTED TO
THE GRADUATE SCHOOL OF ENGINEERING AND SCIENCE
OF BILKENT UNIVERSITY
IN PARTIAL FULFILLMENT OF THE REQUIREMENTS FOR
THE DEGREE OF
DOCTOR OF PHILOSOPHY
IN
PHYSICS

By
Seval Arslan
November 2018

Novel concepts in high power semiconductor lasers
By Seval Arslan
November 2018

We certify that we have read this dissertation and that in our opinion it is fully adequate, in scope and in quality, as a dissertation for the degree of Doctor of Philosophy.

Oğuz Gülseren(Advisor)

Atilla Aydınlı (Co-Advisor)

Ceyhun Bulutay

Raşit Turan

Alpan Bek

Onur Tokel

Approved for the Graduate School of Engineering and Science:

Ezhan Karaşan
Director of the Graduate School

ABSTRACT

NOVEL CONCEPTS IN HIGH POWER SEMICONDUCTOR LASERS

Seval Arslan
Ph.D. in Physics
Advisor: Oğuz Gülseren
Co-Advisor: Atilla Aydınlı
November 2018

This doctoral thesis deals with innovations to the cavity optics of high power semiconductor lasers emitting light at 9xx nm. High power laser diodes are complex electronic and photonic systems. Developments in epitaxial crystal growth techniques and the quality that ensued has been the driving force in the progress of the field. Semiconductor lasers with high output powers and high efficiencies have thus become possible. Commercial single emitters each with over 10 watts output with efficiencies reaching 60% is available.Even higher output powers have been demonstrated in the lab. High power semiconductor lasers have many applications such as acting as optical pumps in other lasers, range finding, optical storage, light sources in sensors and medical tools. The demand for higher powers and efficiencies continues. Among several possibilities, one of the main limits of maximum output power is the catastrophic optical mirror damage (COMD). At high pump currents and hence output powers, facet absorption leads to temperatures high enough to damage the cavity mirrors. This thesis is focused on novel approaches to increase the COMD threshold. We demonstrate design, fabrication and characterization of the high power strained InGaAs/AlGaAs lasers emitting light at 9xx nm. To prevent facet absorption which decreases the laser efficiency especially at high injection currents, band gaps in the vicinity of the laser facet are increased using impurity-free vacancy disordering (IFVD) while preserving the band gap in the lasing region away from the facets. A record large bandgap at the facet region, relative to that of the lasing region is achieved by thermal stress management of a bilayer dielectric structure. We demonstrate excellent optical loss and optical power output with this bilayer approach. Further, positive feedback cycle during absorption at the facets is broken by keeping the facets cold, by design. Thus, in this cold window approach, we extend the passive unpumped windows to keep the heat source from the main body of the cavity away from the facets while eliminating the additional loss incurred by biasing

this section to transparency. This new biased window approach leads to much cooler facet temperatures while reducing the bulk temperatures as well. Thus, we use thermoreflectance spectroscopy to measure facet temperature as a function of pump and bias current. We clearly demonstrate that, for the first time, facet temperatures have been decreased below the bulk temperature without penalty on the output power.

Keywords: High power diode lasers, semiconductor lasers.

ÖZET

YÜKSEK GÜÇLÜ YARIİLETKEN LAZERLERDE YENİ KAVRAMLAR

Seval Arslan
Fizik Bölümü, Doktora
Tez Danışmanı: Oğuz Gülseren
İkinci Tez Danışmanı: Atilla Aydınlı
Kasım 2018

Bu doktora tezi, 9xx nm'de ışık yayan yüksek güçlü yarıiletken lazerlerinin kovuk optiklerine yönelik yeniliklerle ilgilidir. Yüksek güçlü lazer diyotları karmaşık elektronik ve fotonik sistemlerdir. Kristal büyütme tekniklerindeki gelişmeler ve ortaya çıkan yüksek kalitedeki epitaksiyel kristaller, alanın ilerleyişinde itici güç olmuştur. Bu kristallerle yapılan lazerler yüksek güç ve yüksek verim göstermektedirler. Ticari olarak satılan tek emitörlerin her birinden 10 Watt'ın üzerinde yüksek çıkış gücü ve %60'a varan verimlilikler gösterilmiştir. Laboratuvarlarda daha yüksek güçler de elde edilmiştir.

Yüksek güçlü yarıiletken lazerler, diğer lazerlerde optik pompalar, telemetre bulma, optik depolama, sensörlerde ışık kaynakları ve medikal aletler gibi birçok uygulamaya sahiptir. Daha yüksek güç ve verimlilik talebi devam ediyor. Birkaç olasılık arasında, maksimum çıkış gücünün ana limitlerinden biri katastrofik optik ayna hasarıdır (COMD). Yüksek pompa akımlarında ve dolayısıyla çıkış güçlerinde faset soğurması, kovuk aynalarına zarar verebilecek kadar yüksek sıcaklıklara yol açar. Bu tez, COMD eşiğini artırmak için yeni yaklaşımlara odaklanmıştır. Nitekim, bu tezde 9xx nm'de ışık yayan yüksek güçlü gerilmiş InGaAs / AlGaAs lazerlerinin tasarımı, üretimi ve karakterizasyonunu göstermekteyiz. Lazer verimliliğini özellikle yüksek enjeksiyon akımlarında azaltan faset soğurmasını önlemek için, ışıma bölgesinde korunurken, lazer fasetinin çevresindeki yasak bant aralığı safsızlıksız atomları kullanmaksızın boşluk düzensizliği (IFVD) kullanılarak arttırılır. İki bölgeli bir dielektrik yapının ısıl stres yönetimi ile faset bölgesinde, ışıma bölgesine göre varolan en yüksek bant aralığı elde edilir.Bu iki katmanlı yaklaşımla mükemmel optik kayıp ve optik güç çıkışı gösteririz. Ayrıca, fasetlerde soğurma sırasında olumlu geribildirim döngüsü, fasetleri tasarımla soğuk tutarak kırılır. Bu nedenle, bu soğuk pencere

yaklaşımında, ısı kaynağını kovuğun ana gövdesinden uzak tutmak için pasif pompalanmamış pencereleri uzatıp, bu bölümün geçirgen hale getirerek meydana gelen ek kayıpları ortadan kaldırıyoruz.Bu yeni ileri besleme altındaki pencere yaklaşımı, yığın sıcaklıklarını da azaltırken çok daha düşük faset sıcaklıklarına yol açar. Böylece, pompa ve ileri besleme akımının bir fonksiyonu olarak faset sıcaklığını ölçmek için termoyansıma (thermoreflectance) spektroskopisini kullanıyoruz. İlk kez, çıkış sıcaklıklarında düşüş olmadan faset sıcaklıklarının kütle sıcaklığının altına düştüğünü açıkça gösterdik.

Anahtar sözcükler: Yüksek güçlü diyot lazerler, Yarıiletken lazerler.

Acknowledgement

First of all, I would like to express my special thanks to Prof. Dr. Atilla Aydınlı for giving me a chance to carry out my Ph.D. on laser diodes. He has extensive knowledge and experience of semiconductors and has always tried to convey them to me. With his valued advice, he gave me the courage to accomplish the tough work.

I am sincerely grateful to my advisor and the head of the Department of Physics, Prof. Dr. Oğuz Gülseren for his support during my Ph.D.

I would like to thank Prof. Dr. Ceyhun Bulutay, Prof. Dr. Raşit Turan, Assoc. Prof. Dr. Alpan Bek and Asst. Prof. Dr. Onur Tokel for reviewing my thesis and sharing their valuable comments.

It is a pleasure to acknowledge Dr. Abdullah Demir for permanent availability for scientific discussions. I am grateful for his support during my studies with his practical ideas.

My warm gratitude belongs to Sinan Gündoğdu for the supporting me during many aspects of laser testing and analysis. He also provided a very fruitful discussion environment. Hard times got cheerful thanks to his friendship.

I would like to warmly thank my dear friend Seval Şahin for her support in laser processing. Besides the help in laboratory work, my good friend Seval always made me feel special.

I would like take this opportunity to thank my friends, Ali Murat Sözen, Rahim Bahari, Berk Berkan Turgut, Muhammet Genç, Seda Arpacı, Mustafa Elçi, Fatih Bilge Atar, Doğukan Apaydın and Enes Seker for a warm and cheerful. atmosphere.

I sincerely thank Murat Güre and Ergün Karaman and Elvan Öğün for their constant administrative and technical support.

I would like to acknowledge financial support of ERMAKSAN A. Ş. which made this study possible.

A very special word of thanks goes to my parents. They have always encouraged me to finish my doctorate in the best way possible. I am grateful to both for a lifetime of support and love.

The last gratitude goes for my husband, Eray who supported me faithfully

during the Ph.D. years. He has been very patient and made me feel special by showing how proud he is with me. Thank you honey.

Contents

List of Figures

List of Tables

Chapter 1

Introduction

The word laser (light amplification by stimulated emission of radiation) was first used by Gordon Gould and experimentally demonstrated by Theodore Maiman in 1960 [1]. In contrast with the ruby laser of Maiman, semiconductor diode lasers are electrically pumped solid state lasers and they are highly preferred for many applications such as communications, material processing, medical, lithography due to their compactness and higher efficiency compared to the other types of lasers. Diode laser technology accelerated after the development of metal organic chemical vapor deposition (MOCVD) and molecular beam epitaxy (MBE) crystal growth technologies which allow the deposition of semiconductors with different compositions on top of one another. The ability to grow many different compositions and thicknesses can be exploited to engineer the band gap of each layer and build novel devices [1, 2].

Laser performance is evaluated in terms of wavelength tunability, diffraction limited high beam quality, high optical output power and long term reliability. These operational characteristics of laser diodes are based on the electronic and optical design as well as suitable fabrication technology and high quality crystal growth. Laser diodes are characterized by voltage-current-optical output power measurements. Bias voltage injects electrical carriers into the laser making it necessary to understand their transport. In response to the injected current,

coherent photons are generated by recombination in the presence of optical fields, which points to the necessity of understanding the optical fields inside the cavity.

The emission wavelength of the band to band recombination lasers depends on the band-gap of the active region material [3, 2]. In the case of lasers that depend on quantum well(s) for the emitted light, emission wavelength is determined by the lowest bound states in the conduction and valence bands of the quantum well(s).The material system of a semiconductor laser should consist of layers that are lattice matched for defect free laser epitaxy since defects are non-radiative recombination centers decreasing the laser's internal quantum efficiency. However, the laser emission wavelength in the range of 900-1100 nm in the AlGaAs/InGaAs quantum well structures can not be covered by a lattice matched layer system. This range of emission can be covered by the strained-layer system of $In_xGa_{1-x}As/Al_yGa_{1-y}As$ or $In_xGa_{1-x}As/GaAs$ epitaxy by adjusting the thickness and composition of the InGaAs quantum well. [2, 4]. The misfit locations that may arise in these strained layer systems do not have significant detrimental effects on laser performance [2].

The electro-optical design which determines the emission wavelength as well as the transverse lateral and the vertical confinement, affects the efficiency of high power diode lasers. The first diode lasers had a homo-junction design. A homo-junction consists of n- and p- doping of the same semiconductor material. However, the threshold of the homo-junction lasers are very high due to the low mode overlap between the active region and mode. In these lasers there is no mode confinement in the transverse direction, therefore the mode spreads into the highly doped claddings leading to free carrier absorption. Hence, the efficiency of the homo-junction lasers is very low and it works under pulsed bias due to heating problems. The double heterostructure diode lasers show better performance compared to the homo-junction lasers. As the name implies, double heterostructure consists of thin layers of smaller bandgap (higher index) semiconductor material sandwiched between the thicker n- and p- type larger bandgap (lower index) semiconductor materials. The active layer thickness in these lasers are typically is in the range of 0.1 to 0.2 μm [2]. These structures enable carrier confinement in the thin active layer under forward bias conditions, which

force the carriers to recombine in the active region. Furthermore, the index difference between the active layer and the cladding provides mode confinement in the active layer, hence the mode overlap with active layer increases, and the gain threshold decreases. In addition, mode confinement prevents mode spreading into the cladding layers. Thus, absorption loss due to free carriers in the doped cladding layers is eliminated. As a result, the threshold current density is much lower compared to that of the homo-junction lasers. When the active layer thickness is reduced, the carrier confinement and mode overlap decreases leading to an increase in the threshold. However, very thin active layers with thicknesses in the range of de Broglie wavelength shows quantum size effects, and single or multi quantum well (QW) laser performs significantly improved results. The staircase like density of electronic states instead of parabolic density of states as in the double-heterostructures and small active volume are the reasons for the low threshold current density of QW lasers. The difference between the density of states of the bulk and QW material changes the gain curve. The gain curve of bulk material is wide and highly energy dependent whereas QW lasers have narrow gain curves due to the high density of states around ground states. As a result, lower number of carriers are needed for population inversion and the spectral shift due to the band filling effect is very low compared to the bulk material. To increase the carrier and photon confinement in QW lasers, the graded refractive index separate-confinement heterostructure (GRIN-SCH) is used. GRIN-SCH structure consists of single or multiple QWs sandwiched between the graded lower index and higher bandgap semiconductor surrounded yet by lower index and higher bandgap cladding. This approach provides carriers confinement in QW and mode confinement within the SCH region which prevents the free carrier absorption loss due to the highly doped cladding layers.

For the edge emitting diode lasers, transverse lateral current and photon confinement can be achieved by weak index guiding mechanism as in the ridge waveguide lasers. Ridge is formed by etching the laser structure down to the cladding layer and deposition of a dielectric layer next to the edge of the ridge prevent current loss through leakage. Photons are confined in the lateral direction due

to the index step. The lateral single mode operation is crucial for many applications. Therefore, the ridge width and height, and active region thickness should be carefully adjusted for single mode operation. Narrow ridge waveguide lasers are highly preferred for many applications because of low optical losses and thresholds, ease of fabrication and high optical output power in single lateral mode.

Generally speaking, the laser's with an output power larger than 1W is labeled as high power diode lasers [2]. Increasing the output power of semiconductor diode lasers have opened up new application areas such as optical fiber amplifier pumping and material processing which also necessitates the improvement of laser performance. The main factors that limit power output of semiconductor lasers are carrier leakage, gain saturation leading to spatial hole burning (SHB), free carrier absorption, catastrophic optical damage (COD) and catastrophic optical mirror damage (COMD) [5, 6, 7]. There are two reasons for the carrier leakage. First, is the carrier overflow from the active layer. Carriers diffuse without being captured by the quantum well(s) due to the finite diffusion time of the carriers. This effect can be seen even at threshold and increases with current [8]. Second, is the finite relaxation time of the carriers in the quantum well(s) [9]. Electrons and holes leak to the waveguide from the quantum well without contributing to the stimulated recombination. Carrier leakage leads to optical losses via radiative or non-radiative recombination. It can be reduced using the MQWs in the active region [7, 10] as well as eletcron or hole barriers strategically placed in the active region. Spatial hole burning becomes dominant under high power densities. In this condition, the stimulated emission due to the high photon density reduces the local gain because it removes the carriers contributing to the gain. The spatial hole burning (SHB) is a complicated phenomenon and has been studied by many researchers in more detail in refs [11, 12]. This effect can be minimized by reducing confinement factor with vertical designs [7]. COMD and COD are irreversable processes which occur on the laser facets and in the bulk of the laser cavity due to the strong heating caused by high optical power density and non-radiative recombination. Optical power density can be reduced by reducing the mode confinement factor. COMD threshold can also be increased by making

proper surface passivation of the facets or using quantum well intermixing (QWI) techniques. Surface passivation aims to reduce or stabilize the surface states against thermodynamically unstable species such as arsenic, arsenic oxides and adsorbed water [13]. QWI is used to increase the bandgap in the proximity of the laser facet while keeping the rest of the cavity at the original band gap. Increasing the band gap decreases the facet absorption and facet temperature. However, there has, so far, been no way to decrease facet temperature below the bulk temperature.

This thesis concentrates on novel approaches to increase reliable optical output power from InGaAs based high power laser diodes. It covers three main sections; In the Chapter on fundamentals of diode lasers, we summarize the concepts of diode lasers with Fabry-Perot resonators and we examine the electro-optical and thermal properties of the diode lasers. The relation between the physical properties and measurable quantities are given. In the experimental chapter, we describe cavity design, laser fabrication techniques and electro-optical, beam divergence and thermal characterization techniques and measurement set-ups for these characterizations. The pulsed and continuous wave (cw) electro-optical characterization set-ups are shown. There are many ways to measure facet temperature of the diode lasers such as photoluminescence, micro-Raman spectroscopy and thermoreflectance [14, 15, 16]. We built a thermoreflectance measurement set-up to determine facet temperatures. This technique allows us high spatial and temperature resolution. The vertical and lateral beam divergence of the standard high power diode lasers were measured using a galvo-mirror system for the first time. The advantage of this system is the ability to measure both vertical and lateral divergence angles at the same time. Furthermore, the electro-optical and thermal characterization results of the conventional high power laser diodes are also given in this chapter. In the Chapter devoted to the novel concepts for cavity optics, we study the impurity free vacancy disordering (IFVD) technique, which provides facet temperature reduction and higher catastrophic optical mirror damage threshold (COMD). With the IFVD technique, the facet absorption rate is decreased by large bandgap in the proximity of the laser facet. The reliability of the high power diode lasers is correlated with the bandgap difference between the

intermixed and suppressed regions [17]. We enlarged the bandgap in the vicinity of the laser facet using SiO_2 and preserved the pumped region using a bilayer dielectric structure optimized with stress management. We obtained record high bandgap difference between the lasing and mirror region.The comparison of the photoluminescence and surface quality measurements based on the optical microscopy and atomic force microscopy (AFM) results of single layer and bilayer structure was made. The electro-optical characterization of the lasers with and without IFVD process were done. The novel long biased window approach was used to reduce facet temperature. For the first time, facet temperature was reduced down to the bulk temperature. The COMSOL heat transfer model was used to show facet temperature reduction in biased window lasers. The comparison of the electro-optical and thermal properties of the conventional and biased window lasers was done.

Chapter 2

Fundamentals of diode lasers

This chapter summarizes theoretical background of the electro-optical characteristics of the high power laser diodes. The basic diode laser concept is introduced in section 2.1. Section 2.2 explains the operating models of the diode lasers starting from the carrier injection and ending with photon generation. Then, optical loss, threshold and gain mechanisms for Fabry-Perot lasers are presented and followed by current dependent optical output characteristics. In section 2.3, thermal characteristics and their effects on laser performance is presented. Last section describes the lateral and far-field divergence characteristics of the laser diodes.

2.1 Basic diode laser concept

A diode laser consists of an active region sandwiched between p-n or p-i-n junction. Diode lasers are pumped electrically and optical gain is obtained by the stimulated emission due to population inversion under high carrier injection. Emitted light is amplified, instead of being absorbed, during stimulated emission process and propagates along the optical wave guide and partially reflected from the cavity facet (the so called Fabry-Perot resonator) which experiences both loss and gain. Fabry- Perot resonator is needed for positive feedback for lasing and it can

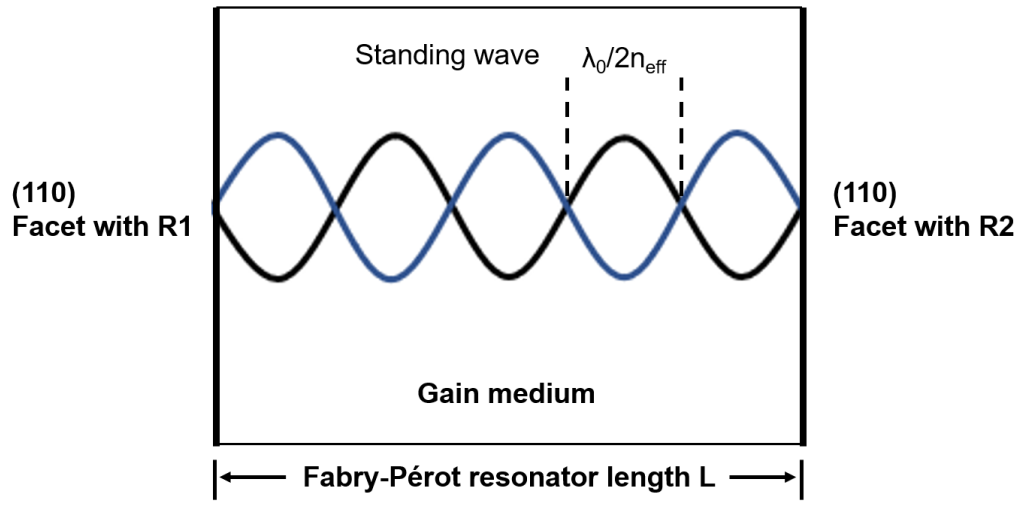

Figure 2.1: The schematic illustration of the Fabry-Perot resonator

be constructed by cleaving the crystal perpendicular to the cavity from the two ends, for edge emitting laser diodes. A schematic illustration of the Fabry-Perot resonator is given in figure 2.1. Even uncoated laser facets can act as resonator mirrors. However, the front and rear mirrors are typically coated to have low and high reflectivity, respectively, to increase laser performance. Generated light lases in the form of optical modes which can be thought as superposition of plane waves propagating inside the cavity and bouncing back and forth between the front and the back facet mirrors. A standing wave develops under the resonance condition which is expressed below as [2]:

$$L = m\frac{\lambda}{2} = m\frac{\lambda_0}{2n_{eff}} \tag{2.1}$$

where L is the cavity length, m is the number of nodes, λ_0 is the wavelength in vacuum and n_{eff} is the effective refractive index of the laser. If the optical gain compensates the loss due to optical absorption and mirror losses threshold condition is reached for lasing and threshold gain is expressed as [1]:

$$g_{th} = \alpha_i + \frac{1}{2L} ln(\frac{1}{R_f R_r}) \tag{2.2}$$

where g_{th} is the threshold gain, α_i is the internal losses and R_f and R_r are the front and rear facet reflectivities, respectively.

The emission wavelength of the lasers is determined by the band gap of the semiconductor used in the active region. Therefore, different emission wavelengths can be achieved using different material systems. The relation between the emission wavelength and the direct band gap energy is given as [18]:

$$\lambda = \frac{h.c}{E_g} \approx \frac{1.24}{E_g[eV]} \tag{2.3}$$

where h is the Planck constant, c is the speed of light in free space and E_g is the band gap energy. Material systems are also selected depending on the lattice constants of the semiconductor materials which are responsible for a defect-free interface between the semiconductors. The material's lattice constant should match to that of the substrate to prevent the formation of mechanical defects. The lattice mismatch is also dependent on the material composition. It desired to be smaller than 0.1% and can be achieved for many compounds [2]. Thus, most III-V and II-VI compound semiconductors can be used in laser diode applications.

The transverse vertical confinement is crucial for effective lasing operation. Photons and carriers are confined in an active region by band gap engineering. The undoped active material is embedded in n- and p- type high band-gap materials. Electrons and holes are confined in the active region and recombine under forward bias. In double hetero-structures (DHs), active region consists of a thin active layer sandwiched between higher bandgap materials. The schematic illustration of the energy band diagram along the vertical direction, x, for a forward biased double heterostructure is shown in figure 2.2. Typical active layer thicknesses in DH structures and structures with QWs are on the order of 0.1- 0.2 μm and about 10 nm, respectively [2]. There are many advantages of the QW lasers such as low threshold current, high characteristic temperatures, high quantum

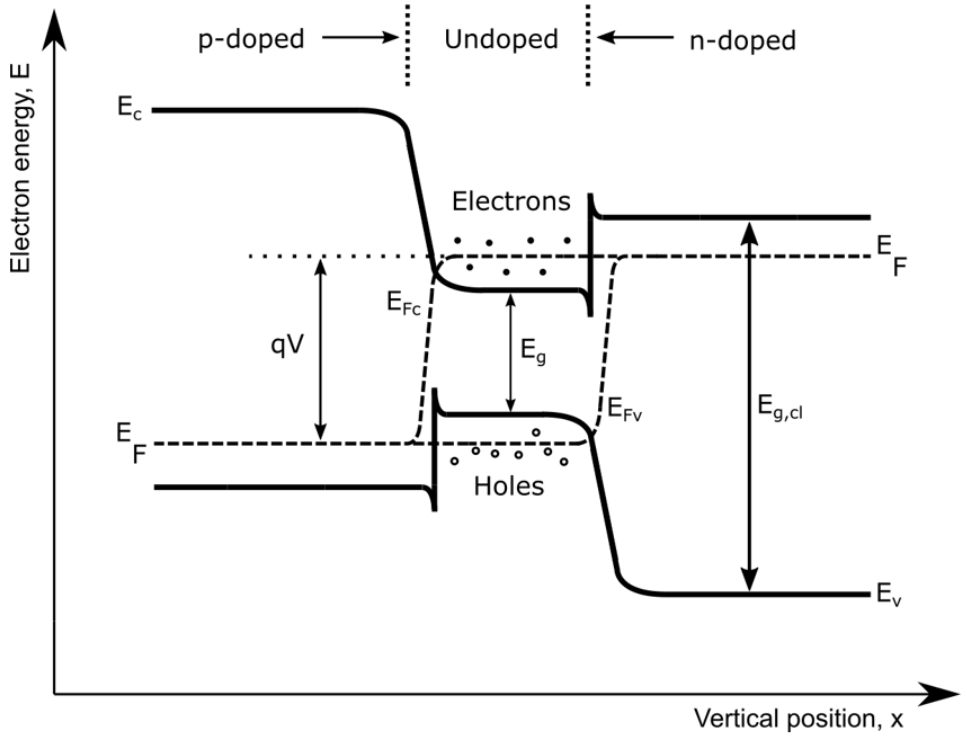

Figure 2.2: Schematic illustration of the energy band diagram versus vertical direction x for the forward biased double heterostructure.

efficiencies and wall plug efficiencies. Confinement factor is increased in separate-confinement hetero-structures (SCH). The generated light is confined in the active region benefiting from the wave guiding structure in the vertical direction. Typically, the active region has higher refractive index whereas cladding lasers has lower refractive index. Photons generated in the active region undergoes total internal reflection in the waveguide structure. Thus, optical mode confines in the vertical direction by index guiding.

Moreover, transverse lateral confinement is required to increase the performance of edge emitting diode lasers. In gain guided lasers, a current aperture is formed by, for example, ion implantation forming a stripe laser which provides current confinement (fig. 2.3a). There are many disadvantages of gain guiding lasers such as high threshold current densities and low differential quantum efficiencies due to lossy waveguides. In ridge waveguide lasers (fig. 2.3b), the

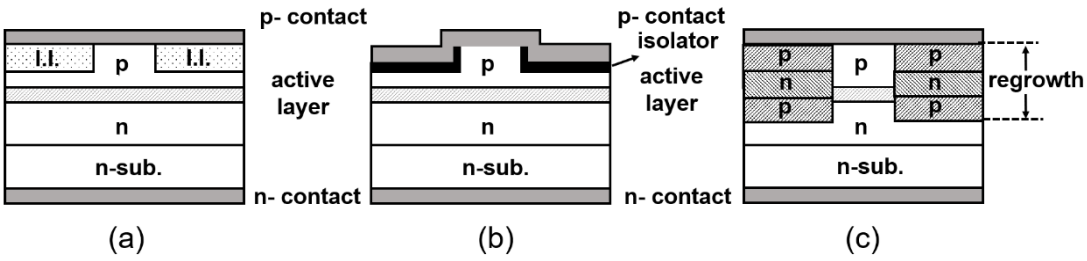

Figure 2.3: Schematic illustrations of (a) gain guided laser (b) ridge waveguide laser and (c) buried heterostructure.

passivation at the edge of the ridge helps the current confinement. Also, lateral index step created by the ridge provides the optical and carrier confinement. In buried heterostructures (fig. 2.3c), the active layer is buried on all sides with higher band and lower indices semiconductors. Therefore, carriers are confined besides the optical and current confinement.

2.2 Laser operating model

2.2.1 Carrier injection and photon generation

Solutions to the coupled electron and photon density rate equations shed light on the lasing behaviour of most semiconductor lasers. Laser characteristics closely depend on the carrier concentration in the active region and carrier density can be expressed using the generation and recombination rate balance which can be written as [4]

$$\frac{dN}{dt} = R_{gen} - R_{nr} - R_{sp} - R_{stim} \tag{2.4}$$

The first term on the right hand side shows carrier generation rate and the last three terms express the recombination rates for nonradiative, spontaneous radiative and stimulated radiative processes. The generation rate is equal to the number of injected carriers into the active region per unit time and volume.

Therefore, it can be written as [4]

$$R_{gen} = \frac{\eta_i j}{qd} \tag{2.5}$$

where η_i is the internal efficiency which indicates the conversion of current into carriers in an active region, j is the current density, q is the elementary charge and d is the active layer thickness. The R_{nr} is the non-radiative recombination rate and R_{sp} is the spontaneous emission rate and they can be expressed as [4]

$$R(N) = AN + BN^2 + CN^3 = \frac{N}{\tau} \tag{2.6}$$

where AN is the non-radiative recombination rate related to the Shockley-Read-Hall (SRH) recombination, BN^2 is the spontaneous emission rate and CN^3 is the Auger recombination rate. The carrier density decays inside the cavity as a function of carrier life time τ. Stimulated emission which provides gain increases the photon density exponentially in the active region. Therefore, photon generation rate is equal to the stimulated emission rate and it can be written as [4]

$$R_{stim} = \frac{dN_{ph}}{dt} = \frac{dN_{ph}}{dz}\frac{dz}{dt} = g(N, \lambda_0) N_{ph} \upsilon_{gr} \tag{2.7}$$

where $g(N, \lambda_0$ is the material gain, N_{ph} is the density of photons and υ_{gr} is the group velocity of photons in the active region. As a result, the change of carrier density in an active region becomes [4]

$$\frac{dN}{dt} = \frac{\eta_i j}{qd} - \frac{N}{\tau} - g(N, \lambda_0) N_{ph} \upsilon_{gr} \tag{2.8}$$

2.2.2 Optical loss, gain and threshold conditions

Gain is generated in the active region by stimulated emission. However, the material gain which is the gain of the active region is different from the modal gain which is the gain experienced by each optical mode. The modal gain depends on the overlap of the optical mode with the active region which is defined as a confinement factor Γ. The modal gain and confinement factor can be written as [2]

$$g_{modal} = \Gamma g \tag{2.9}$$

$$\Gamma = \frac{\int_{-d/2}^{+d/2} |E(x)|^2 dx}{\int_{-\infty}^{+\infty} |E(x)|^2 dx} \tag{2.10}$$

where $|E(x)|^2$ is the intensity of the optical mode propagating along the cavity and $-d/2$ and $+d/2$ are the active layer boundaries through the epitaxial direction. The propagating light intensity decreases exponentially due to the optical losses inside the cavity. Thus, it can be described as [2]

$$P(z) = P_0 \exp(-\alpha z) \tag{2.11}$$

where P_0 is the initial intensity and α is the absorption coefficient. It is described as

$$\alpha = \alpha_i - \Gamma g \tag{2.12}$$

α_i is the internal loss due to the free carrier absorption and absorption from the defects. Intensity increases in the case of optical gain which refers to $-\alpha$ when modal gain exceeds internal loss (α_i). Optical mode intensity after one round trip in the cavity is equal to

$$P_{rt} = P_0 R_f R_r \exp[2(\Gamma g - \alpha_i)L] \tag{2.13}$$

where R_f and R_r are the front and rear mirror reflectivities, respectively and L is the cavity length. At threshold condition, P_{rt}= P_0. Thus, threshold modal gain becomes the summation of internal loss and mirror losses as given in below [2]

$$1 = R_f R_r \exp[2(\Gamma g_{th} - \alpha_i)L], \tag{2.14}$$

$$\Gamma g_{th} = \alpha_i + \frac{1}{2L} ln(\frac{1}{R_f R_r}) = \alpha_i + \alpha_{mirror} \tag{2.15}$$

2.2.3 Current dependent optical output characteristics

Above the lasing threshold, lasers are in the steady state. Under this condition carrier and photon density is conserved. Thus, the rate equations can be expressed as below [4]

$$\frac{dN}{dt} = \frac{\eta_i j}{qd} - \frac{N}{\tau} - \upsilon_{gr} g(N, \lambda_0) N_{ph} = 0 \tag{2.16}$$

and

$$\frac{dNph}{dt} = \upsilon_{gr} \Gamma g(N, \lambda_0) Nph - \frac{N_{ph}}{\tau_{ph}} = 0 \tag{2.17}$$

Second equation implies that below the threshold photon density, N_{ph} is equal to zero and above the threshold we find the relation:

$$\upsilon_{gr} \Gamma g_{th}(N, \lambda_0) = \frac{1}{\tau_{ph}} \tag{2.18}$$

By putting equation 2.18 into the equation 2.16, photon density above threshold is found as

$$N_{ph} = \Gamma \frac{\eta_i \tau_{ph}}{qd} j - \Gamma \frac{\tau_{ph}}{\tau(N_{th})} N_{th} \tag{2.19}$$

The threshold current density can be calculated from the above equation. At threshold, photon density becomes zero and threshold current density becomes

$$j_{th} = \frac{qd}{\eta_i \tau(N_{th})} N_{th} \tag{2.20}$$

By combining equation 2.20 and 2.19, the current density dependent photon density is found as:

$$N_{ph} = \eta_i \frac{1}{qd\upsilon_{gr} g_{th}} (j - j_{th}) \tag{2.21}$$

The output power is the measure of photons extracted from the laser mirrors. When photons go through the mirrors, mirror loss decreases the photon density in the cavity. Therefore, output power depends on the mirror loss and the photon density in the cavity. This can be expressed as:

$$P = \alpha_{mirror} \upsilon_{gr} N_{ph} \hbar w \frac{LWd}{\Gamma} = \eta_i \frac{\alpha_{mirror}}{\Gamma g_{th}} \frac{\hbar w}{q} (I - I_{th}) \tag{2.22}$$

As we mentioned in section 2.2.1, Γg_{th} is the sum of the internal and mirror losses. Therefore, the output power is equal to:

$$P = \eta_i \frac{\alpha_{mirror}}{\alpha_i + \alpha_{mirror}} \frac{\hbar w}{q} (I - I_{th}) = \eta_{ext}^d \frac{\hbar w}{q} (I - I_{th}) \tag{2.23}$$

where η_{ext}^d is the external differential quantum efficiency which indicates the conversion of electrons to photons emitted from the laser facets. Therefore, it

is equal to the ratio of differential increase of photons per time ($dP/\hbar w$) and differential increase of injected carrier per time (dI/q). Thus, external differential quantum efficiency becomes [4],

$$\eta_{ext}^{d} = \frac{dP/\hbar w}{dI/q}\frac{q}{\hbar w}\frac{dP}{dI} \tag{2.24}$$

The right most term is the expression of the slope efficiency. It is calculated from the current dependent output power graph. Beyond the threshold, power increases linearly with injected current. The slope of this graph beyond the threshold gives the slope efficiency.

The magnitudes of internal efficiency and internal loss are the measure of the laser performance. They are determined from the length dependent inverse external differential quantum efficiency measurements using the relation below:

$$\frac{1}{\eta_{ext}^{d}} = \frac{1}{\eta_i} + \frac{\alpha_i}{\eta_i}\frac{2}{ln(\frac{1}{R_f R_r})}L \tag{2.25}$$

Another crucial parameter that is effective in determining laser performance is the power conversion efficiency (PCE). It shows the efficiency of electrical power P_{el} conversion to the optical output power P_{opt}. Therefore, it is expressed as the ratio of optical output power to electrical power injected into the laser.

$$\eta_c = \frac{P_{opt}}{P_{el}} = \frac{P_{opt}}{I * U(I)} = \frac{\eta_{ext}^{d}\frac{\hbar w}{q}(I - I_{th})}{I * (U_0 + IR_s)} \tag{2.26}$$

where $U(I)$ is the current dependent voltage and U_0 is the turn-on voltage, and R_s is the series resistance. When the laser turns-on, voltage increases linearly with current. Therefore, plotting the voltage versus current, and performing a linear fit delivers the R_s.

2.3 Thermal characteristics of the high power diode lasers

Thermal properties of semiconductorlasers are important in the achievement of high optical output power and affect the reliability of the lasers by thermal induced degradation. Temperature of a laser increases due to the carrier and internal optical losses and high series resistance. Laser operation temperature depends on the design and the fabrication of the laser structure.

2.3.1 Characteristic temperatures and thermal resistance

Characteristic temperature, T_0 of the lasers is a parameter measuring the temperature sensitivity of the lasers. The carrier escape from the active region causes reduced characteristic temperature which leads to the high threshold current. The relation between the threshold current and T_0 is given as:

$$I_{th} = I_0 \exp\left(\Delta T\right)/(T_0) \tag{2.27}$$

where I_0 is the initial threshold current, and ΔT is the temperature rise. As indicated in the above relation, threshold current exponentially increases with the temperature rise and exponentially decreases with the T_0. When the threshold increases, the output power and laser efficiency decreases. T_0 is increased by reducing carrier losses due to scattering, carrier leakage and free-carrier absorption. Proper fabrication process and design optimization such as the choice of material composition, doping level, growth conditions are required. The characteristic temperatures are higher in QW lasers due to the higher carrier confinement and lower threshold currents. It is especially higher for strained lasers due to better confining potentials and the lower band filling effect. [2, 4].

Another crucial parameter affecting the laser optical output power and efficiency is the thermal resistance which defines the temperature rise due to the

dissipated power during the laser operation and is described by:

$$R_{th} = \frac{\Delta T}{P_{waste}} \tag{2.28}$$

where ΔT is the temperature difference between the active region and heat sink and P_{waste} is the dissipated power which is the difference between the electrical and optical power. Dissipated electrical power can not converted into optical power and it becomes waste heat load. Increasing the active region temperature leads to the higher threshold currents, lower laser efficiency, and saturation or even decreasing of the output power. This power limiting phenomena is called thermal rollover. Therefore, reducing thermal resistance is crucial to increase thermal roll over power. For epi-up mounted lasers, the laser is thinned to improve thermal resistance. However, smallest thermal resistance is obtained through the epi-down mounting. The thermal resistance of epi-down mounted lasers is around 2.5 K/W. Another way to reduce thermal resistance is making the laser longer, however optical loss increases with cavity length [2].

2.3.2 Theory of the catastrophic mirror damage

One of the significant limitations of the output power and electro-optical power conversion efficiency is the catastrophic optical mirror damage (COMD) which causes the sudden failure of the lasers[19, 20, 21]. The main reasons of the COMD are the Joule heating at the facets due to the non-radiative recombination centers on the mirror surface. This is exacerbated even further due to increasing heat load linked to the temperature induced band gap shrinkage[19, 21]. The critical temperature for catastrophic failure reported in the literature is in the range of 120-160°C[21].

Surface traps are caused by the impurities attracted by the dangling bonds at the laser facet. Also, the surface oxides create defects, thus Al-based material systems whose oxidation rate is high is more prone to the non-radiative recombination and the recombination rate is proportional with the Al content. Therefore,

the COMD threshold for AlGaAs/GaAs lasers is smaller than that for the Al-free lasers. COMD threshold is increased by reducing internal optical power density, P_{int} which is expressed as [22, 18]:

$$P_{int} = P_{max,cw} \cdot \frac{1+R_f}{1-R_f} \cdot \frac{1}{(\frac{d}{\Gamma}).W} \tag{2.29}$$

where $P_{max,cw}$ is the maximum optical output power under CW operation, R_f is the front facet reflectivity, $\frac{d}{\Gamma}$ is the description of vertical spot size, d is the active region thickness, Γ is the confinement factor, and W is the ridge width. Optical power density can be decreased by expanding the mode into a larger volume. Therefore, the COMD threshold is higher in large optical cavity (LOC) designs.

2.4 Fast axis and slow axis beam divergence

Solving the homogeneous Helmholtz equation, the optical field emitted into the air can be derived. The emitted light is diffracted into air. Diffraction pattern is found using a Fresnel diffraction formula in the near field, however Fraunhofer diffraction formula is used to determine far-field profile of the emitted light. A schematic of the near and far field profiles of the ridge waveguide laser is shown in figure 2.4. Near field profile can be expressed in the form of a uniform Gaussian pattern [23]. Thus, it becomes

$$P(x,y) = P_0 exp[-(2x^2/x_0^2) - (2y^2/y_0^2)] \tag{2.30}$$

where P_0 is the intensity at the center of the beam, and x_0 and y_0 are the beam radius in the x and y direction, respectively. Spatial Fourier transform of the near field amplitude is given as below [23]:

$$E_0(K_x, K_y) = \int_{-\infty}^{+\infty} \int \sqrt{P(x,y)} \exp\left[i(K_x x + K_y y)\right] dxdy \quad (2.31)$$

$$= \sqrt{P_0(x_0 y_0 \pi)} \exp\left[-(K_x x_0/2)^2 - (K_y y_0/2)^2\right] \quad (2.32)$$

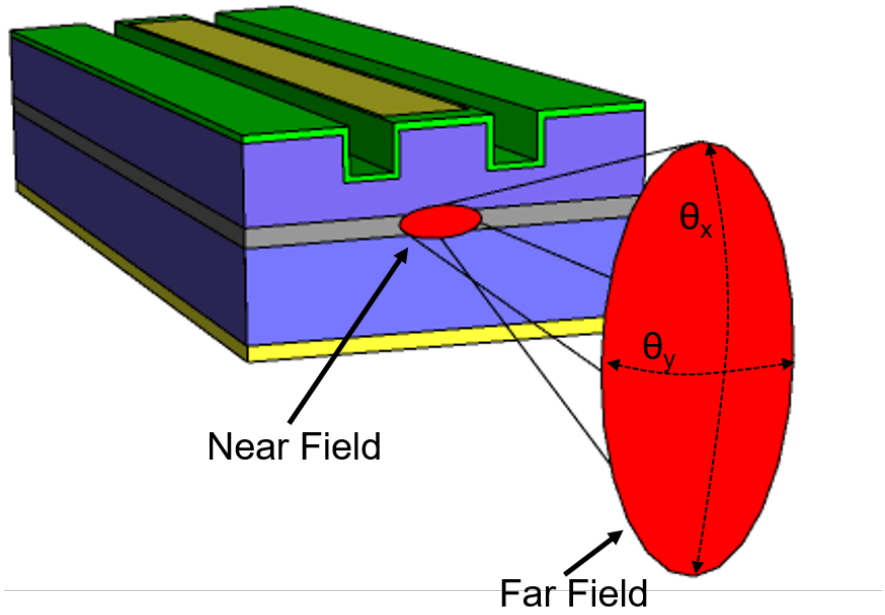

Figure 2.4: Schematic representation of the near and far field profiles of the ridge waveguide laser.

Thus, the far-field intensity is

$$P_{FF}(\theta) = |E_0(K_x K_y)|^2 \cos^2\theta/(\lambda_0 r)^2 \quad (2.33)$$

where λ_0 is the emission wavelength and $K_0 = 2\pi/\lambda_0$ is the wavenumber. $K_x = K_0 \sin\theta\cos\phi$ and $K_y = K_0 \sin\theta \sin\phi$ in spherical polar coordinates. The vertical far-field intensity is found by taking the $\phi = 0$ and it is expressed as [23, 24]

$$P_{FF}(\theta) = P_0 \cos^2\theta (\frac{\pi x_0 y_0}{\lambda_0 r})^2 exp\left\{-2[(K_0 x_0/2)\sin\theta]^2\right\} \quad (2.34)$$

Lateral far-field intensity is found by taking the $\phi = \pi/2$ and it is expressed as [23, 24]

$$P_{FF}(\theta) = P_0 \cos^2\theta (\frac{\pi x_0 y_0}{\lambda_0 r})^2 exp\left\{-2[(K_0 y_0/2)\sin\theta]^2\right\} \tag{2.35}$$

Far-field divergence angle depends on the radiating aperture. As the aperture gets larger, far field divergence becomes smaller. Divergence angle for the axis perpendicular to the semiconductor layers is called the fast axis divergence angle whereas that for the axis parallel to the semiconductor layers is called slow axis divergence angle.

Chapter 3

Experimental

3.1 Design of a high power diode laser

Design of a laser cavity is an complicated task at best. There are many parameters to take into account. Both the laser structure as well device design and fabrication is important to improve the efficiency of the diode lasers. High power lasers typically use wide wave guide device structures as well as large optical cavities. Advantages of the expanding the mode in the transverse vertical direction are strong reduction in the divergence angle and achieving low threshold current as well as lower risk of COMD failure at high power operation and suppression of beam filamentation effects. Our laser structure design is shown in figure 3.1. We designed a single quantum well InGaAs/AlGaAs laser emitting at 915 nm. The index and optical mode profile of this structure is given in figure 3.2. Optical mode is asymmetrically expanded toward the substrate side by increasing the refractive index of the n-cladding layer relative to that of the p-cladding to reduce free carrier absorption. This will also keep the mode away from the top metal contact eliminating the possibility of absorption by the top metal contact. Epitaxial growth was done at JenOptik AG (www.jenoptik.com) via metal organic chemical vapor deposition (MOCVD) [25].

	Material	Thickness (nm)	Doping (cm^{-3})	Dopant
Contact	GaAs	100	5.E+19	C
Cladding layer	$Al_{0.45}Ga_{0.65}As$	500	5.E+18	C
		300	1.E+18	C
		200	2.E+17	C
Waveguide	$Al_{0.25}Ga_{0.75}As$	200	1.E+17	C
		300	5.E+16	C
Active region	$In_{0.08}Ga_{0.92}As$	8	-	-
Waveguide	$Al_{0.25}Ga_{0.75}As$	100	-	-
		400	5.E+16	Si
Cladding layer	$Al_{0.30}Ga_{0.70}As$	500	1.E+17	Si
		2500	5.E+17	Si
Buffer layer	GaAs	500	2.E+18	Si
Substrate		n-GaAs (100)		

Figure 3.1: Laser structure.

3.1.1 Electronic design

The band structure of the active region affects the laser performance and lasing wavelength. Therefore, the electronic structure of the laser should be carefully designed. Design is based on the solutions of the self-consistent Schrdinger and Poisson equations. The solutions give the eigenenergies and eigenfunctions. The gain profile and the emission wavelength is determined from these solutions. We aim to fabricate lasers emitting at 915 nm, which can be used for pumping fiber amplifiers. One way to obtain the lasing wavelength of 900-1100 nm is the use of strained $In_xGa_{1-x}As/Al_yGa_{1-y}As$ layer systems [2]. Lasing wavelength depends on the thickness and mole fraction of In in the InGaAs alloy [26]. The higher efficiency and reliability of the strained quantum QW lasers than that of the unstrained conventional lasers are proven [2]. Advantages of these lasers are low threshold current density due to the reduced density of states and thus of the reduced hole effective mass, higher differential gain, lower laser linewidth, and higher characteristic temperature [2]. Under the biaxial compression, the non-parabolicity of the heavy-hole (hh) and light-hole (lh) valence bands decreases and the degeneracy of the hh and lh at the maximum of the band splits off leading to decrease in valence band effective masses and increase in the energies of hh and lh valence bands relative to conduction band. In this case, the density of states

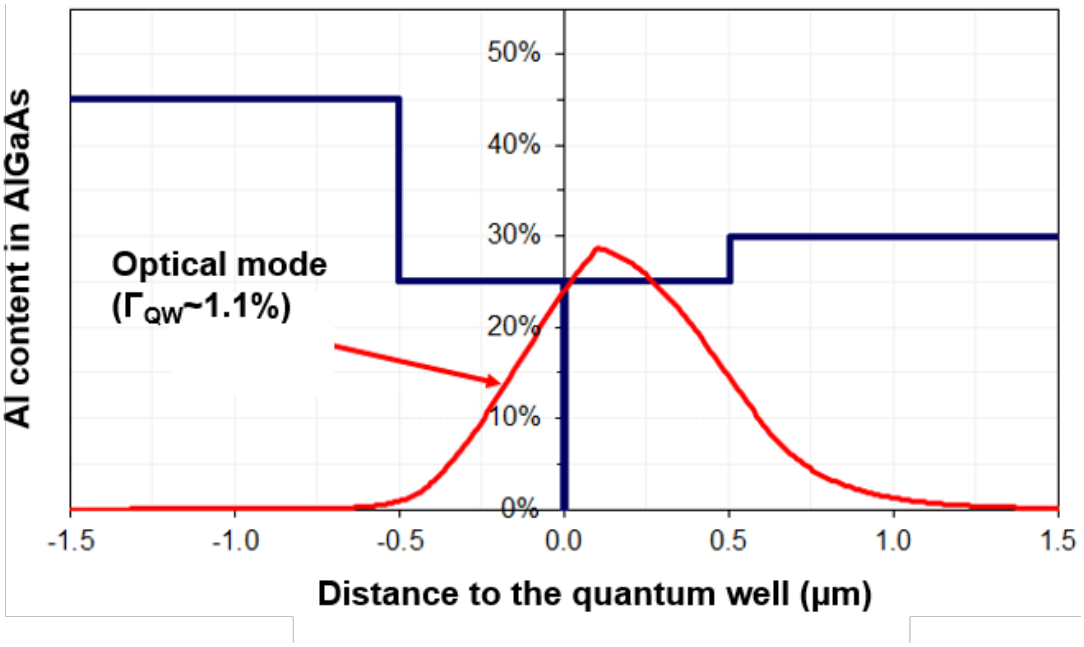

Figure 3.2: Calculated mode profile of the laser.

in the valence band becomes comparable the density of states in the conduction band [2, 27, 28, 29].

3.1.2 Optical design

The high power laser structure consists of quantum well embedded in waveguide layers. Waveguide layers have larger bandgap, low doping for reduced free carrier absorption and lower refractive index than that of the quantum well. The light generated at the active region makes total internal reflection and is confined in the active region. Thus, this three-layer structure behaves like optical waveguide. This active region is further embedded in a sandwich of doped cladding layers. The index of refraction of the cladding layers are smaller than that of the waveguide layers. The thickness, doping level and composition of the layer are optimized to decrease the threshold current, the risk of COMD, series resistance and free-carrier absorption. However, some requirements conflict each other such as high doping, necessary to decrease series resistance can increase the free-carrier

absorption. The composition of the cladding is adjusted to provide the index difference between the active region and the cladding for mode confinement. For the $In_xGa_{1-x}As/Al_yGa_{1-y}As$ laser system, Al content of $Al_yGa_{1-y}As$ is increased to increase the index step between the active region and the cladding. The thickness of the $Al_yGa_{1-y}As$ cladding region is increased to decrease the effective index of the $Al_yGa_{1-y}As$ cladding layer. However, thicker cladding layer leads to the high series and thermal resistance. Series resistance can be decreased by increasing the doping level, however this increases the free carrier absorption. In our experiments, we used 1.0 μm $Al_{0.45}Ga_{0.55}As$ for p-cladding and 3 μm $Al_{0.30}Ga_{0.70}As$ for n-cladding. The asymetric cladding design is used to shift mode to the n-side to prevent free carrier absorption due to the highly doped p-cladding. A large optical cavity design in which the waveguide layer is relatively thick is used in our experiments. The 500 nm thick $Al_{0.25}Ga_{0.75}As$ is used as a waveguide layer. We calculated the field distribution, and the field does not penetrate into the p-cladding layer due to the thicker waveguide layer leading to low free carrier absorption. The laser structure and the mode profile of this laser are given in figure 3.1 and figure 3.2. Thus, increasing the doping level of cladding layers, and reducing the thicknesses of these layers allow us to decrease series and thermal resistance of the diode laser. Optical confinement is smaller in LOC design; however laser performance is increased due to the low loss.

3.1.3 Crystal growth

The most popular crystal growth techniques for high power diode lasers are the molecular beam epitaxy (MBE) and metal-organic chemical vapor deposition (MOCVD). The schematic illustration of the MBE and MOCVD crystal growth techniques are given in figure 3.3. MBE system works under ultra-high vacuum (UHV$<10^{-10}$ Torr) whereas MOCVD carries out deposition at low pressure which is around 0.1 atm [2]. MBE provides the precisely controlled layer thickness and composition. In the MBE system, effusion cells are heated to generate thermal beams of atoms, and these beams are directed on to the heated substrate to form the epitaxial layer. The substrate temperature is adjusted depending on

the volatility of the atoms. The elements of the group V is more volatile than the group III elements. Therefore, temperature becomes lower to increase sticking coefficient of group III elements. By adjusting temperature, sticking coefficient becomes close to unity. Thus, the growth rate is determined by the flux of these elements and measured using reflection high energy electron diffraction (RHEED). Substrate temperatures for AlGaAs have to be around 700-720 °C to prevent deep-level traps and non-radiative recombination centers whereas, for InGaAs QW, temperatures have to be approximately 510 °C [2]. In contrast to MBE system, MOCVD system is based on the chemical reactions of gases obtained from the metal-organic precursors such as group-III alkyls and group-V hydrides at the substrate surface, therefore, the substrate temperature is higher than the MBE system, and it is in the range of 500-1500 °C. The thickness and composition analysis can be done by in-situ optical measurement techniques such as reflectometry and reflectance anisotropy spectroscopy (RAS) due to low pressures in the chamber. MOCVD is preferred due to the higher throughput and cost-effectiveness than MBE. MOCVD is the cheaper system because it does not require UHV.

The high power laser crystals used in our experiment were grown by MOCVD. We do not have a MOCVD system in our laboratory; therefore they were grown in a commercial facility of JenOptik AG, an integrated photonics company in Germany (www.jenoptik.com) [25].

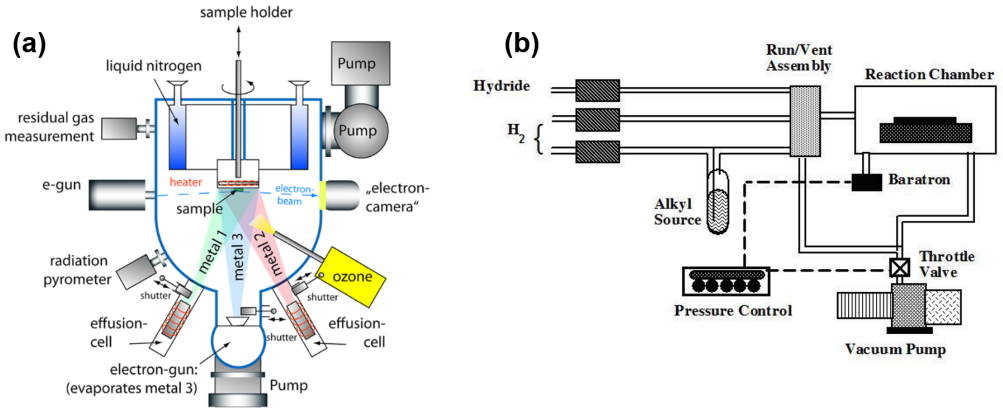

Figure 3.3: Schematic illustrations of the (a) MBE and (b) MOCVD systems (Figures reprinted from [30, 31].)

3.2 Micro-fabrication of edge emitting broad area diode lasers

We started the process of the edge emitting broad area diode lasers by designing lithography masks. We designed the photomasks using L-Edit software program. These masks were fabricated at METU-MEMS Center and UNAM Research Center. Microfabrication starts with the top most cap layer removal. Lithography mask with 50 μm wider stripes from the laser cavity width was applied on top of the epitaxial crystal (p-side) and followed by oxygen plasma in reactive ion etching system to remove photo-resist residues in open areas. All photolithography process was followed by oxygen plasma to keep open areas clean. Cap layer was etched using H_2O:H_2O_2:H_3PO_4 (45:4:1) solution as wet etchant for 20 sec. Then, 100 μm wide ridges were defined by photolithography and the exposed areas were etched down to the p-cladding layer by the same etchant for 2.5 min. A 200 nm thick Si_3N_4 passivation layer was deposited by plasma enhanced chemical vapor deposition (PECVD) system over all of the sample. Metal contact regions were defined by photolithography and Si_3N_4 was removed from those regions using buffered oxide etchant (BOE) for 40 sec. After the top metalization photolithography, Ti/Pt/Au (20/25/200 nm) were consecutively deposited and followed by lift-off to remove the unwanted metal. Final Au layer thickness was increased up to 3-6 μm by electroplating for easier wire bonding and to help cool the laser during the epi-up testing. Before electroplating process, we defined the metallization regions by photolithography. We tested lasers in the form of a bar with several emitters on it. For this, we isolated emitters through the crystal etch down to the n- cladding. The isolation etch regions were defined by photolitography before etch. We cleave samples under the microscope to isolate bars. To do this, photomasks were designed with cleave markers. Finally, samples were thinned by H_2O:H_2O_2:H_2SO_4 (1:8:1) wet etchant to reduce series resistance. AuGe/Ni/Au (40/40/200 nm) was deposited on the back side (n-side) of the crystal for n-contact. Finally, with microfabrication finished, samples were annealed at 420°C for 2 min. in a rapid thermal processor to form an ohmic contact. The short line perpendicular to the emitter axis is etched down to 30 μm to form a trench

for ease of cleave. We cleaved laser facets using these trenches of tweezers and a sharp diamond cleaver. Our design allows the formation of three different cavity lengths of 3, 4 and 5 mm. The schematics of the this laser process steps are shown in figure 3.4.

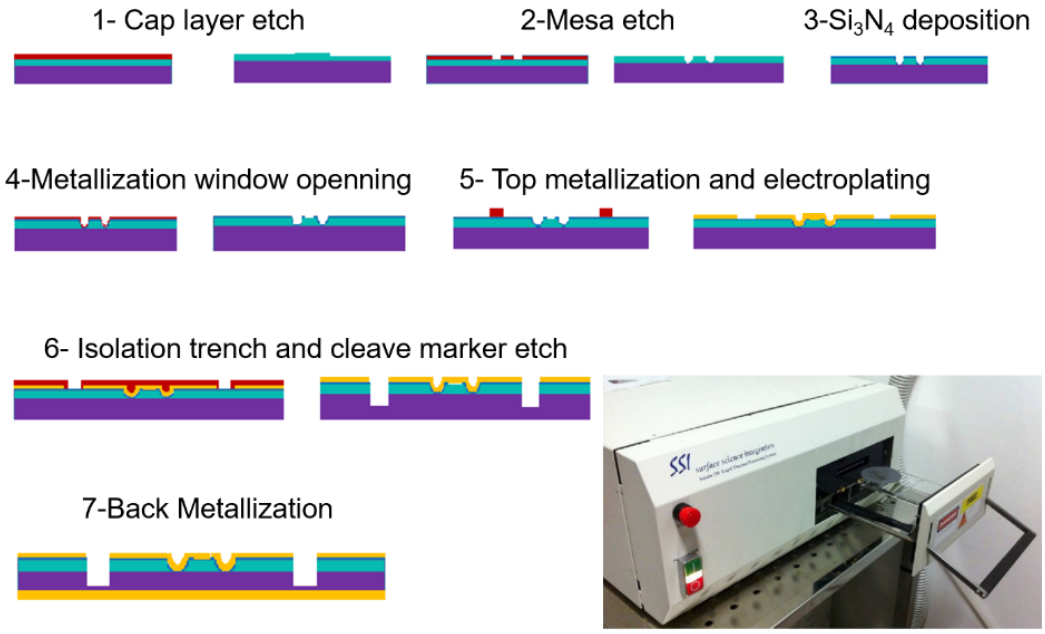

Figure 3.4: Laser diode chip fabrication steps.

In figure 3.5(a, b, c and d) the optical microscopy images from the top surface of the 3 mm long fabricated lasers with three different widths of 50, 100 and 200 μm after mesa etch, Si_3N_4 removal from the contact region, lift-off and electroplating, respectively are given.

3.3 Mounting of high power lasers for testing

We optimized the epi-up mounting techniques of the high-power diode lasers without window coatings for testing. Our aim is to study novel ideas that will help increase pulsed and CW output power. The one critical problem limiting output power of the lasers is soldering and mounting lasers on a copper plate because one has to align the laser chip on In solder while protecting laser facet

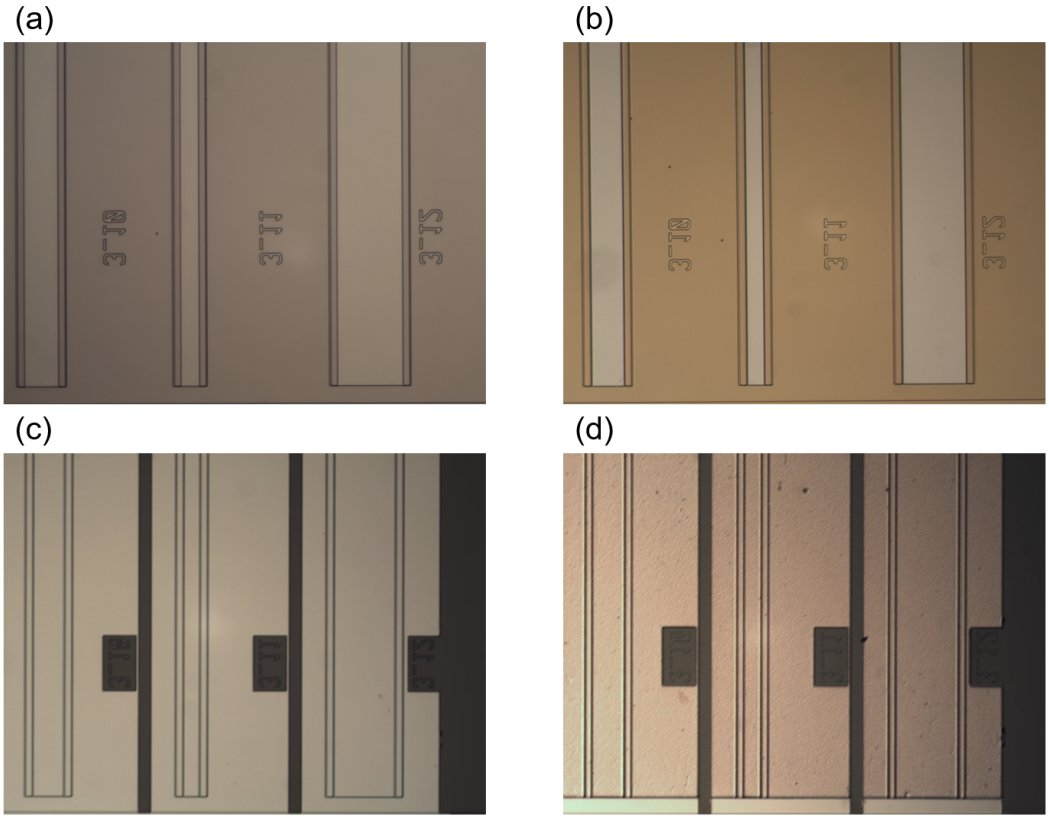

Figure 3.5: The optical microscopy images from the top surface of the 3.00 mm long fabricated lasers with three different widths of 50, 100 and 200 μm after (a) mesa etch, (b) Si_3N_4 removal from the contact region, (c) lift-off and (d) electroplating.

during the soldering. Therefore, we used the pick and place instrument shown in figure 3.6 for accurate alignment of the laser bar with the In covered copper plate. We added a heater on this instrument to heat the solder. We made a pick and place instrument with a computer controlled heater. Thus, we can move laser chip by μm step, and we can control copper plate temperature precisely. At first, we used the In tape for soldering; however, there was adhesion problem of In tape due to oxidation. Instead of In tape, we switched to an In paste, and we obtained a smooth surface. The flux inside the In paste solved the adhesion problem. Before soldering, In paste is spread on a copper plate with a dimension 1 mm smaller from every side of the laser bar using a stencil. After that, we screw the copper plate to the heater. Then we hold the laser chip with a vacuum

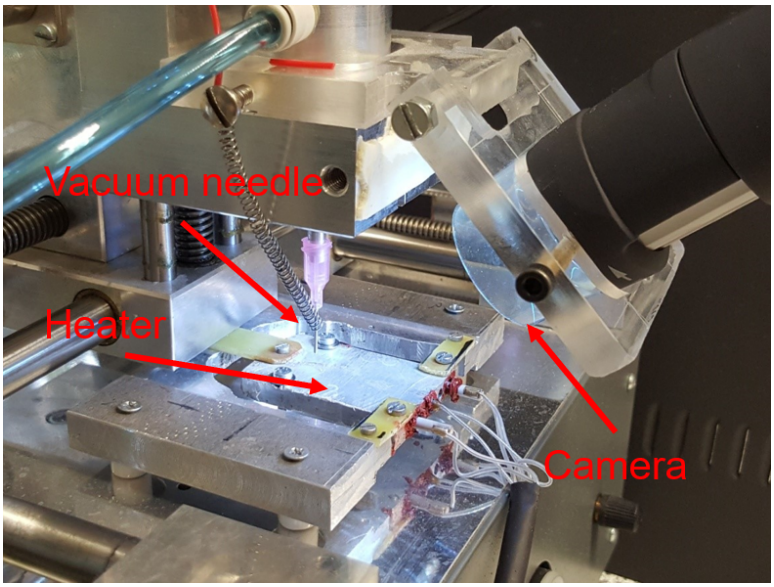

Figure 3.6: Pick and place instrument.

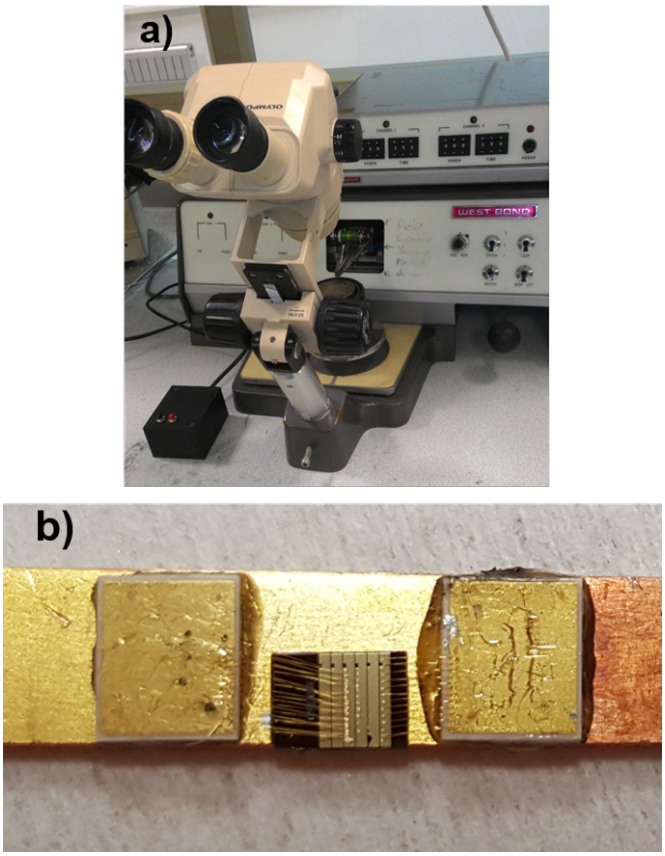

Figure 3.7: a) Wedge bonder and b) mounted and wire bonded laser chip.

needle and align it on In paste with the pick and place instrument under optical microscope. Finally, we place the laser chip on In solder film and heat the copper plate up to the 190°C; then we wait to cool In solder. We stick bonding pads on a copper plate by epoxy, and we have wire bonded top metal to the bonding pad by wedge bonder. The wire bonder and wire bonded lasers are shown in figure 3.7(a and b).

3.4 Characterization techniques

3.4.1 L-I-V characteristics and optical spectrum analysis

Electro-optical performance of the high-power laser diodes is extracted from the current-voltage-power measurements. We can find the threshold current (I_{th}), slope efficiency (S), maximum power conversion efficiency, PCE (η_c) and series resistance (R_s) from the current-voltage-power characteristics. We characterize the lasers in two regimes of pulsed and continuous wave (CW) at room temperature.

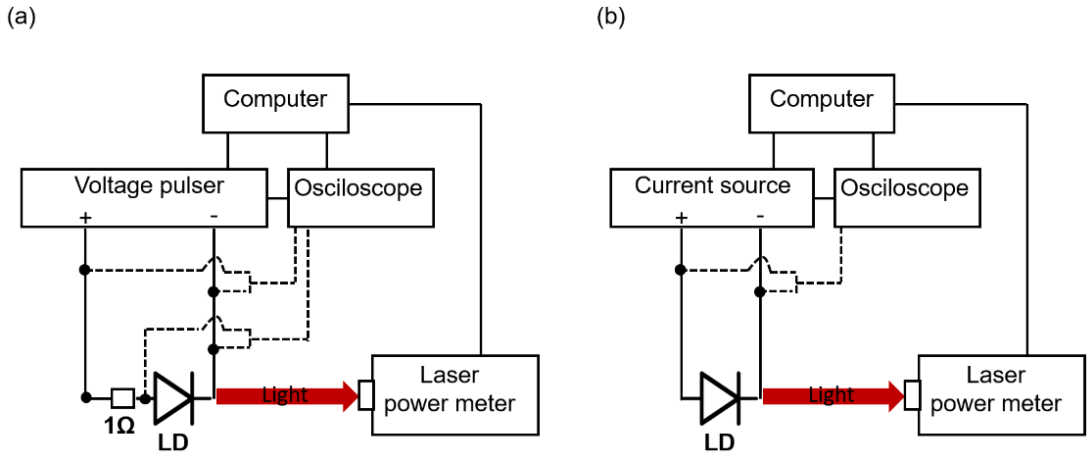

Figure 3.8: Schematics of the a) pulsed and b) CW measurement set-ups.

For pulsed measurements, we used an AVTECH voltage source. We connected a 1 resistor in series with the laser diode to measure the current. The set-up

for pulsed measurements is shown in figure 3.8a. For power measurements, we used a thermopile detector up to 2W (front facet power) with associated error of less than ±5% or an InGaAs photodedector with an integrating sphere for powers(front facet power) higher than 2W with a measurement error in the range of ±13%. The slope efficiency and threshold measurements were made in CW operation at low pump current (1A) where the power-current characteristic is linear and the measurement error is low. For CW characterization, we used ILX lightwave LDX-3600 current source. The set-up for CW measurements is shown in figure 3.8b.

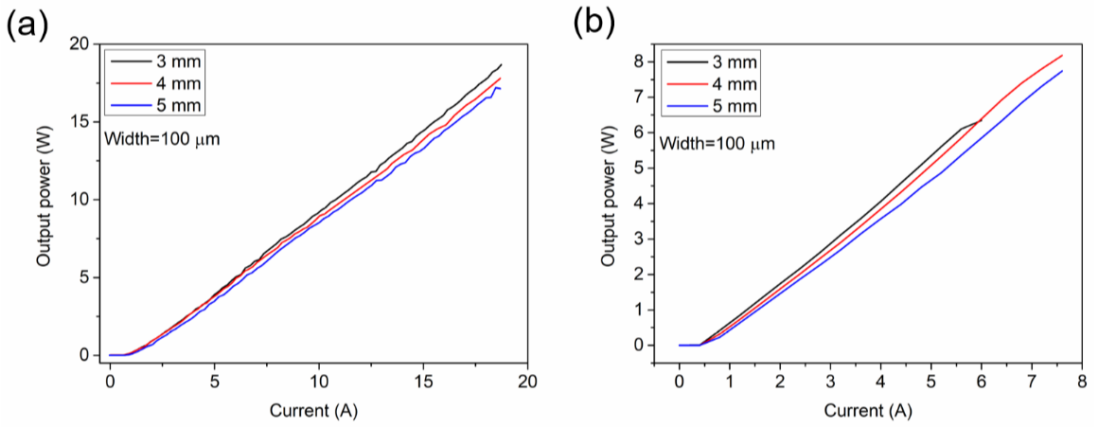

Figure 3.9: L-I measurements of 3.00, 4.00 and 5.00 mm long lasers under (a) pulsed and (b) CW operations.

We characterized 100 μm width high power broad area lasers with 3.00, 4.00 and 5.00 mm cavity lengths. In figure 3.9, the L-I characteristics of these lasers under pulsed and CW operation are given. Pulse duration was 500 ns and repetition rate was 2 kHz corresponding to 0.04% duty cycle. We tested lasers under short pulse regime because active region temperature increases with duty cycle and overheating leads to laser damage. In short pulse regime, we preserve the optical characteristics of the lasers by decreasing active region temperature. Thus, the maximum peak power is strongly increased [18]. We measured the front facet power and we found the optical output power of the uncoated lasers by multiplying front facet power by two because the back and front facet reflectivities are equal. We achieved pulsed and CW output power greater than 18W and 8W, respectively. Laser output power becomes higher by increasing PCE [2]. The

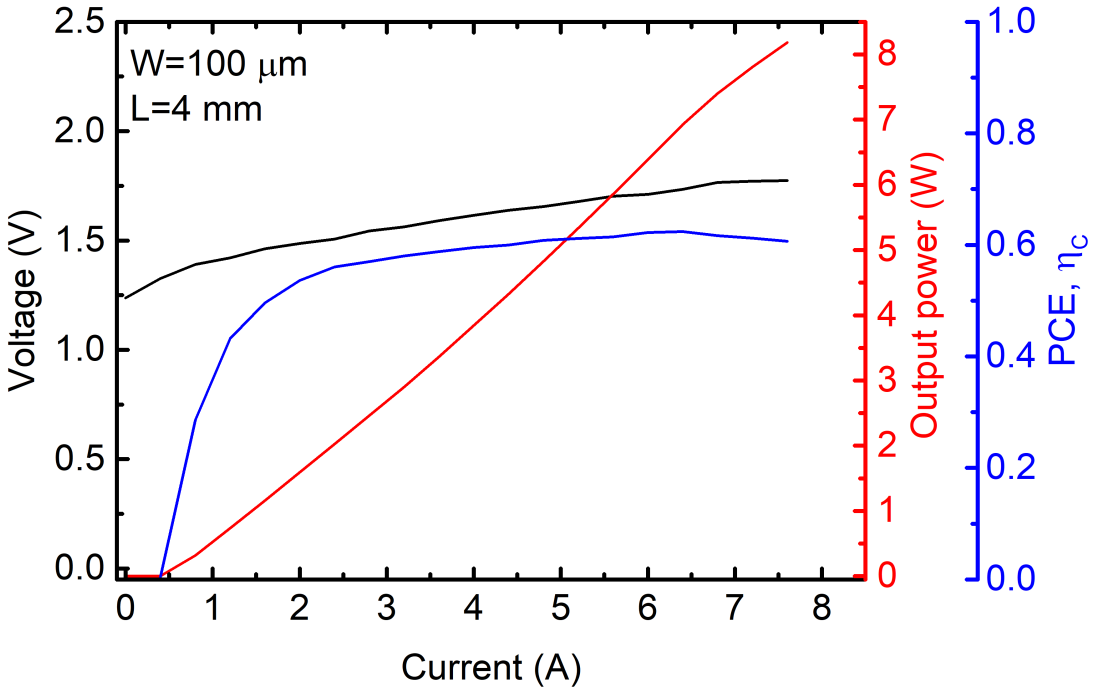

Figure 3.10: The L-V and PCE as a function of operating current for the 4.00 mm long laser under CW operation.

maximum output power and PCE obtained from epi-down mounted high-power diode lasers emitting at 9xx nm are ∼33%W and ∼65%, respectively [32, 17]. In figure 3.10, we showed the L-V and PCE as a function of operating current for 4.00 mm long laser under CW operation. Maximum PCE obtained from our lasers is ∼60%. Smaller value of output power and PCE is due to the epi-up testing. In the epi-up configuration, thermal resistance is much higher than epi-down, and it prevents the perfect cooling of the lasers [33].

In order to measure optical spectrum, the laser light is collected by a multi-mode optical fiber (0.22 NA) which is connected to the optical spectrum analyzer (Ocean Optics HR200+, spectral wavelength 190-1100 nm, resolution 0.04 nm). The emission wavelength of our lasers is around 920 nm. In figure 3.11, we show the optical spectra of the (4.00 mm)X (100 μm) laser under various CW operation currents of 1.5A, 2A, and 3A and as an inset, we indicated the spectral line width and emission wavelength as a function of operating currents. The emission

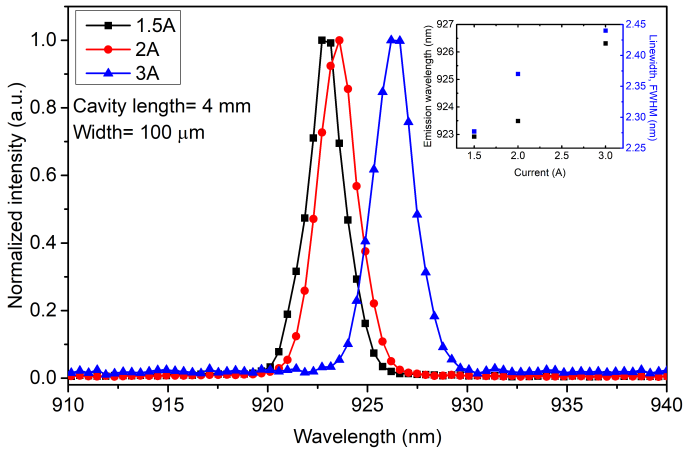

Figure 3.11: The optical spectra of the 4.00 mm long broad area laser for different CW operation currents. Inset represents the spectral line width and wavelength of this laser as a function of operation current.

wavelength makes red-shift with increasing operation current because active region temperature increases due to the Joule heating. The spectral line width of the high power broad area lasers is between the 4-5 nm at the 95% power content, and it increases with temperature [34]. The spectral linewidth of this laser under CW 1.5A, 2A, and 3A operation current is 4.00 nm, 4.17 nm, and 4.35 nm at 95% power content, respectively. Also, we showed the FWHM of the spectral line width as 2.17 nm, 2.35 nm and 2.54 nm for various current of 1.5A, 2A and 3A.

3.4.2 Internal loss and internal efficiency analysis

Internal loss (α_i), internal efficiency (η_i), and transparency current density (J_{Tr}) are obtained from the length dependence measurements. The cavity length dependence differential external efficiency is expressed as below

$$\frac{1}{\eta_{ext}^{d}} = \frac{1}{\eta_{i}^{st}} + \frac{\alpha_i}{\eta_{i}^{st} ln\frac{1}{R}} L \tag{3.1}$$

and the differential external efficiency is found from the equation below

$$\eta_{ext}^{d} = \frac{dN_{ph}}{dN} = \frac{dP/dI}{\hbar w/q} \tag{3.2}$$

where N_{ph} is the number of the emitted photon through the laser facet per unit time and N is the number of injected charged carriers per unit time.

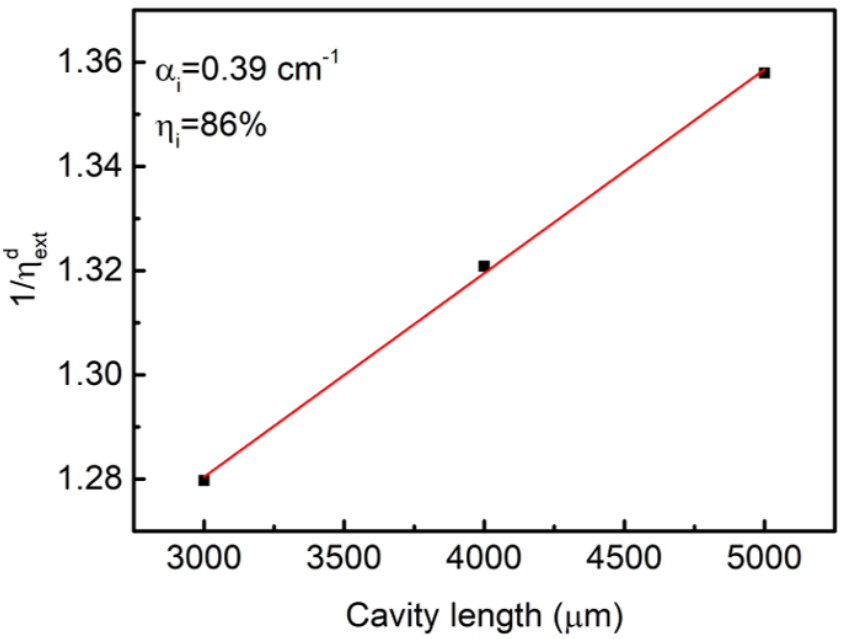

Figure 3.12: Inverse external differential efficiency versus cavity length.

Plotting the inverse differential external efficiency as a function of cavity length and performing the linear fit, we can find the internal loss from the slope and internal efficiency from the intercept. In figure 3.12, the inverse differential efficiency versus cavity length graph is given for high power laser diodes with 100 μm width. These lasers were fabricated using the conventional laser process described in the fabrication section. We obtained 0.39 cm^1 internal loss and 86% internal quantum efficiency from the CW measurements. These results are consistent with our theoretical expectations.

Transparency current density can be calculated using the relation below[35]

$$J_{tr}^{d} = J_{th}^{0} - \frac{\alpha_i de}{g'\tau\Gamma} = J_{th}^{0} - \alpha_i(\tan\Theta/2ln(\frac{1}{R_f R_r})) \tag{3.3}$$

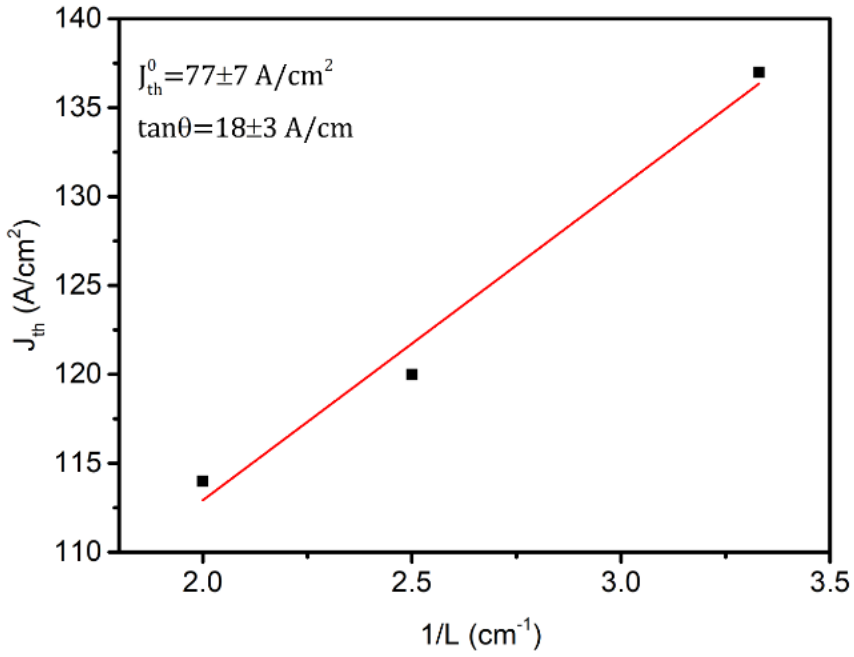

Figure 3.13: The threshold current density as a function of inverse cavity length (Copyright 2018 IEEE [36]).

where J_{th}^{0} is the threshold current density at the infinite cavity length, α_i is the internal loss, $g^{'}$ is the differential gain, τ is the carrier lifetime, d is the active layer thickness, e is the electron charge, and Γ is the optical confinement factor. Plotting the threshold current density, J_{th}, versus inverse cavity length, 1/L, and performing the linear fit give J_{th}^{0} from the intercept and $\tan\theta$ from the slope. We know the rear and front reflectivities of R_r and R_f, therefore we can calculate the transparency current density using the α_i obtained from the cavity length dependent inverse differential external efficiency calculated above. In figure 3.13, the threshold current density as a function of inverse cavity length is given for high power diode laser with 100 μm width. The J_{th}^{0} and $\tan\theta$ are found as 77±7 A/cm^2 and 18±3 A/cm. α_i is equal to 0.39 cm^1 and uncoated facet reflectivity of R_r and R_f are the same and equal to 0.32. We calculated transparency current density of our lasers as 76±7 A/cm^2.

3.4.3 Far-field measurements

We measured the lateral and vertical far-field profiles of the 100 μm width and 4.00 mm long broad area lasers fabricated in our laboratory. We calculated the lateral and vertical FWHM divergence angle from the angled dependent intensity profiles. There are many ways to measure far-field profiles of the high-power diode lasers. One way is scanning the divergent beam with a photodiode with a slit on a motorized rotating arm (goniometer). Similarly, the divergent beam can be scanned by rotating laser diodes instead of the photodiode. The uncertainty of the divergence angle depends on the slit dimension and the distance between the laser diodes and photodiode. Another way is to use a three lens systems. Lens system also allows us to measure the near-field beam profile. The first lens in front of the laser diode is an aspheric plano-convex lens to collimate laser beam and a second plano-convex lens is a focusing lens. For near-field measurements, the photodiode with a slit is put at the focal length of the focusing lens. This lens system magnifies the image at the amount of the ratio of the focal lengths of the focusing lens and collimating lens. For far-field measurements, the third lens with a smaller focal length than that of the focusing lens is put at the place where it is one focal length of the third plano-convex lens apart from the photodiode. We can find the angle from the ratio of the beam width and focal length of the third lens. However, this is the magnified image of the far-field therefore, we have to divide by the magnification where the unit of the angle is radian.

The schematic illustration of our lateral and vertical far-field beam profile characterization set-up is given in figure 3.14. The laser light directed into the photodiode using galvo mirrors. By changing the rotation angle of the galvo mirrors, we measured the intensity using a photodiode. We put 250 μm width slit in front of the photodiode to decrease the uncertainty of the far-field divergence angle. The correction factor is required for rotation angle because of their shift between the rotation axes of the galvo mirror and the laser facet. The angle correction is given in below

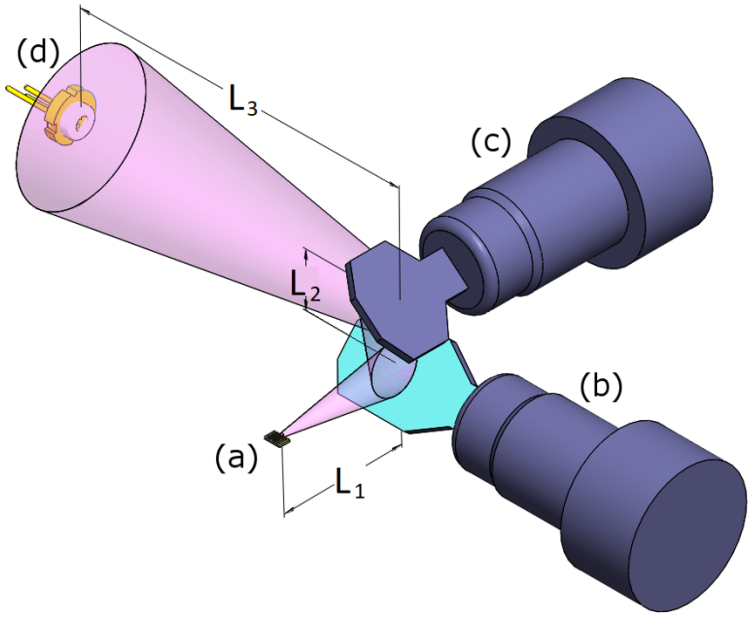

Figure 3.14: Schematic illustration of the lateral and vertical far-field characterization set-up. a) Laser diode b) first galvo mirror c) second galvo mirror d) photo diode.

for fast-axis,

$$\frac{\sin(\theta_r)}{L_3} = \frac{\sin(\theta_s - \theta_r)}{L_1} \tag{3.4}$$

for slow-axis,

$$\frac{\sin(\theta_r)}{L_3} = \frac{\sin(\theta_s - \theta_r)}{L_1 + L_2} \tag{3.5}$$

where θ_s and θ_r are the set angle, and real angle, respectively; L_1 and L_2 are the distance between the laser and first galvo mirror and galvo mirror and photodiode. We measured the beam profile of the 100 μm width and 4.00 mm long broad area laser diode under 3A CW operation current. The beam profile result is shown in figure 3.15. Through the lines, we obtained the vertical and lateral beam profile shown in figure 3.16(a and b). In figure 3.16a, the experimental vertical far-field profile and the Gaussian fit of this data is given. Experimental

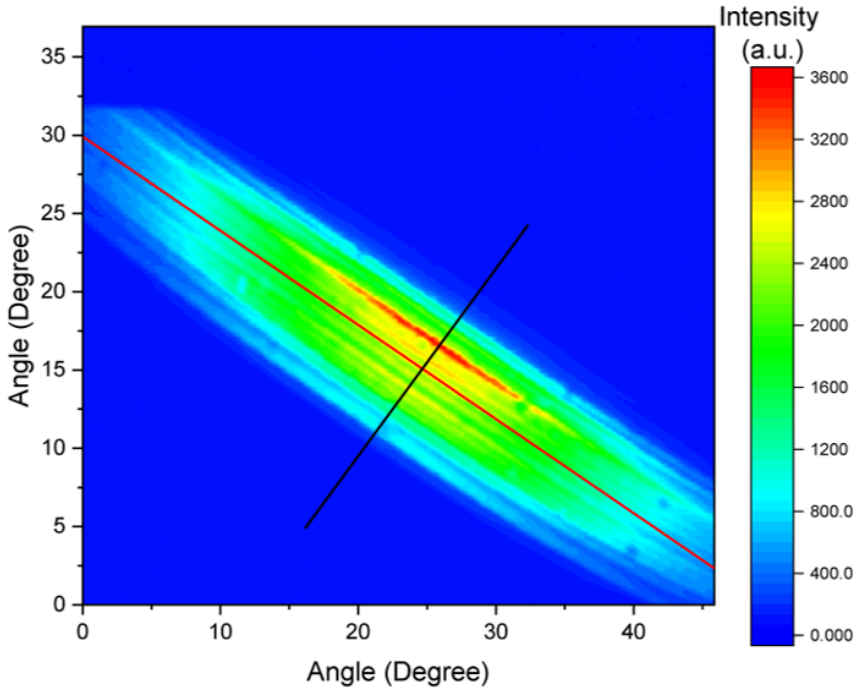

Figure 3.15: Beam profile of 100 μm width and 4.00 mm long laser under 3A CW operation current.

data does not show the tail of Gaussian function because the galvo mirror is small and it does not cover all beam. However, the Gaussian function is well fitted to the experimental data. Therefore, small galvo mirror does not prevent to measure the FWHM and 95% power content vertical beam divergence angle of 28° and 47°, respectively. The vertical divergence angle depends on the laser structure; therefore, it does not change with the operating current or output power. In the vertical direction, it is single mode; therefore we see the Gaussian profile. The lateral beam divergence angle containing the 95% power content of this laser at 3A operation current is 9.2° (fig. 3.16b). In the lateral direction, the multimode peaks are easily seen. As the current increases, the lateral beam divergence angle increases due to the higher order mode contributions.

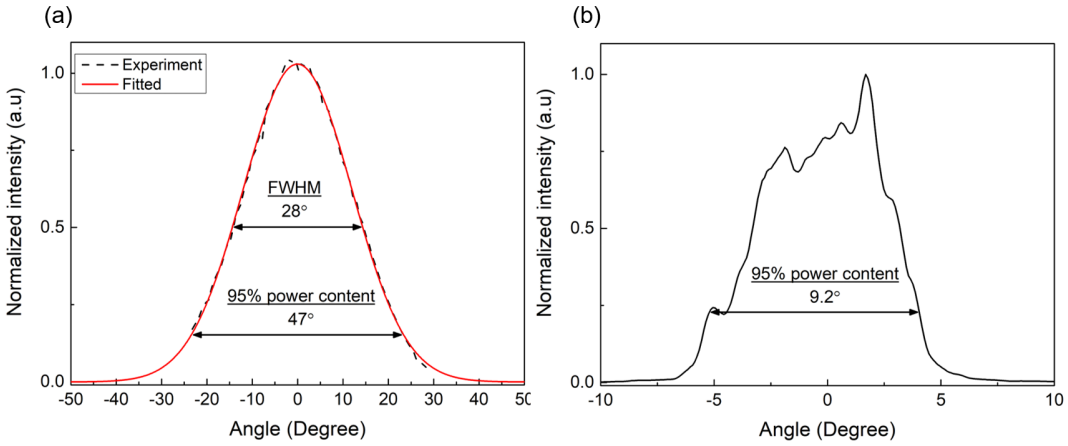

Figure 3.16: (a) The vertical and (b) lateral beam profile of 100 μm width 4.00 mm long laser under 3A CW operation current.

3.4.4 Thermo-reflectance method for facet temperature measurements

Facet temperatures of various types of lasers have previously been measured with a variety of methods. Among the most common non-contact temperature measurement methods are micro-Raman spectroscopy, photoluminescence (PL) and thermo-reflectance spectroscopy [14, 15, 16]. While micro-Raman measures lattice dilation with temperature, photoluminescence relies on the shrinkage of the band gap of the active region with temperature. Thermo-reflectance approach, on the other hand, has many varieties all relying on the changes of surface refractive indices. In this study, we used thermo-reflectance spectroscopy due to its high temperature resolution, reaching below 1K [37, 38, 39, 15, 40, 16, 41]. Typically, the temperature distribution on the facet under operating current is determined by either a point by point imaging of the surface reflectivity or by a full-scale image of the object plane, recorded for further analysis. The reflection change is proportional to the temperature change. The relation between the temperature and reflectivity is given as [38, 41, 42]:

$$\Delta T = C * \frac{\Delta R}{R} \tag{3.6}$$

and

$$C = [\frac{n^2 - 1}{4}] * (\frac{\delta n}{\delta T})^{-1} \tag{3.7}$$

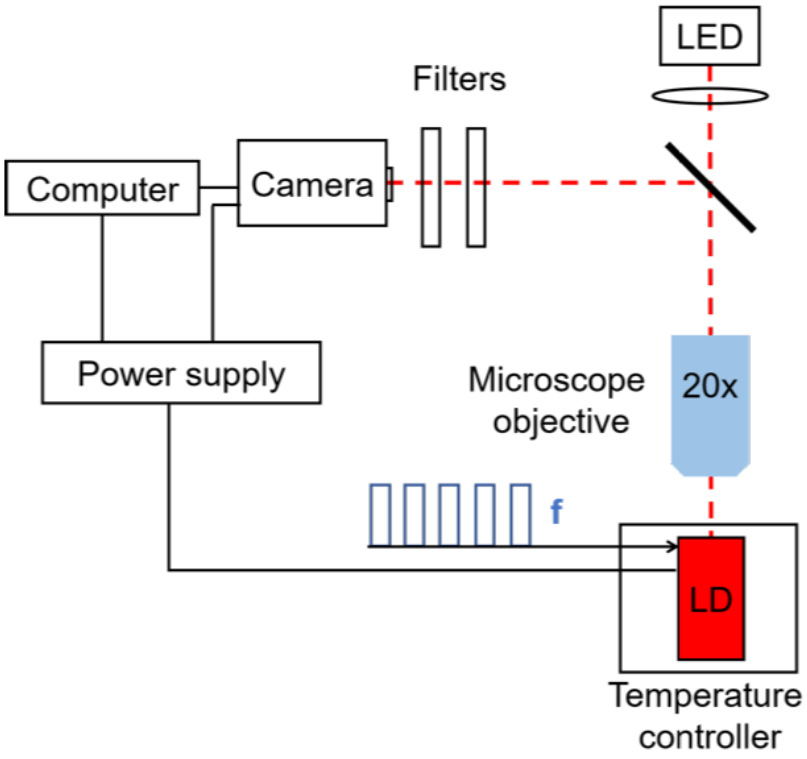

Figure 3.17: Schematic of the thermoreflectance measurement set-up (redrawn from [43]).

The thermoreflectance set-up is shown in figure 3.17. We used a LED emitting at 450 nm to illuminate the laser facet. LED is focused on laser facet by X20 microscope objective and reflected light was detected by CMOS camera. We used a beam splitter and bandpass filters to prevent laser light detection by a camera. We used the four-bucket technique to measure $\frac{\Delta R}{R}$.

To determine the temperature change (ΔT), first, we have to determine the proportionality constant, C. It is found by measuring $\frac{\Delta R}{R}$ under various temperatures. Laser temperature is controlled by a temperature controller. We plotted $\frac{\Delta R}{R}$ as a function of the temperature rise of the temperature controller as shown

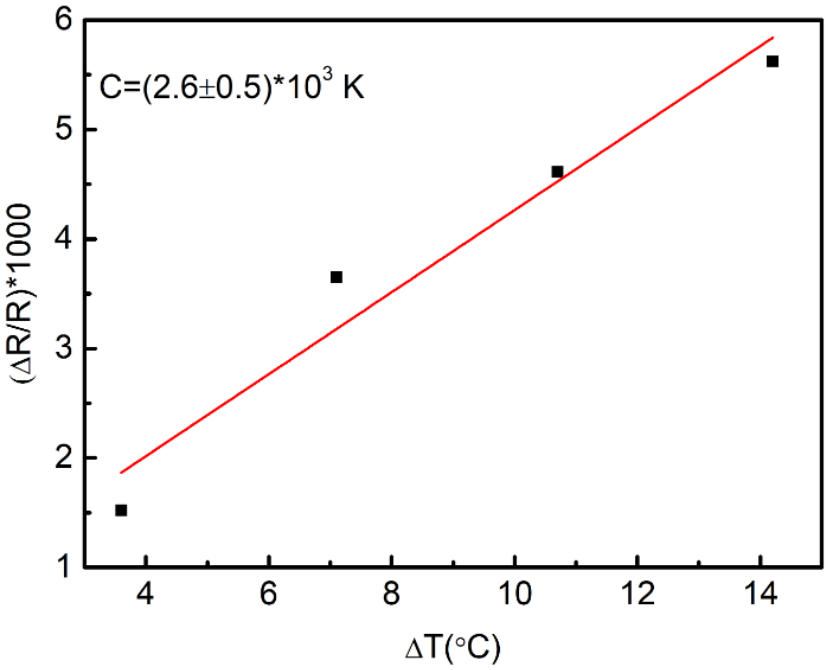

Figure 3.18: The proportionality constant of thermoreflectance.

in figure 3.18. Then, we performed line fitting to this graph and calculated, C, constant of $(2.6\pm0.5)^{*}10^{3}$ K from the slope of the line graph.

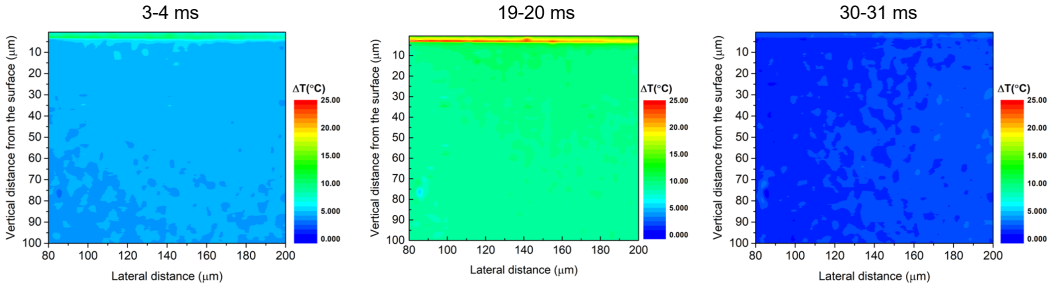

Figure 3.19: The temperature map for different time interval of the laser pulse.

We performed thermo-reflectance measurements during pulsed operation of the emitters. The pulse duration was 20 ms, and the duty cycle was set at 20 percent. We measured the temperature rise and fall at different time intervals to ensure that laser facet temperature is stabilized. When the laser is on, laser continues to heat from beginning of the pulse to the end of the pulse and cools after 30 ms which is 10 ms after the laser is turned off, as shown in figure 3.19.

Therefore, we have taken the high temperature image at 19 ms after laser was turned on and cold image at 90 ms after laser was turned off.

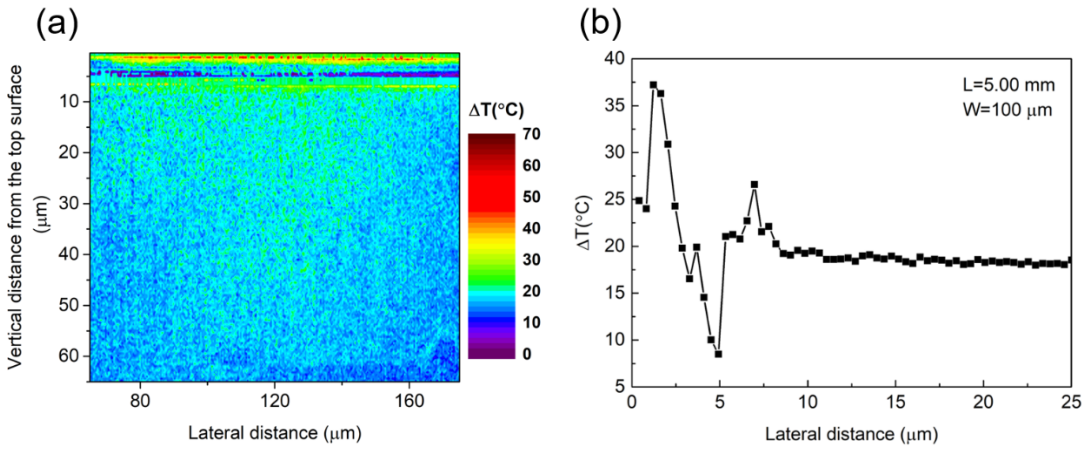

Figure 3.20: The temperature map of 5.00 mm long conventional laser at 4.00 A and (b) The temperature line scan for 5.00 mm long laser taken at the active region through the direction perpendicular to surface.

We measured the facet temperature of the 5.00 mm long high-power laser diode. The temperature map and temperature profile of this laser at 4A operation current are given in figure 3.20(a and b). As seen in figure 3.20a, heat is generated in the active region and spreads vertically towards the copper heat sink as well as laterally through the electroplated gold heat spreader. We note, that the right-hand side of the mesa in figure 3.20a is cooler than the left-hand side due to it being at a larger distance from the edge of the chip compared to that on the left. In figure 3.20b temperature rise along the facet vertical from the top of the epitaxial region to GaAs substrate is plotted as a function of distance from the epitaxial surface. We averaged the temperature through the 100 μm width of the ridge facet. The waveguide region has the highest temperature, and the temperature falls towards the GaAs substrate as seen in the temperature map. Sharp changes in the vertical scans are mainly due to the differences in the reflectivity of materials that make up the epitaxial layer, and consequently are indicative of different values of thermoreflectance. Thus, sharp peaks delineate the transition between the growth layers (e.g., the peaks on the GaAs substrate side in figure 3.20b are indicative of the epitaxial growth interface).

Joule heating is the main reason for the temperature rise in the active region, and it is inversely proportional to the thermal resistance. Therefore, we calculated the thermal resistance of our lasers by measuring the dissipated power dependent wavelength shift. The thermal resistance can be defined as:

$$R_{th} = \frac{\Delta T}{P_{waste}} = \left(\frac{\Delta\lambda}{\Delta T}\frac{\Delta P}{\Delta\lambda}\right)^{-1} \tag{3.8}$$

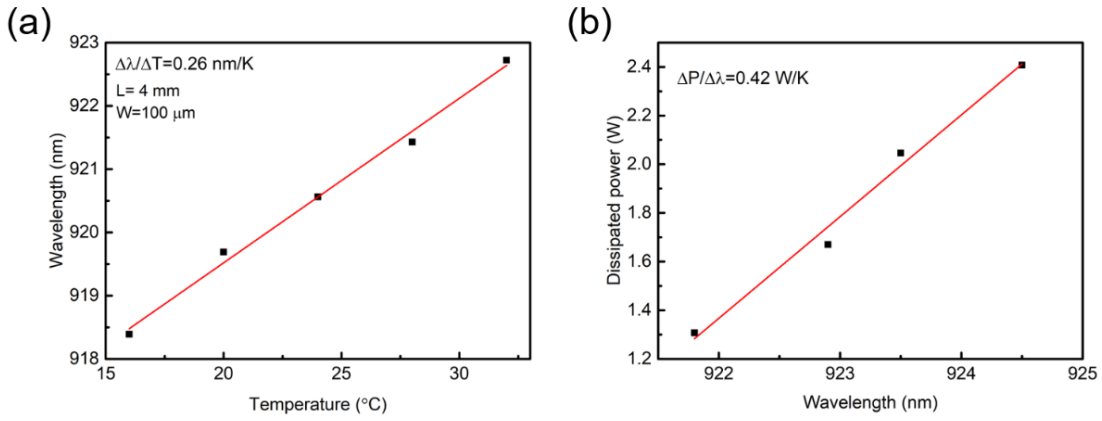

Figure 3.21: (a) Wavelength versus laser temperature and (b) dissipated power versus wavelength.

$\frac{\Delta\lambda}{\Delta T}$ is 0.26 nm/K which is comparable to the data given in literature found from the slope of the line fitted to the wavelength shift as a function of temperature change graph (fig. 3.21a) and $\frac{\Delta P}{\Delta\lambda}$ is determined from the slope of the line fitted to the dissipated power versus wavelength graph as 0.42 (fig. 3.21b). Using these values, we calculated the thermal resistance as 9.2 W/A for 4 mm long laser. Thermal resistance depends on the solder quality; therefore, we measured the thermal resistance for every laser chip.

Chapter 4

Novel concepts for cavity optics

The cavity of a semiconductor laser is a complex environment. Many, some conflicting, requirements need to be met for the most efficient high power operation. The 9xx nm high power lasers under study in this work, are typically used to pump Yb+ ions to generate emission around 1060 nm. High power, high efficiency, long life and reliability are sought after properties. Assuming good crystal growth with low defects and impurities, limiting are the series and thermal resistance of the device dissipating heat with eventual facet failure and damage. Series resistance is controlled through doping of the cladding layers taking care to minimize free carrier absorption. As heat is carried by electrons and phonons, cavity doping and layer thicknesses play a major role. Heat is dissipated via conduction towards the substrate and excellent soldering without pinholes is required to get rid of this excess heat. Facets of the laser, from at least one the output light emerges is most sensitive to excess heat. As the facet is a discontinuity in the cavity, heat accumulating at the interface can not dissipate easily. Further, additional heat is generated at the facets due to excess absorption. Band to band reabsorption as well as absorption through surface defects and contamination result in additional heat load which drives the facet temperature to catastrophic damage at high power densities.

Many successful methods have been used to limit facet heating and eventual

COD. Fundamental to low facet temperature is lowering the optical density incident on the facet. While the width of the laser increases light generated due to recombination, the vertical thickness of the cavity decreases the optical density incident on the facet. However, increased cavity thickness is both costly as well as leading the increased series resistance, despite doping. Current generation of high power 9xx lasers uses large optical cavities reaching to several micron thick cavities, with doped cladding layers for minimum series resistance. Further remedies to facet temperature reduction have been explored.

Non-absorbing mirrors (NAMs) are based on the area- selective bandgap enlarging to reduce facet absorption and performed by quantum well intermixing near laser facet [44, 45, 46]. The aim is to increase band gap difference between the window and the gain region using the impurity-free vacancy disordering to increase the reliability of the lasers because the laser lifetime is correlated with the band gap selectivity [17]. The non-injecting current blocking window is also used to reduce facet absorption by placing the pump region away from the facet. Facet temperature was reduced by a factor of 3-4 for 2 mm long 200 μm wide InGaAs/AlGaAs lasers emitting at 940 nm by decreasing non-radiative recombination rate due to the reduced carrier density with 30 μm long window region [47]. However, lowering the bulk temperature so far, has not been attempted, which is the main contributor to the catastrophic failure by changing the cavity optics as well as reducing the facet temperature. Further innovative approaches are welcome to lower both the cavity and the facet temperature. Making the non-injecting window longer, can decrease the facet temperature lower than bulk temperature because the heat created at the active region can be dissipated through the cold window region. However, longer window region increases optical absorption loss as the light generated internally passes through the non-injecting passive section and degrades the efficiency of the lasers [48]. In this thesis, we report on a new biased window approach to reduce facet temperature below the bulk temperature without degrading laser performance.

4.1 Cavities with cold windows

The unavoidable temperature rise in the active region of the laser is caused by Joule heating. The heat load at the active region can effectively be dissipated vertically towards the epitaxial layer by mounting lasers epi-down and using heat-sinks and laterally with the electroplated Au. A new biased window approach provides heat diffusion along the cavity. In this method, the hot active region is kept far away from the laser facet with a long cold window region which provides the heat dissipation sink. The main limitation is the reduction of the power conversion efficiency of the laser due to the optical absorption losses in cold window region. Absorption losses can be eliminated by making window region transparent by biasing this section. Hence, there will be no penalty on the output power of the lasers. The cavity under study consists of electrically isolated pumped and biased window sections. The window is biased up to the transparency current. Further increase in the bias current can lead to extra heat load. In addition, in like of conventional practice, we defined 50 μm passive unpumped windows reaching out to the back and front facets to prevent facet absorption due to excess carriers. The application of the biased window method is not restricted to InGaAs/AlGaAs lasers, and can be applied to all band to band semiconductor lasers.

4.1.1 Fabrication of biased window high power diode lasers

Biased window high power laser diode fabrication steps are similar to the conventional laser process. As different from the standard laser fabrication, we added an electrical isolation etch step. Before starting the laser fabrication, we designed additional lithography mask for this process. Mask design allows us to characterize 5 mm long conventional lasers and biased window lasers with different window lengths on the same chip. We started the laser process with the cap layer removal

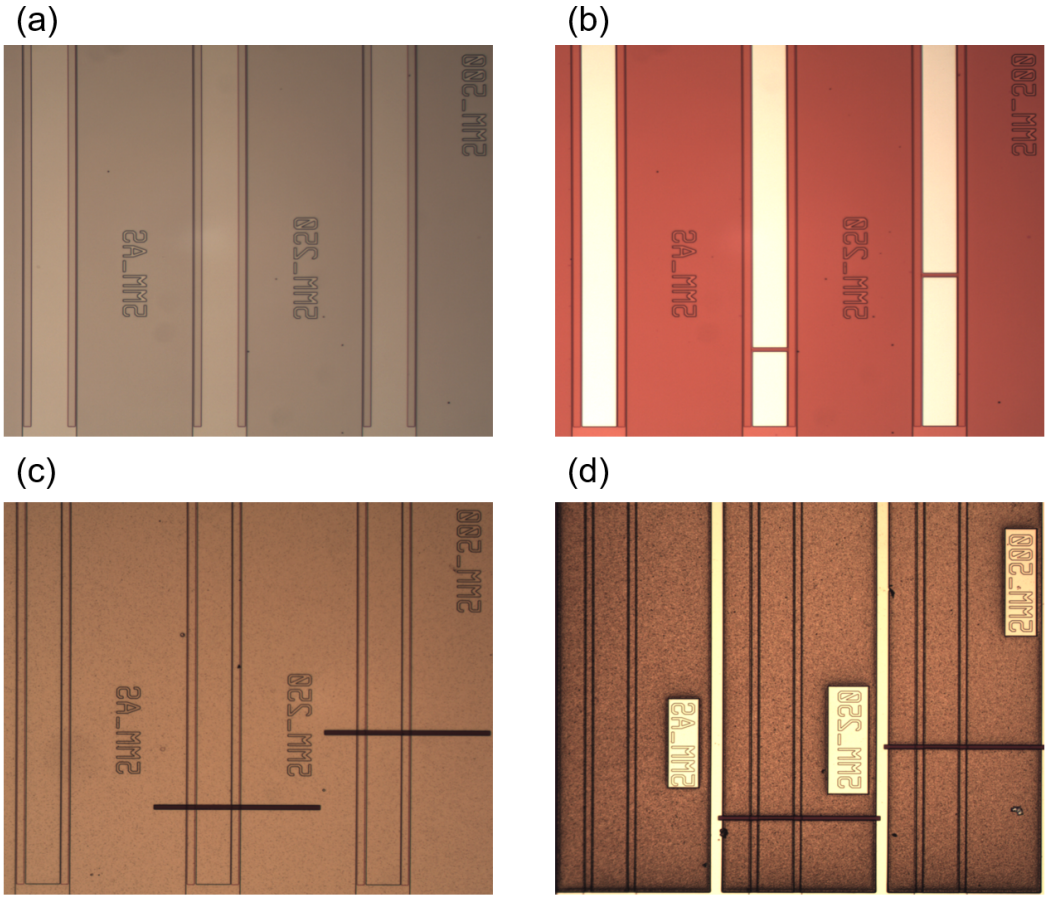

Figure 4.1: The optical microscopy images from the top surface of the biased window high power diode laser after (a) ridge waveguide etch, (b) Si_3N_4 removal from the contact regions (c) lift-off and (d) electroplating.

process. We, then, formed 100 μm wide ridge waveguides by wet etching and followed by 300 nm deep trench etch for electrical isolation between the pumped and biased window sections. We limited the depth of the isolation trench to 300 nm to conserve the mode profile. 200 nm thick dielectric layer (Si_3N_4) was deposited for passivation. After the p-contact windows opening, Ti/Pt/Au was deposited on top of the waveguide regions. Electroplating was performed to increase Au thickness. In figure 4.1(a, b, c and d), the optical microscopy images from the top surface of the biased window high power diode lasers after ridge waveguide etch, Si_3N_4 removal from the contact region, lift-off and electroplating, respectively are shown. After we isolated emitters by wet etching, we defined cleave

markers using same etchant. Series resistance leads to the excess voltage drop and causes heating; therefore laser chips were thinned down to 250 μm on the substrate side. Afterwards, AuGe/Ni/Au was deposited for n- metal contact and alloyed by 420°C RTP process for 1 min. to obtain ohmic contacts. Fabricated lasers were cleaved under optical microscope and mounted epi-up on a copper plate for testing.

4.1.2 L-I-V measurement of biased window high power diode lasers

Figure 4.2 shows the line graph of the voltage versus current between the lasing and window regions of 4.00+ 1.00 mm long biased window laser. We calculated the electrical resistance between the lasing and window regions of biased window laser from the slope of this line as 69Ω which is ∼1000 times of the series resistance of the laser, therefore carrier leakage between the lasing and window region is negligible.

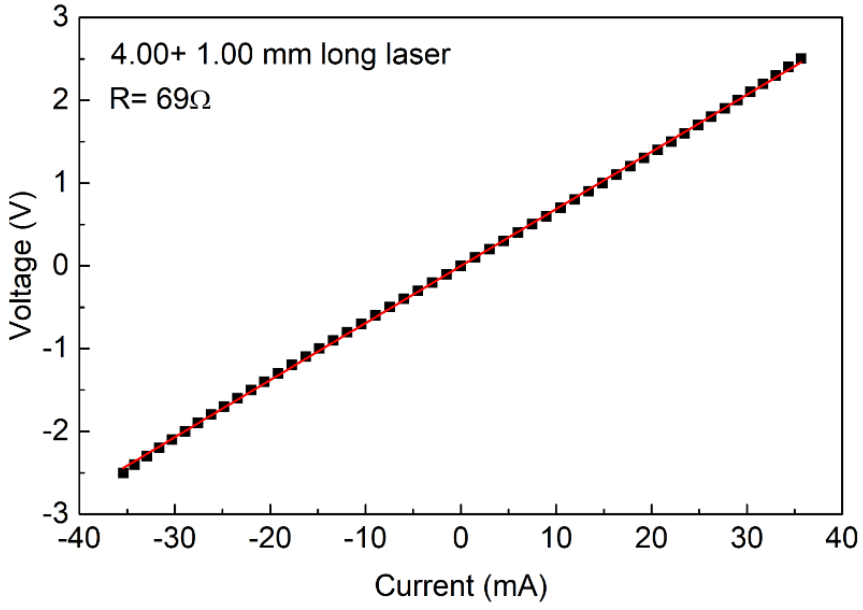

Figure 4.2: The line graph of voltage versus current between the lasing and window region of 4.00+ 1.00 mm long biased window laser.

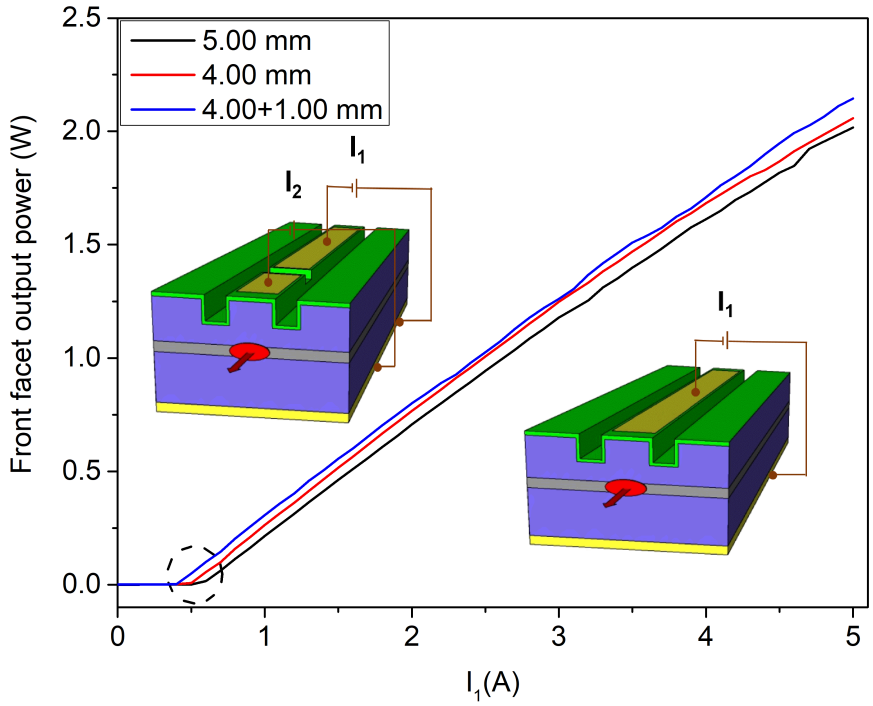

Figure 4.3: The front facet output power at various injection currents for lasers with and without 1.00 mm long window region (window current is at 170 mA). Schematic illustrations of the two different laser designs are also shown (Copyright 2018 IEEE [36]).

In this study, the performance and facet temperatures of the conventional (5.00 mm) x (100 m) broad area high power laser diodes were compared to those of biased window lasers with the same dimensions and on the same chip. In this approach, we varied the length of the biased section to understand its effect on the laser facet temperature. The schematics of the conventional and biased window lasers are shown in figure 4.3 as insets.

Laser performance was analyzed by measuring L-I-V curves for each bias window current (I_2). The front facet power of the 4.00 mm and 5.00 mm long standard lasers and 4.00+ 1.00 mm long-biased window laser at 170 mA biased current as a function of pump current is shown in figure 4.3 to illustrate the biased window laser performance. The output power of 4.00+ 1.00 mm long-biased window laser of 2.15W is higher than that of the 4.00 mm and 5.00 mm long standard lasers of 2.06W and 2.02W, respectively at 5A pumped current. Using the L-I measurements, we calculated the threshold currents and slope efficiencies

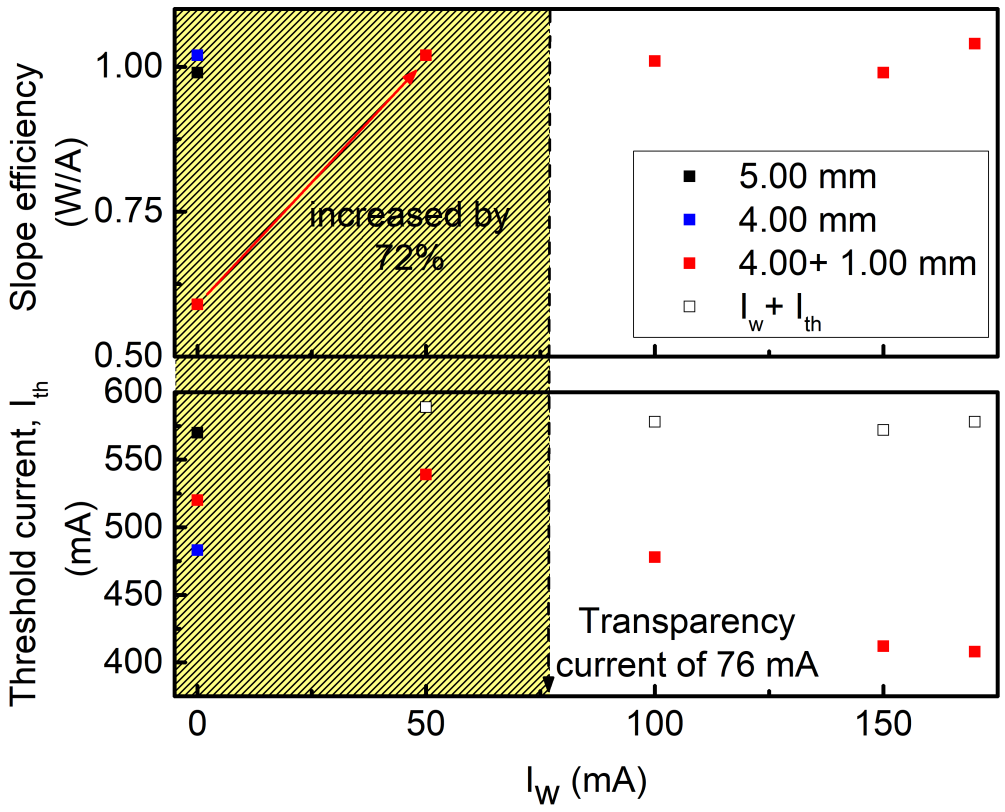

Figure 4.4: The threshold currents and the slope efficiencies of the 4.00 mm and 5.00 mm long standard lasers and biased window lasers for various biasing currents (Copyright 2018 SPIE [43]).

of the standard 4.00 mm and 5.00 mm lasers and biased window lasers for various biasing currents of 50 mA, 100 mA, 150 mA, and 170 mA. The results are shown in figure 4.4. The slope efficiencies of the uncoated lasers calculated by taking twice that of the front facet power. Therefore, the slope efficiencies of the biased window can be a slightly different from our results. The negligible variation does not affect the conclusion of our results. While the slope efficiencies of the standard 4.00 mm and 5.00 mm long lasers are 1.02 W/A and 0.99 W/A, respectively, the slope efficiency results of biased window lasers for various bias currents of 0, 50, 100, 150 and 170 mA are 0.59, 1.02, 1.01, 0.99 and 1.04 W/A, respectively. The data clearly show that zero biased windows have low slope efficiency due to optical loss in this region while the slope efficiency improves in biased window approach ∼72 % by eliminating the optical absorption loss. Loss reduction can

be seen by comparing the threshold currents of the standard 4.00 mm and 5.00 mm long lasers of 480 mA and 570 mA, respectively with 520, 539, 478, 412 and 408 mA threshold currents of biased window laser for different bias currents of 0, 50, 100, 150 and 170 mA, respectively. When we compare unbiased threshold currents of this laser with that of the 4.00 mm long standard laser, window region leads to the 40 mA current loss. The summation of threshold current, I_{th} and window bias current, I_w gives the actual threshold current of the biased window lasers. The threshold current of biased window laser of 589 mA is slightly higher than that of the 5.00 mm long standard laser at below transparency current of 76 mA because the loss is not compensated at this regime.

4.1.3 Facet temperature measurements

We measured the facet temperature changes for various pump currents of standard 5.00 mm long laser and compared the results with that of the 4.00 mm+ 1.00 mm and 4.25 mm+ 0.75 mm long-biased window lasers. In figure 4.5, we show the temperature map of these lasers at 5A pump current in addition to the temperature profiles of these lasers extracted from the temperature maps. The generated heat at active region spreads vertically towards the copper plate and upwards and laterally through the electroplated gold. We found the facet temperature difference of waveguide region by averaging the temperature change through the 100 μm width of the ridge. However, we observe noticeable filament formation in the temperature map of the standard 5.00 mm long lasers whereas there is a dramatic disappearance of filaments in biased window lasers. The averaged temperature difference profile of the ridge from the top surface to the GaAs substrate is shown in figure 4.5d. Our spatial resolution is around 0.7 μm, therefore we analyze the temperature rise of the waveguide including the active region. As seen from the profile, the maximum temperature rise is in the waveguide region, and it decreases towards the GaAs substrate. We can conclude that waveguide temperature reduces with biased window approach and further decreases by increasing the window length of biased window laser. Therefore, we compared the facet temperature changes in 5.00 mm long lasers with that in

4.00+ 1.00 mm long lasers.

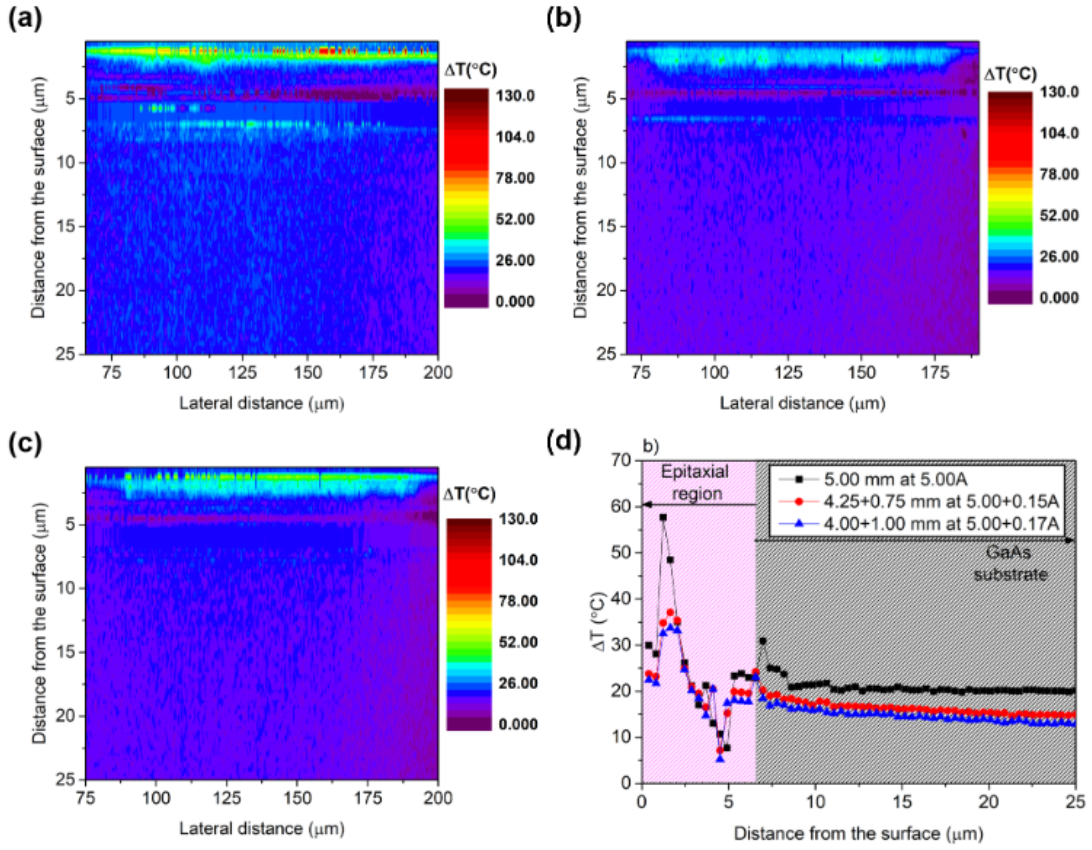

Figure 4.5: The temperature maps of (a-c) 5.00 mm long standard laser, 4.00+ 1.00 mm and 4.25+ 0.75 mm long lasers, respectively and (d) the comparison of the temperature profiles obtained from the map of these lasers at 5A (Copyright 2018 IEEE] [36]).

In figure 4.6, we compared the facet temperature rise of 4.00+ 1.00 mm long biased window laser biased at different current, I_2 of 50, 100, 150 and 170 mA with bulk and facet temperature rise of 5.00 mm long standard laser for various pump current, I_1 of 1A, 3A and 5A. Bulk temperature was calculated from the relation below

$$(\Delta T)_{bulk} = P_{waste} * R_{th} \tag{4.1}$$

where P_{waste} is the dissipated power and R_{th} is the thermal resistance of the

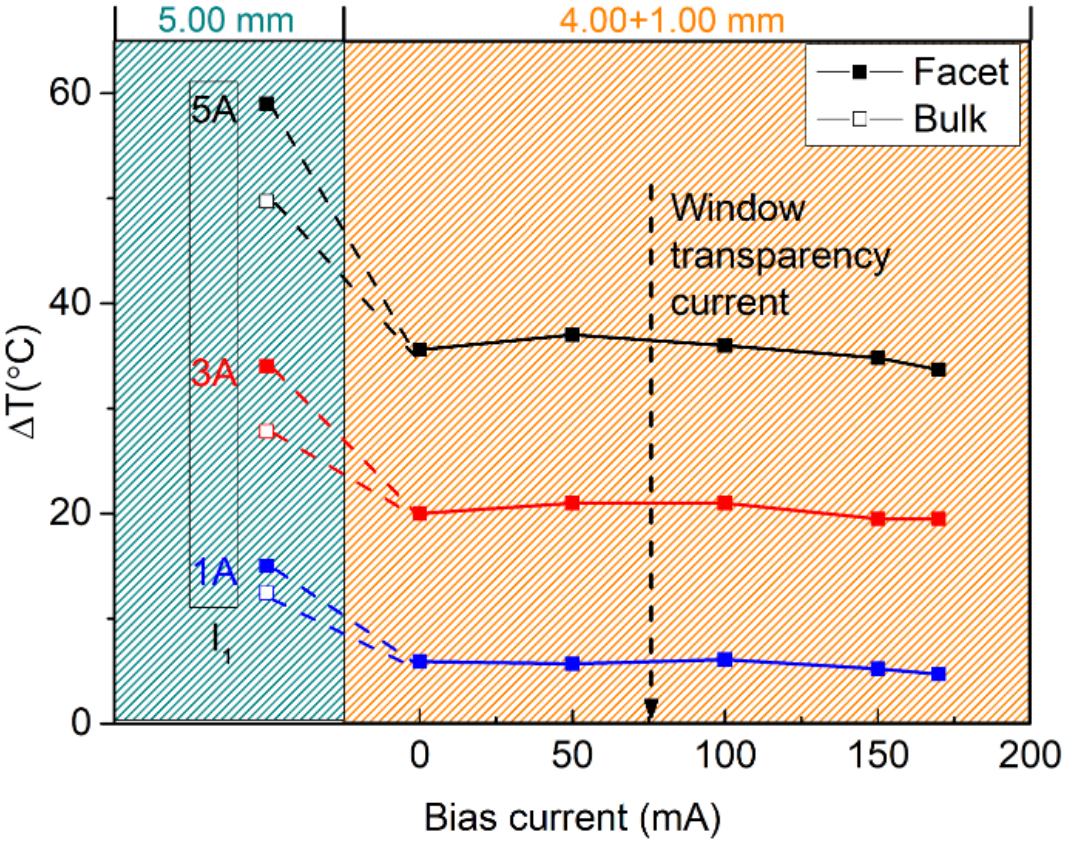

Figure 4.6: The facet temperature rise of 5.00 mm long standard laser and 4.00+ 1.00 mm long biased window lasers as a function of bias current for various pump currents of 1A, 3A and 5A. Bulk temperature rise of standard laser is also shown for these pump currents (Copyright 2018 IEEE [36]).

lasers. The thermal resistance of these lasers was 12.8 K/W which is calculated from the emission wavelength shift of the light as a function of dissipated power, and the bulk temperature of the 5.00 mm long standard laser is found as 12.4 °C, 27.8 °C and 49.7 °C for various I_1 of 1A, 3A, and 5A, respectively. The bulk temperature increases correlated with the operating current due to Joule heating. The facet temperature rise becomes higher than bulk temperature rise due to the facet absorption. The facet temperatures of 5.00 mm long standard laser were measured as 14.7 °C, 33.7 °C and 58.7 °C for various I_1 of 1A, 3A and 5A, respectively. We compared these results with the facet temperature rises of the 4.00+ 1.00 mm long biased window laser for different I_1 and I_2. Although temperature change reduces to 5.9 °C, 20.0 ° and 35.6 ° for I_1 of 1A,

3A and 5A, respectively under unbiased condition, the slope efficiency decreases ∼72%. Therefore, we biased this section up to transparency. The calculated transparency current of 1.00 mm long window is 76 mA. When we bias window below the transparency current, temperature change increases correlated with the Joule heating of window due to the bias current. The bias current of 50 mA is below the transparency current, and it leads to the 69 mW dissipated power corresponds to the 0.9 °C temperature rise. The temperature slightly decreases to 100 mA bias current, which is above the transparency due to the eliminating optical loss. The facet temperature of the 5.00 mm long standard laser was reduced by ∼40% with biased window approach compensating the optical loss of the window at transparency current. Thus, for the first time, facet temperature was decreased far below the bulk temperature (30%) of the laser.

4.1.4 Simulation of facet temperature rise

The bulk temperature of the high power laser diodes increases due to the Joule heating. The heat diffuses laterally and vertically through the electroplated gold spreader and Cu base plate, respectively. By extending the cold laser window, we allow the heat diffusion through the cavity. Our aim is to decrease high facet temperature which leads to the band-gap shrinkage and further facet absorption at high operation current. The thermal resistance prevents the effective heat dissipation and thermal resistance times dissipated power gives the bulk temperature. We simulated the biased window bulk temperature distribution using the heat transfer module of COMSOL. Using the finite element method (FEM), we solve the time-dependent heat diffusion equation derived from the law of conservation of thermal energy, which can be written as shown below

$$\rho C_p \frac{\partial T}{\partial t} + \rho C_p u.\nabla T + \nabla.q = Q + Q_{ted} \tag{4.2}$$

and

$$q = -k\nabla T \tag{4.3}$$

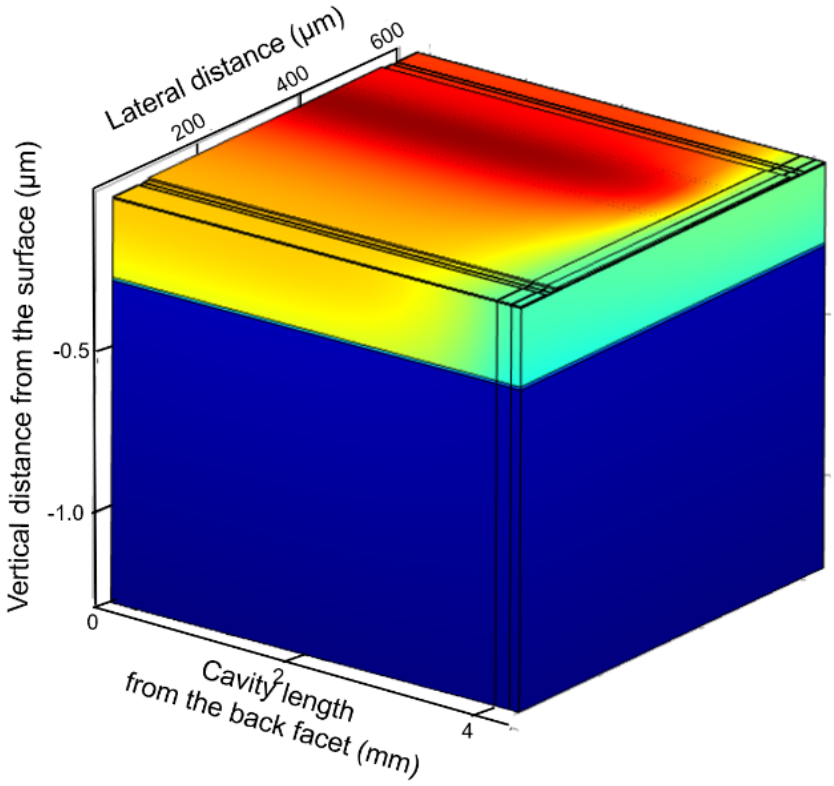

Figure 4.7: (a) Schematic illustration of the COMSOL model.

where $Q + Q_{ted}$ expresses the sum of the heat source per unit volume and the heat flux through the boundary, the material parameters of ρ, C_p and k are the density, heat capacity, and thermal conductivity, respectively; u is the translational velocity of the atoms or molecules. If the velocity is zero, heat transfer is pure conductive. These parameters and boundary conditions are defined in the COMSOL platform. The schematic illustration of the COMSOL model that we used in this study for laser with 250 μm cold window when the dissipated power is 3.88W and the thermal resistance is 12.8 K/W is given in figure 4.7. We assume that there is a heat sink at room temperature at the bottom of the structure and the laser structure is thermally insulated (the heat flux is zero) at the boundary. Besides, a heat source representing the dissipated power is placed in the active region and the thermal conductivity of indium representing the quality of the

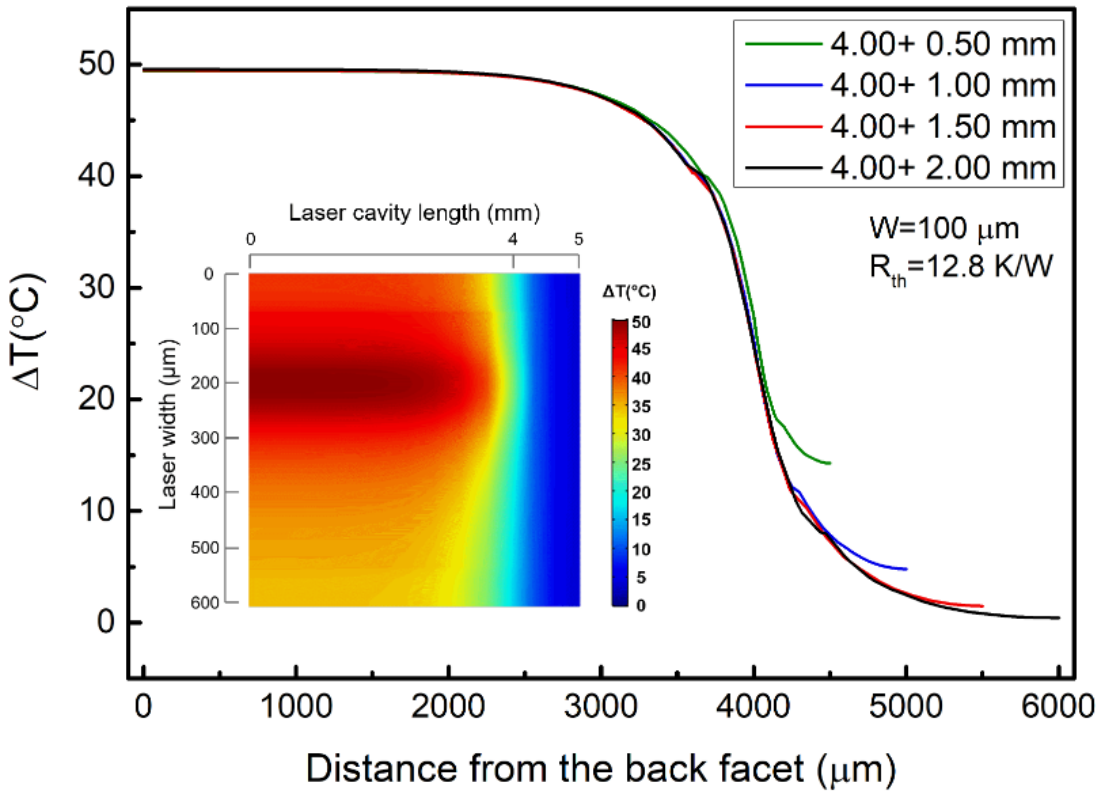

Figure 4.8: The active region temperature change of 4.00 mm long biased window laser with various window length of 500, 1000, 1500 and 2000 μm through the laser cavity. Inset shows the top temperature map of the biased window laser with 1000 μm window length.

mounting process is varied to obtain the experimental bulk temperature values of 5.00 mm long laser for different dissipated powers of 0.96W, 2.17W, 3.88W. These dissipated power values are used from our standard 5.00 mm long lasers under 1A, 3A and 5A operation currents, respectively. The thermal resistance of this laser is experimentally found as 12.8 K/W and the bulk temperatures of this laser under the various operation currents of 1A, 3A and 5A are 12.4 °C, 27.8 °C and 49.7 °C, respectively. The active region temperature variation as a function of distance from the back facet of the biased window lasers with different window lengths of 500, 1000, 1500 and 2000 μm obtained from the simulation for 3.88 W dissipated power and 12.8 K/W thermal resistance is given in figure 4.8. The temperature map of this laser with 1.00 mm long window region is given as an inset of figure 4.8. As seen from the temperature map, the heat generated

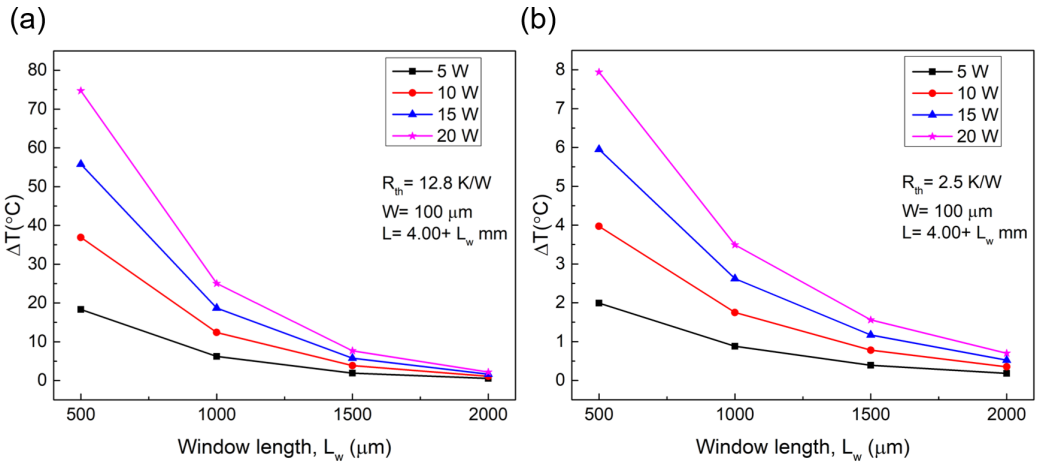

Figure 4.9: (a)The active region temperature change of 4.00 mm long biased window laser with (a) 12.8 K/W (b) 2.5 K/W thermal resistance as a function of window length for various dissipated power of 5W, 10W, 15W and 20W.

by the source diffuses laterally through the gold spreader at the top and longitudinally along the cavity optical axis due to the cold window. The simulated design is similar to lasers fabricated in our laboratory and the asymmetric lateral heat diffusion seen in simulation map is quite similar to the map obtained from the thermoreflectance measurements. Based on these results, we conclude that the bulk of the heat load dissipates towards the cold windows. As the length of the window region increases, the facet temperature decreases, further. In our simulations, the facet absorption is not taken into account as it is difficult to quantify. The computed facet temperature results are, therefore, somewhat below the experimental values. Also, changes in the active region temperature of 4.00 mm long-biased window laser with 12.8 K/W thermal resistance for various dissipated powers of 5W, 10W, 15W and 20W as a function of window length is compared with that of the laser with 2.5 K/W thermal resistance. The results are shown in figure 4.9(a and b). The data suggests that longer windows are required for higher dissipated powers. However, it should be kept in mind that the window length, necessary for a cold facet can also be decreased by reducing the thermal resistance of the lasers as well. Therefore, the smaller window region is expected for epi-down mounted lasers which typically have smaller thermal resistances of around 2.5 K/W.

4.2 Selective band gap engineering

Light emitted deep in the active region can be reabsorbed close to the facets as it exits the cavity. Optical absorption at the facets is known to result in excessive heating eventually leading to COMD. Despite best engineering practices, facets coated with dielectric mirrors contain interface defects which increase absorption of light and dissipate the energy non-radiative increasing the facet temperature. To eliminate this possibility, one approach is to selectively increase the band gap in the vicinity of the facets which requires the inter diffusion of the quantum well atoms with the surrounding waveguide atoms. In InGaAs based lasers, this translates into the inter-diffusion of In and Al atoms, in particular. Local nature of the requirement, limits ways in which the band gap can be locally increased. Conventional window suggests that disorder locally induced by impurities or physical bombardment of the surface with fast ions, can serve as source of point defects which can then act as a sink for inter-diffusion of atoms in the active quantum well region.

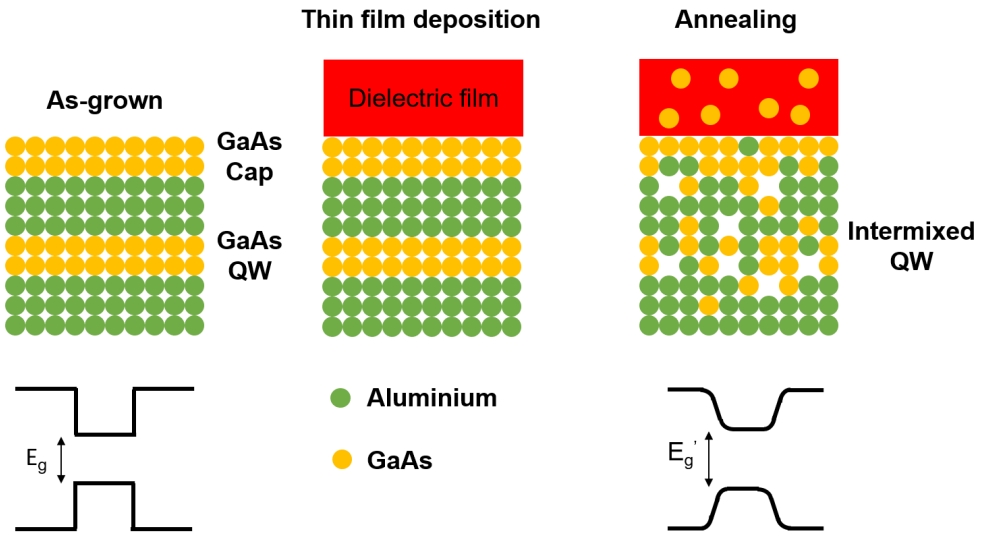

Figure 4.10: Schematic illustration of the IFVD process.

In figure 4.10, we depict how quantum well intermixing (QWI) is used to control band gap energy. In short, interdiffusion of quantum well atoms with

those of the waveguide layer, leads to an quantum well alloy material with larger bandgap. There are many types of processes to achieve QWI such as impurity induced, laser-induced disordering and impurity free vacancy disordering (IFVD). In the case of impurity induced vacancy generation, added impurities can lead to free carrier absorption as well as bound to continuum recombination and non-radiative recombination. In this work, we used IFVD to enlarge bandgap near the laser facets. The schematic illustration of the IFVD process is shown in figure 4.10. The advantage of the IFVD is that there is no impurity induced recombination centers in the laser structure as well as no impurity induced free carrier absorption. In this process, Ga atoms out-diffuse into the dielectric layer leaving vacancies behind depending on temperature. The out-diffusion of the Ga atoms provide inter-diffusion of Ga-Al. In the case of InGaAs QW structure, In is also out-diffuses into the waveguide region. IFVD is a two-step process, and inter-diffusion of Ga-Al and out-diffusion of In is highly stress dependent [49, 50]. Atoms' diffusions are promoted when the GaAs cap of laser structure is under compressive stress during the RTP process whereas it is inhibited when the cap layer under tensile stress [51]. As a result, intermixing can be controlled by stress management.

IFVD can be a area selective process. While we would like to increase the band gap in the vicinity of the facets, we do not want changes to the band gap in the rest of the cavity. We, thus, need to find suitable dielectrics to enhance IFVD near the facets at window region as well as to suppress it at the gain region of the lasers. The high power laser reliability increases with the band-gap difference, ΔE between the window and gain region [17]. In this work, we used SiO_2 thin films for the intermixing region and bilayer of Si_xO_2: SrF_2 films for the suppression region.

4.2.1 Photoluminescence measurements of the band gap shift

Photoluminescence spectroscopy is an excellent probe of radiative recombination processes in semiconductors. When applied to semiconductor laser materials, it can be a sensitive probe of the recombination wavelength. The e-hh transitions in the InGaAs quantum well leads to the lasing wavelength of these lasers. As such, PL spectroscopy can track the shifts in the e-hh transitions after each QWI process. To estimate the degree of QWI, we measured the photoluminescence (PL) of the samples at room temperature using optical spectrum analyzer(OceanOptics HR200+, spectral wavelength 190-1100 nm, resolution 0.04 nm) and Ar^+ laser at 514 nm was used for excitation. PL from a quantum well is a sensitive probe of the changes that occur in the quantum well. Blue shift of the PL wavelength is indicative of band gap widening.

The literature suggests that band-gap shift via IFVD based on a two step mechanism, which are the creation of Ga vacancies and diffusion of Ga vacancies away from the dielectric-GaAs interface to the inside of the epitaxial layers. The vacancies inside the dielectric film enhances the out-diffusion of Ga atoms from GaAs layers to the dielectric film whereas second mechanism is stress dependent. When the GaAs layer is under compressive stress, intermixing becomes thermodynamically more favorable [52]. The degree of intermixing not only depends on the annealing parameters such as rapid thermal annealing (RTA) temperature and annealing duration but also the properties of the dielectric encapsulant like stoichiometry and thickness. The PECVD deposited stoichiometric SiO_2 is used to enhance intermixing [44]. The vacancies inside the dielectric film can be adjusted by changing the deposition parameters of the PECVD. Data in the literature demonstrates that the refractive index of Si_xO_2 increases as the voids inside the film decreases. They assume that stoichiometric SiO_2 does not contain voids. The denser Si_xO_2 film with higher refractive index than the stoichimetric SiO_2 is obtained with negative voids [44, 53]. Refractive index can, thus be used as a rough means of monitoring the chemical composition of the films. We also note that associated with the chemical composition and vacancy concentrations

of the films, stress is generated by the film. Hence, Si content of Si_xO_2 films also affect the magnitude and sign of the stress associated with these films. However, we do not deduce the level of intermixing as a function of the Si_xO_2 film stress. We aim to increase PL shift for the QWI using SiO_2 for intermixing and silicon-rich silicon dioxide films (Si_xO_2) and SrF_2 films for the suppression. Thin films of SiO_2 and (Si_xO_2) used in this work were deposited by PECVD using 2% SiH_4 in He. The reports in the literature show that the denser films were obtained under the deposition condition of 20W radio frequency (RF) power and 300 °C deposition power [44]. Hence, we analyzed the refractive index of Si_xO_2 deposited by PECVD under 20W RF power 300 °C temperature at one torr base pressure for 2 min. by varying the flow rate to obtain denser, high refractive index dielectric film.

The refractive index analysis was performed by the spectroscopic ellipsometer (V-VASE). Ellipsometer measures the s and p polarized Fresnel reflectivities of the light at the Brewster angle. The ratio of the Fresnel reflectivities of the s and p polarized light is expressed as below [54]

$$\frac{r_p}{r_s} = tan(\Psi).e^{(i\Delta)} \tag{4.4}$$

where Ψ is the amplitude ratio and Δ is the phase difference of s and p polarized light. The Ψ and the Δ depend on the optical properties and the thickness of the materials. The measured Ψ and Δ profiles as a function of the wavelength are fitted to the data generated by the model of material system to find the thickness and the optical constants of the materials. The Cauchy is the typical fit model to analyze the thickness and the optical properties of the dielectric materials [55]. Hence, we used the Cauchy model for the analysis of SiO_2 and Si_xO_2. As an illustration, the ellipsometer model with the model parameters, the measurement and fit profiles of Ψ and Δ for Si_xO_2 film deposited using 210 sccm SiH_4(He) and 800 sccm N_2O and the refractive index profiles of this film are given in figure 4.11. The Cauchy model is well fitted to the experimental data of Ψ and Δ and the refractive index of this film changes from the 1.53 to 1.57 from 400 nm to 1200 nm. It is 1.54 at 630 nm. The measured refractive indices of Si_xO_2 for various

deposition flow rate are given in the table 4.1.

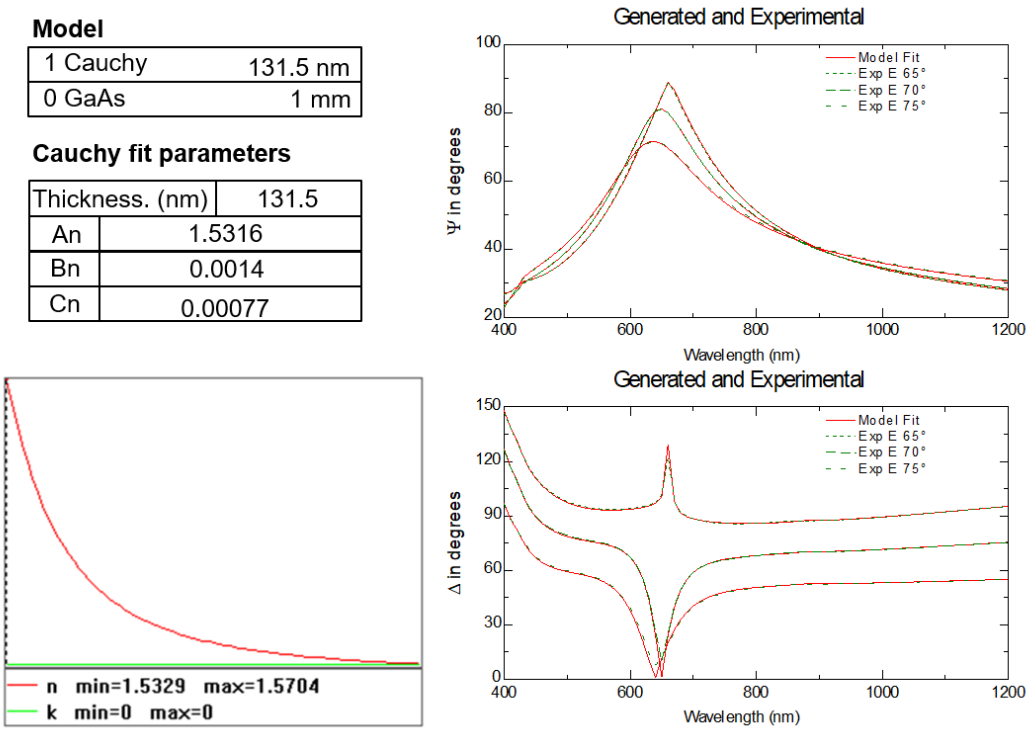

Figure 4.11: An example for the ellipsometer model and model parameters used to analyze the thickness and the optical properties of the Si_xO_2 and the measurement and fit profiles of the Ψ and Δ are given. Also, refractive index profiles obtained from the fit is shown.

After refractive index and thickness characterization, we analyzed the PL spectra of 250 nm SiO_2 (n=1.460), Si_xO_2 (n=1.57) deposited by PECVD and thermal evaporation of SrF_2 (1.38) annealed at various temperatures of RTA. We tried to obtain stoichiometric SiO_2 (n=1.45) to increase intermixing because the intermixing increases with the increasing amount of voids in the Si_xO_2; however it was limited by PECVD flow rate. To make the material deposition similar to IFVD process of lasers, 250 nm SiO_2 used for intermixing deposited on the same epitaxial laser structure with the dielectric film used for suppression either Si_xO_2 or SrF_2. The schematics of the two different sample configuration is shown in figure 4.12. The process steps up to PL measurements are as follows:

1. Solvent cleaning under ultrasound: In acetone (ACE) at 50 °C for 5 min.,

Table 4.1: Refractive index analysis of PECVD deposited SiO_2 and Si_xO_2

Thin film material	Flow rates (sccm)	Refractive index
SiO_2	SiH_4(He): N_2O 27:1000	1.46
Si_xO_y	SiH_4(He): N_2O 50:1000	1.48
Si_xO_y	SiH_4(He): N_2O 100:800	1.50
Si_xO_y	SiH_4(He): N_2O 210:800	1.54
Si_xO_y	SiH_4(He): N_2O 320:800	1.57

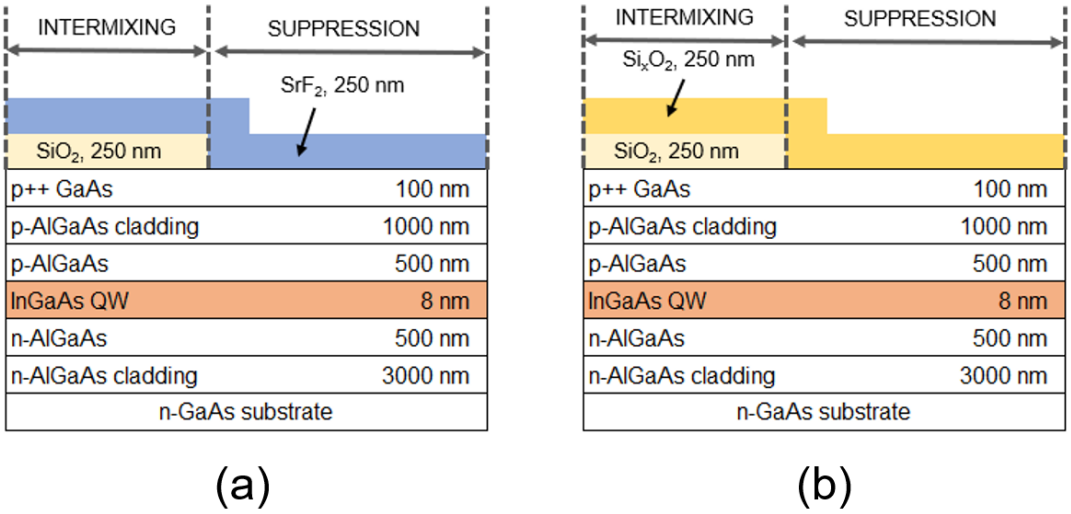

Figure 4.12: Intermixing and suppression configuration used for comparison of PL wavelength shift of 250 nm SiO_2, SrF_2 and Si_xO_2.

in isopropanol (IPA) at 50 °C for 5 min. and deionized water (DI).

2. Surface oxide removal: Etch in HCl:H_2O (1: 10) at room temperature for 20 sec.

3. Dielectric film deposition for intermixing: SiO_2 by PECVD.

4. Photo-resist covering on the half of the sample

5. Dielectric film etches: SiO_2 etch in NH4F: HF (7: 1) or buffered oxide etch (BOE).

6. Photo-resist strip and the oxygen plasma etch in the reactive ion etch (RIE) for 1 min. at room temperature.

In the RIE process, the oxygen flow rate and RF power were 10 sccm and 51W, respectively.

7. Dielectric film deposition for suppression: SrF_2 deposition by thermal evaporation or Si_xO_2 deposition by PECVD.

8. Annealing for intermixing: RTA process under various temperature and duration.

9. Dielectric removal for PL measurements: Sr_2 etch in $HCl:H_2O$ (1: 10) (or Si_xO_2 etch in BOE) and SiO_2 etch in BOE.

10. Crystal etch down to p-cladding to increase PL intensity: $\sim$1 μm etch in H_3PO_4: H_2O_2: H_2O (1: 4: 45).

As an illustration, the normalized PL spectra of the as-grown and SiO_2, Si_xO_2 and SrF_2 capped samples annealed at 880 °C for 2 min. are given in figure 4.13. In each spectra, ground state and higher order transitions are seen starting from the long wavelength transition of interest to shorter wavelength which are not amplfied in the laser. The dominant transition for lasing is the ground state; therefore we analyze the evaluation of ground state peak on the IFVD process parameters. We did not take account of the spectral responsivity of the monochromator because our aim is to measure the relative PL intensity at room temperature, not to determine the absolute value of the PL intensity. The ground state PL peak wavelength of the as-grown sample is at 902 nm whereas it is at 900 nm, 887 nm and 867 nm for SrF_2, Si_xO_2 and SiO_2, respectively.

We annealed the samples using a rapid thermal processsor at various temperatures of 860, 880, 900 and 920 °C for 2 min. in nitrogen ambient. During the RTA process, samples were sandwiched between the two pieces of GaAs wafers to prevent As out-diffusion from the sample surfaces. We used dielectric film thicknesses ranging from 100 to 300 nm. It is known that the PL wavelength shift is proportional with the dielectric thickness as the total number of vacancies increase with thickness [57]. In our experiments, we find that the PL wavelength shift saturates at around 250 nm for SiO_2 films. Therefore, the layers deposited

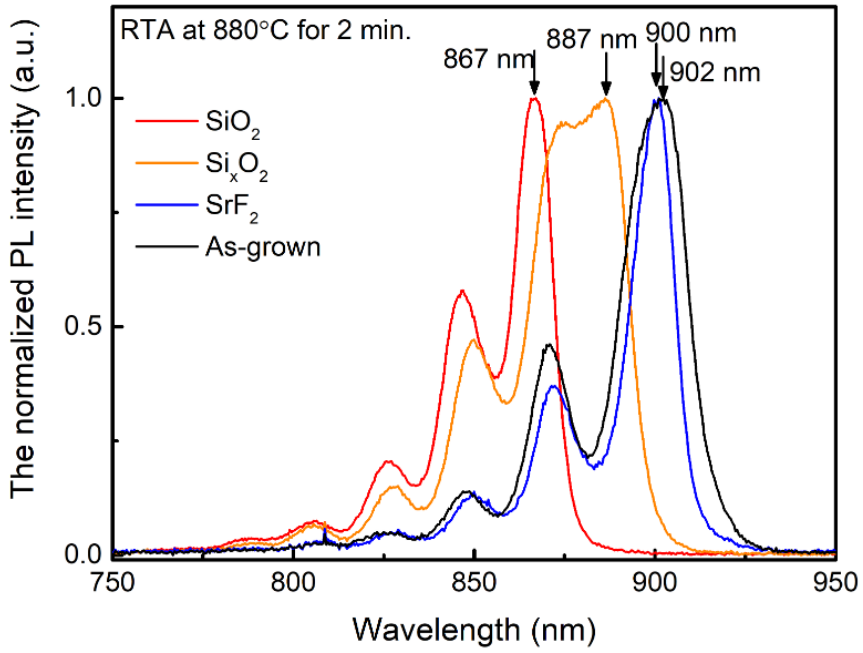

Figure 4.13: The normalized PL spectra of the as-grown and SrF_2, Si_xO_2, SrF_2 capped samples under RTA annealing condition of 880°C for 2 minutes (Copyright 2018 IOP [56]).

on SiO_2 does not affect the PL wavelength shift due to intermixing. The PL peak wavelength shift as a function of annealing temperature for 250 nm SiO_2, Si_xO_2 and SrF_2 are given in figure 4.14. Based on the results obtained from the PL analysis, we find that wavelength shift increases with annealing temperature as reported in the literature [45, 58]. Increasing PL shift is known to be related to enhanced Ga out-diffusion at high temperatures. The smallest PL wavelength shift is obtained when SrF_2 capping is used, which makes SrF_2 a good candidate for suppression of disordering. The maximum PL wavelength difference, $\Delta\lambda$ of 70 nm (corresponding band-gap difference, ΔE is 120 meV) was obtained between the SiO_2 and SrF_2 capped regions at 920 °C. However, at this annealing temperature SrF_2 films do not preserve the PL emission wavelength in the gain region where PL emission wavelength makes a 17 nm blue shift. We, therefore, tried annealing at lower temperatures. We find that the maximum temperature at which there is no observable defect formation is 880 °C when SrF_2 films are used. We find that the PL wavelength shift due to SiO_2 and SrF_2 are 35 nm and 2 nm, respectively. As a result, the $\Delta\lambda$ (ΔE) obtained via SiO_2 and SrF_2 capping

for intermixing and suppression, respectively is 33 nm (52 meV).

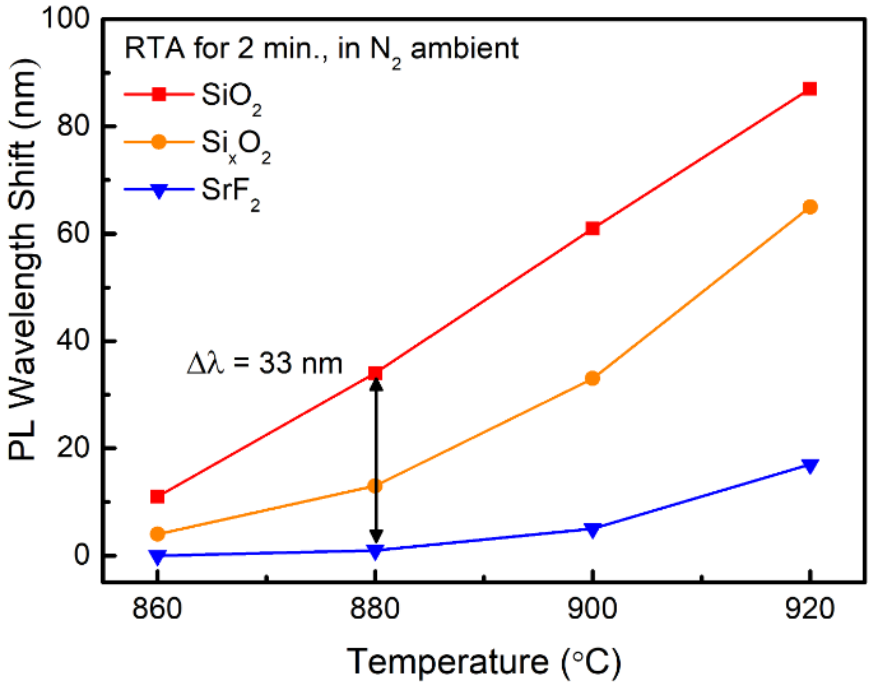

Figure 4.14: PL peak wavelength shifts under RTA annealing conditions of 860 to 920°C for 2 minutes (Copyright 2018 IOP [56]).

Defect free processes are a critical requirement in fabrication of semiconductor devices. It is essential that surfaces remain free of defects after each fabrication step. We analyzed the surface quality of RTA processed samples under optical microscopy after the dielectric film is removed. Surface defects are non-radiative recombination centers which cause the degradation of laser performance and reliability. The images obtained from the sample surfaces are shown in figure 4.15, the results reveal that there are several surface defects on SrF_2 capped sample surfaces even for the smallest SrF_2 thickness of 5 nm whereas the SiO_2 and Si_xO_2 surfaces are free of defects. To investigate the reason of surface damages, microscopy images of SrF_2 were examined before dielectric etch and RTA process. The optical microscopy images taken from this analysis are given in figure 4.16. No surface damage was observed before the RTA process. Surface damage was detected only after the RTA process. These results suggest that thermal stress induces surface damage during the annealing in RTP. We, therefore, tried to reduce thermal stress, without penalty on gain and negligible PL wavelength shift.

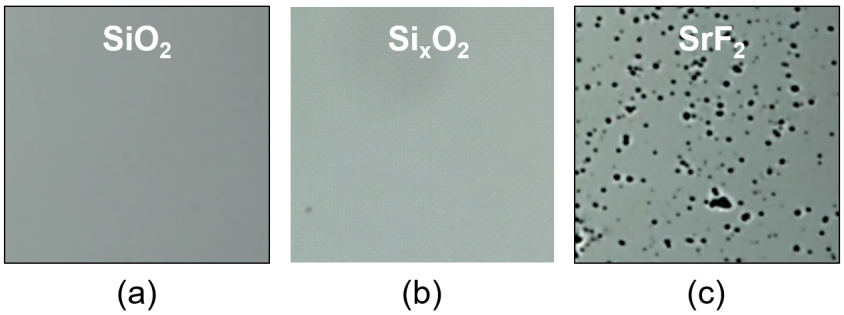

Figure 4.15: The optical microscopy images of a) SiO_2, b) Si_xO_2 and c) SrF_2 film covered surfaces, respectively, obtained from the sample surfaces after the removal of dielectric films (Copyright 2018 IOP [56]).

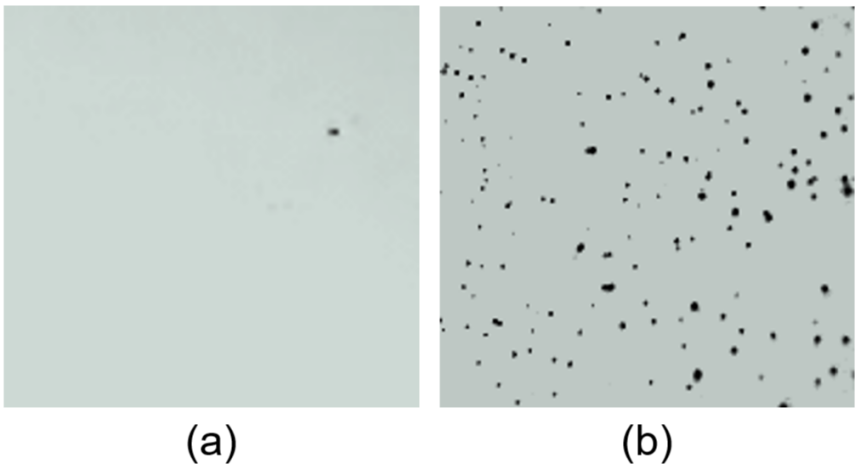

Figure 4.16: The optical microscopy images of SrF_2 surfaces (a) after film deposition (b) after RTP process of the sample.

To decrease thermal stress in the suppression region, the thickness of the SrF_2 films were reduced down to 30 nm and a thin layer of Si_xO_2 was deposited before SrF_2 layer deposition. A thin Si_xO_2 layer of 10 nm was used to prevent the PL wavelength shift. This was also enough to prevent surface damage, as shown below. The new configuration is shown in figure 4.17. We analyzed the surface quality after RTA process under the same conditions. Optical microscopy images are obtained from the suppression region, which consists of Si_xO_2: SrF_2 (10 nm: 30 nm). The apparent surface quality improvement was observed as indicated in figure 4.18(a and b). Using atomic force microscopy, we compared the root mean

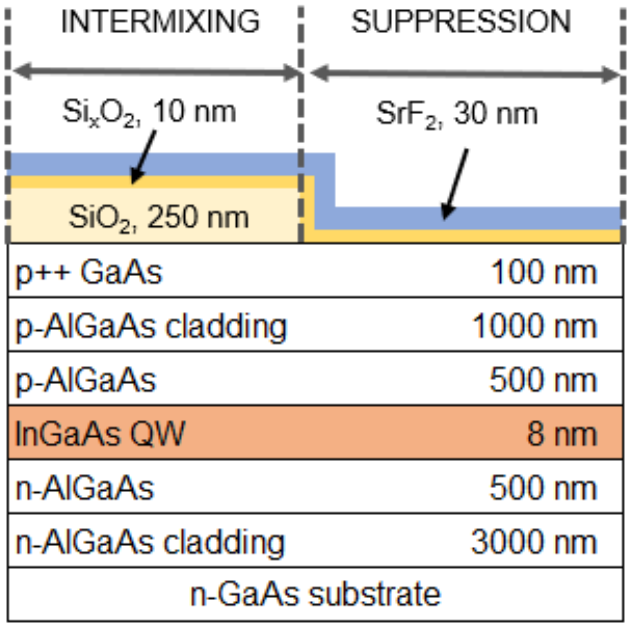

Figure 4.17: Bilayer configuration to decrease thermal stress.

square (rms) roughness of the SrF_2 deposited sample with a bilayer of Si_xO_2: SrF_2 deposited sample after dielectric etch process. The results of these measurements are given in figure 4.18(c and d). The modification of the rms roughness seen from these images. Surface roughness for SrF_2 is 10 nm, whereas it is 2 nm for Si_xO_2: SrF_2.

Table 4.2: The thermal stress of various materials and the physical parameters used to calculate stress (Copyright 2018 IOP [56]).

Material	α (ppm $^{\circ}C^{-1}$)	$E_f/(1-\nu_f)$ (GPa)	σ_{in} (GPa)	$\Delta\alpha.\Delta T$	σ_{th} (GPa)	σ_{total} (GPa)
Si_xO_2	1	120	-0.2	-0.5%	0.6	+0.4
SrF_2	28	110	0	+1.8%	-2.1	-2.1
GaAs	7	-	-	-	-	-

We did not have a possibility to measure the thermal stress of the dielectric films during the RTA process. Therefore, in the following, we try to make rough estimation for thermal stress of the dielectric films at a given temperature using the as deposited film parameters. The total thermal stress and the mechanical parameters that are used to calculate the total thermal stress is given in table 4.2 for Si_xO_2, SrF_2 and GaAs substrate. The SrF_2 films impose extensive compressive

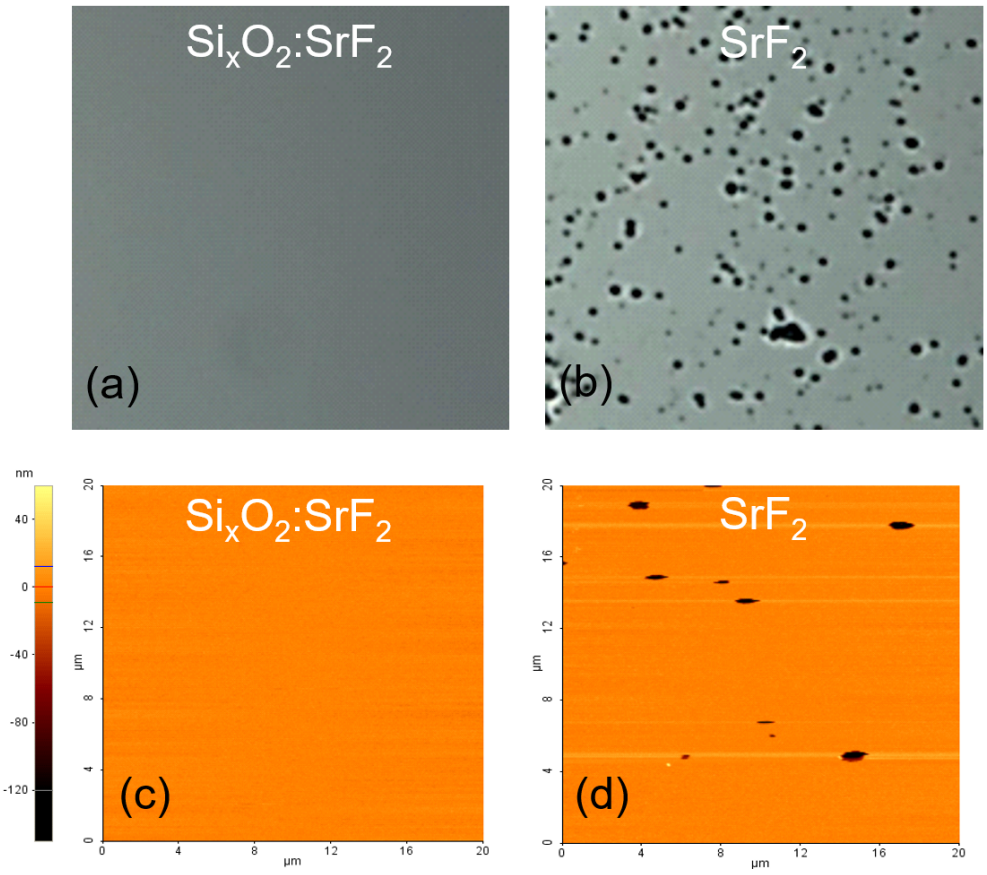

Figure 4.18: The comparison of the optical microscopy and AFM measurement results of the Si_xO_2: SrF_2 and SrF_2 capped samples after dielectric film etch process (Copyright 2018 IOP [56]).

stress on the epitaxial structure due to the large thermal expansion coefficient difference between GaAs and SrF2 films. We calculated thermal stress using the relation below [59, 60]:

$$\sigma_{th} = (\frac{E_f}{1-\nu_f}) * \Delta\alpha\Delta T \tag{4.5}$$

where E_f and ν_f are the Young modulus, and Poisson coefficient of the dielectric film, respectively and $\Delta\alpha$ expresses the thermal expansion coefficient difference between the dielectric film and GaAs substrate. This compressive stress due to the large thermal expansion coefficient mismatch between the SrF_2 (CTE $\sim$ 18 ppm°C^{-1} at 20 °C and $\sim$ 31 ppm°C^{-1} at annealing temperature of 880 °C) and GaAs (CTE $\sim$ 18 ppm°C^{-1} at 880 °C) is -2.1 GPa. Therefore, GaAs is under

tensile stress, which leads to the suppression of the disordering. We measured the intrinsic stress of Si_xO_2 as -0.2 at room temperature after PECVD film deposition using a surface profilometer to calculate the total stress, as explained in the next paragraph. The minus sign indicates compressive stress whereas positive sign expresses tensile stress. Although the intrinsic stress of the Si_xO_2 is compressive, it becomes tensile after annealing due to the thermal expansion coefficient difference (CTE is $\sim$ 1 ppm $^{\circ}C^{-1}$ for Si_xO_2 at 880 °C). When we compare the total stress of -2.1 for SrF_2 with that of +0.4 for Si_xO_2, we can conclude that SrF_2 imposes high compressive stress to the laser structure. In bilayer configuration, Si_xO_2 acts as a barrier against the high thermal expansion of SrF_2 to protect the surface. Moreover, Si_xO_2 becomes compressively stressed under SrF_2 during the RTP. Therefore, GaAs is tensile-stressed during intermixing in the bilayer configuration of Si_xO_2: SrF_2.

The intrinsic stress measurement technique with surface profilometer utilizes the radius of curvature of the substrate before and after the film deposition. After measurements of the curvatures, the intrinsic film stress is calculated using the relation below [61]:

$$\sigma_i = (\frac{E_s}{6(1-\nu_s)})\frac{(t_s)^2}{t_f}(\frac{1}{R_f} - \frac{1}{R_s}) \tag{4.6}$$

where E_s is the Young modulus, ν_s is the Poisson coefficient of the substrate, t_s and t_f are the thickness of the substrate and film, respectively and R_s and R_f are the radius of curvature before and after the film deposition, respectively.

The normalized PL spectra of the as-grown and SiO_2: Si_xO_2: SrF_2 and Si_xO_2: SrF_2 capped samples annealed at 880 °C for 2 min. are given in figure 4.19. The ground state PL peak wavelength of the as-grown sample is at 902 nm whereas it is at 896 nm for Si_xO_2: SrF_2 used in the suppression of disordering and 867 nm for SiO_2: Si_xO_2: SrF_2 used in intermixing.

The PL peak wavelength shift due to SiO_2: Si_xO_2: SrF_2, Si_xO_2, Si_xO_2:SrF_2 and SrF_2 capped samples annealed at various temperatures of 860, 880, 900 and

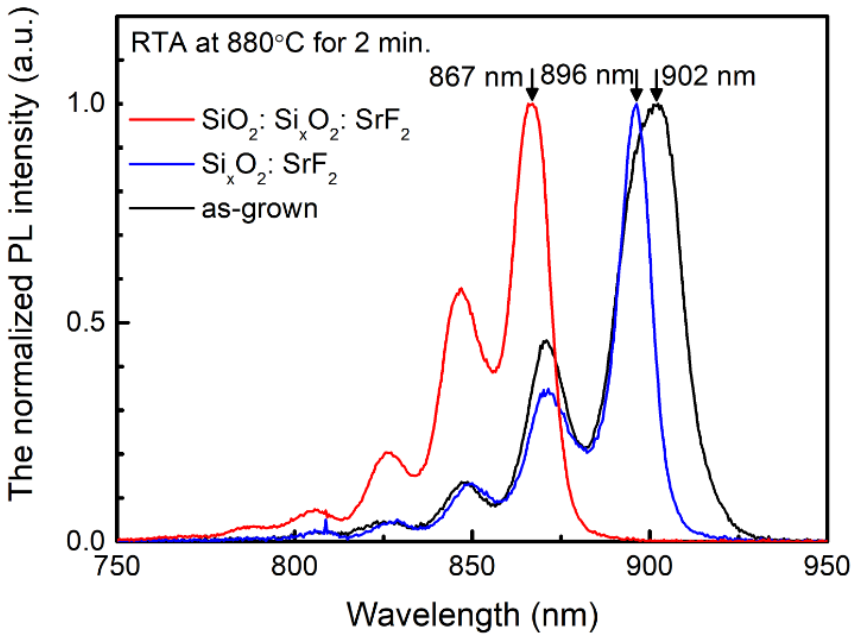

Figure 4.19: The normalized PL spectra of as-grown and SiO_2: Si_xO_2: SrF_2 and Si_xO_2: SrF_2 capped samples annealed at 880 °C for 2 min. (Copyright 2018 IOP [56]).

920°C are given in figure 4.20. We improved the suppression of disordering with Si_xO_2: SrF_2 films when compared with the results of Si_xO_2 films. When we compare the PL wavelength shift of Si_xO_2: SrF_2 capped samples with that of the SrF_2 capped samples, similar band-gap difference of 29 nm instead of 33 nm due to SrF_2 capped samples at 880 °C annealing temperature for 2 min. was obtained. We, therefore, conclude that, the bilayer dielectric structure is a good candidate for suppression of intermixing by preserving surface quality.

Figure 4.21(a and b) shows the ground state full-width at half-maximum (FWHM) and integrated PL intensity as a function of the RTA temperature. PL peak FWHM provides information about the homogeneity of QW thickness and integrated PL intensity gives significant clues about the deep level defects created during the IFVD process due to the Ga-vacancies. There is no noticeable change in between the FWHM of the SiO_2: Si_xO_2: SrF_2 and Si_xO_2: SrF_2 capped samples and they are not changes with temperature indicating that the roughness caused by defects is negligible. However, integrated PL intensity of

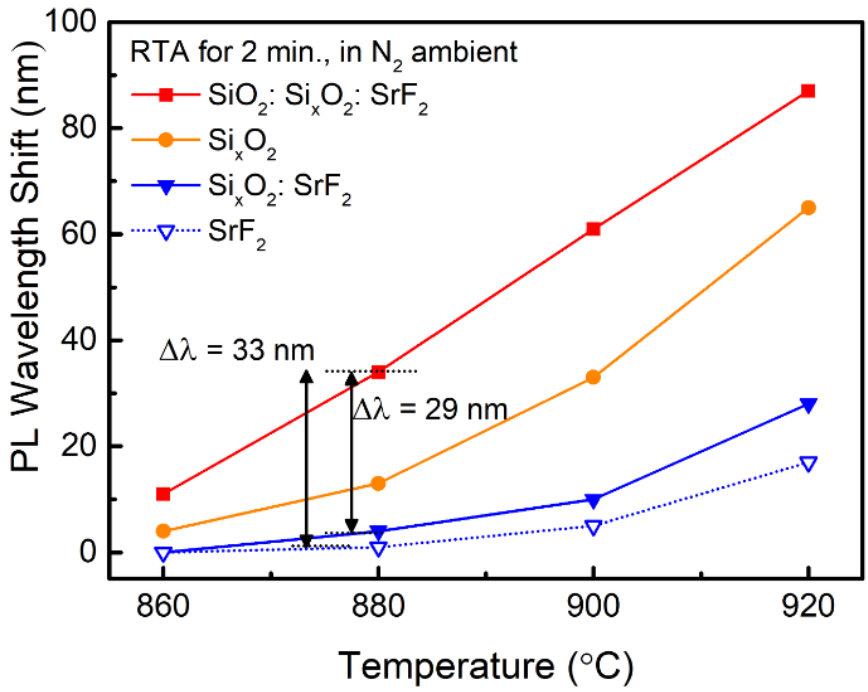

Figure 4.20: The PL peak wavelength shift of SiO_2: Si_xO_2: SrF_2, Si_xO_2, Si_xO_2: SrF_2 and SrF_2 capped samples annealed at various temperatures of 860, 880, 900 and 920°C (Copyright 2018 IOP [56]).

the SiO_2: Si_xO_2: SrF_2 capped samples decreases as a function of temperature because intermixing increases with temperature and it creates the deep-level defects at the active region of the sample. Deep-level defects lead to the non-radiative recombination through deep interband levels created by Ga-vacancies during the IFVD process. The slightly increasing integrated PL intensity of the Si_xO_2: SrF_2 capped samples can be due to the reduced lattice damage with temperature.

To increase wavelength difference between the SiO_2: Si_xO_2: SrF_2 and Si_xO_2: SrF_2 capped samples, we extended the annealing time at 880 °C. Fig. 4.22 shows PL spectrum comparison of as-grown with SiO_2: Si_xO_2: SrF_2 and Si_xO_2: SrF_2 capped intermixed and suppressed regions, respectively at the maximum PL wavelength difference condition of 6 min. annealing time. PL peak wavelength of the suppressed region of Si_xO_2: SrF_2 is 900 nm negligibly blue shifts, but its linewidth was reduced. The separation between the ground state and higher order state is smaller due to the modified band-structure after RTA process as shown in the

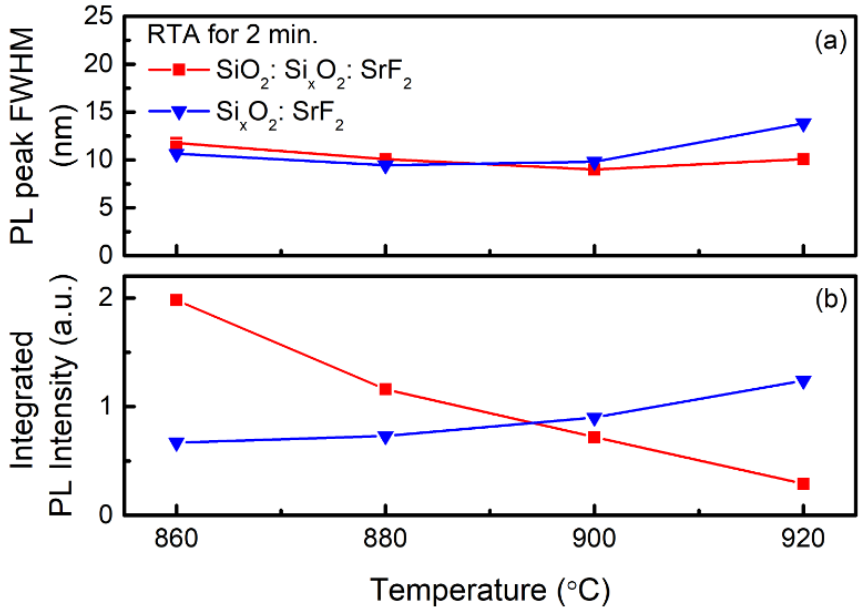

Figure 4.21: (a) The FWHM and (b) integrated PL intensity of SiO_2: Si_xO_2: SrF_2 and Si_xO_2: SrF_2 capped samples annealed at 880 °C for 2 min. (Copyright 2018 SPIE [62]).

IFVD process description in which the square-like well becomes gaussian-like. The PL peak wavelength of SiO_2: Si_xO_2: SrF_2 capped intermixed region is at 825 nm which is around the saturation wavelength for SiO_2.

Figure 4.23 shows the effect of extended time RTA on PL wavelength shift. As the time extends, the wavelength shift of Si_xO_2: SrF_2 capped region increases correlated with the Ga-vacancies provided by the SiO_2. At 8 min. annealing time, Si_xO_2: SrF_2 does not prevent the wavelength shift and at this annealing time the PL wavelength shift of SiO_2: Si_xO_2: SrF_2 approaches the saturation. However, at 6 min., suppression region preserve the wavelength and intermixing is around maximum value. Therefore, the optimum PL wavelength shift of 75 nm (125 meV) between these samples are obtained at 6 min. annealing time. Thus, we achieved a record high PL wavelength difference between the intermixed and suppressed regions.

Figure 4.24 shows the ground state FWHM and the integrated PL intensity

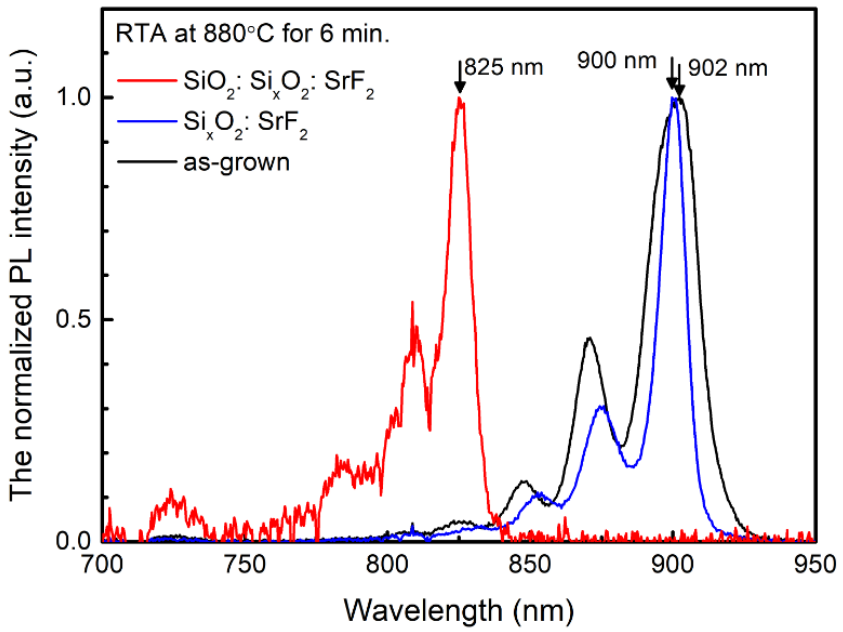

Figure 4.22: The normalized PL spectra of SiO_2: Si_xO_2: SrF_2 and Si_xO_2: SrF_2 capped regions after RTA process at 880 °C for 6 min. compared to as-grown structure (Copyright 2018 IOP [56]).

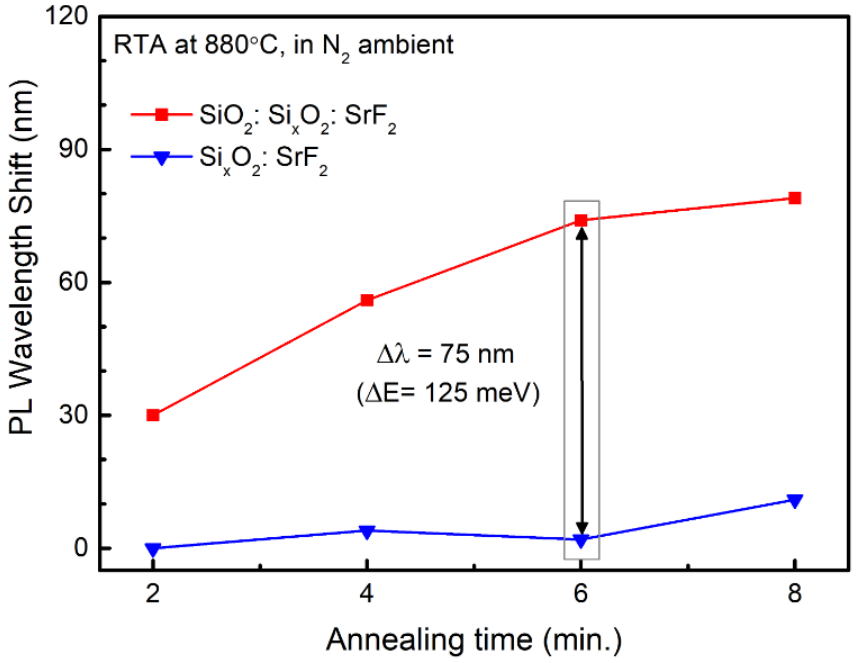

Figure 4.23: PL peak wavelength shift under annealing conditions of 2 to 8 min. at 880°C (Copyright 2018 IOP [56]).

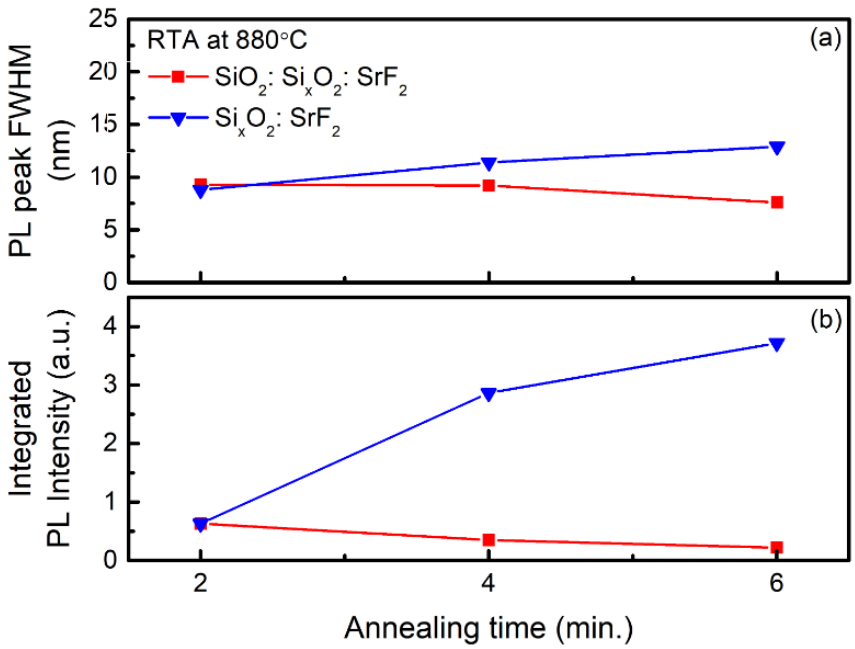

Figure 4.24: The FWHM and integrated PL intensity of intermixed and suppressed regions at 880 °C from 2 to 6 min. (Copyright 2018 SPIE [62]).

change as a function of RTA annealing time. The ground state FWHM of suppression region increases with time possibly due to the contribution of the higher order transitions because as we indicated that the separation between the states decreases depending on the QW band-structure evolution during the RTP process. A small decrease of FWHM in the intermixed region is possibly to be due to high energy tail of the shallower confinement with larger QWI blueshift. The PL intensity of intermixed region decreases with annealing time correlated with non-radiative recombination related to the Ga-vacancies as indicated in figure 4.21b. The suppression region improvement by increased annealing time is evident with substantial PL intensity increase.

4.2.2 Fabrication of lasers with IFVD

Based on the detailed investigation of the processes described above, we fabricated broad area laser diodes with 3, 4 and 5 mm long cavity and 100 μm wide ridge waveguides to study the applicability of the developed IFVD method. We

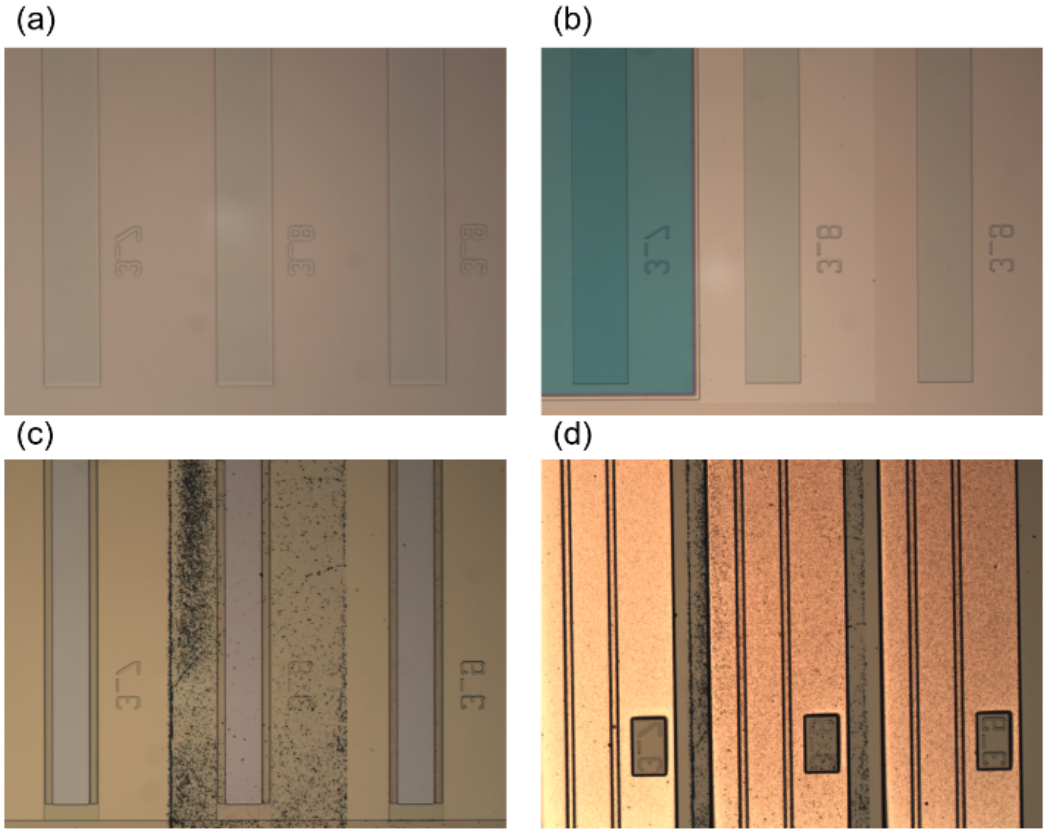

Figure 4.25: The optical microscopy images of the lasers after (a) cap layer removal (b) dielectric film deposition (c) Si_3N_4 removal from the contact regions and (d) electroplating.

compared the performance of the various types of RTA processed lasers fabricated on the same chip with standard laser. Therefore, following the cap layer removal etch, various types of dielectrics which are 250 nm SiO_2, bilayer of 10 nm Si_xO_2 and 30 nm SrF_2 and single layer of SrF_2 are initially fully covered on the waveguide regions of the different lasers and lasers are annealed at 880 °C for 4 mins. for intermixing and suppression before standard laser fabrication without cap layer removal etch. In figure 4.25(a and b), the optical microscopy images of these lasers after cap layer removal and dielectric film deposition, respectively are given. In figure 4.25b from the left, emitters covered by three layers of $SiO_2/Si_xO_2/SrF_2$, single layer of SrF_2 and bilayer of Si_xO_2/SrF_2, respectively are shown. After the RTA process, we applied standard laser fabrication processes. In figure 4.25(c and d), the optical microscopy images from the top surface of the lasers after

the Si_3N_4 removal from the contact region and electroplationg, respectively are shown. Whereas the surface of bilayer of Si_xO_2/SrF_2 deposited laser is clean, the defects on single layer of SrF_2 covered laser are clearly seen. After the laser fabrication, lasers are mounted epi-up on a copper plate for testing.

4.2.3 Spectrum of lasers

We measured the above threshold lasing spectrum of the SiO_2: Si_xO_2: SrF_2 and Si_xO_2: SrF_2 capped lasers and compared the lasing wavelength shift with PL wavelength shift in figure 4.26. The lasing wavelength shift of 45 nm (equivalent to 70 meV) is approximately equal the PL wavelength shift of 44 nm. Under this RTA condition, the peak wavelengths for Si_xO_2:SrF_2 layer protected laser is comparable to as-grown devices shown in the experimental section of this work.

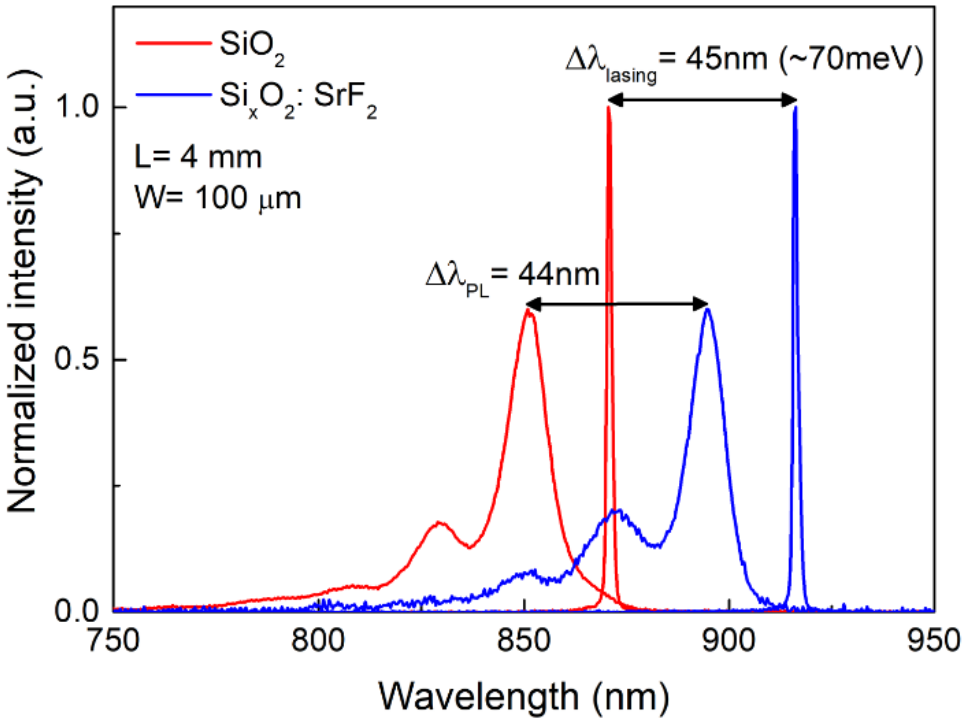

Figure 4.26: The normalized PL and lasing spectra of the Si_xO_2: SrF_2 capped suppression and SiO_2 capped intermixing lasers as a results of 4-minute annealing at 880 °C (Copyright 2018 IOP [56]).

4.2.4 L-I-V measurements of lasers with IFVD

The effects of the different dielectrics on laser performance were analyzed based on the L-I-V measurements of lasers with IFVD. In figure 4.27, we compared the CW output powers and threshold currents of the 4 mm long and 100 μm width SiO_2: Si_xO_2: SrF_2 capped laser for intermixing, bilayer of Si_xO_2 and SrF_2 and single layer of SrF_2 deposited for suppression with that of the corresponding as-grown laser. In table 4.3, we give the threshold current and slope efficiency results of these lasers calculated from the current dependent output power. The threshold current of bilayer Si_xO_2: SrF_2 of 520 mA is comparable with that of the as-grown laser of 480 mA. However, it is very high for SrF_2 capped lasers due to the stress-induced defects which lead to the non-radiative recombination loss. The threshold current increase associated with stress-induced defects is higher than that caused by the corruption of QW due to the intermixing. The slope efficiency of the as-grown laser did not change much with the bilayer film. However, the slope efficiency of SrF_2 and SiO_2: Si_xO_2: SrF_2 of 0.82 and 0.65, respectively are very low compared with that of the as-grown laser.

Table 4.3: Threshold current, slope efficiency and differential quantum efficiency of different lasers

Type of laser	The threshold current (mA)	The slope efficiency (W/A)	Differential quantum efficiency
as-grown	480	1.02	76%
Si_xO_2: SrF_2	520	0.91	67%
SrF_2	770	0.82	61%
SiO_2	600	0.65	46%

The internal loss and internal efficiency of the as-grown and bilayer Si_xO_2: SrF_2 were extracted from the slope and intercept of the line graph of inverse external differential efficiency versus cavity length which is given in figure 4.28. The internal loss and internal quantum efficiency of as-grown laser are 0.39 cm^{-1} and 86%, respectively whereas they slightly differ to 0.54 cm^{-1} and 80% for Si_xO_2: SrF_2, respectively. However, we could not obtain the consistent results from the SrF_2 lasers to make loss analysis, and these lasers were failed at low operation currents. The comparable internal loss and efficiency and repeatable results of

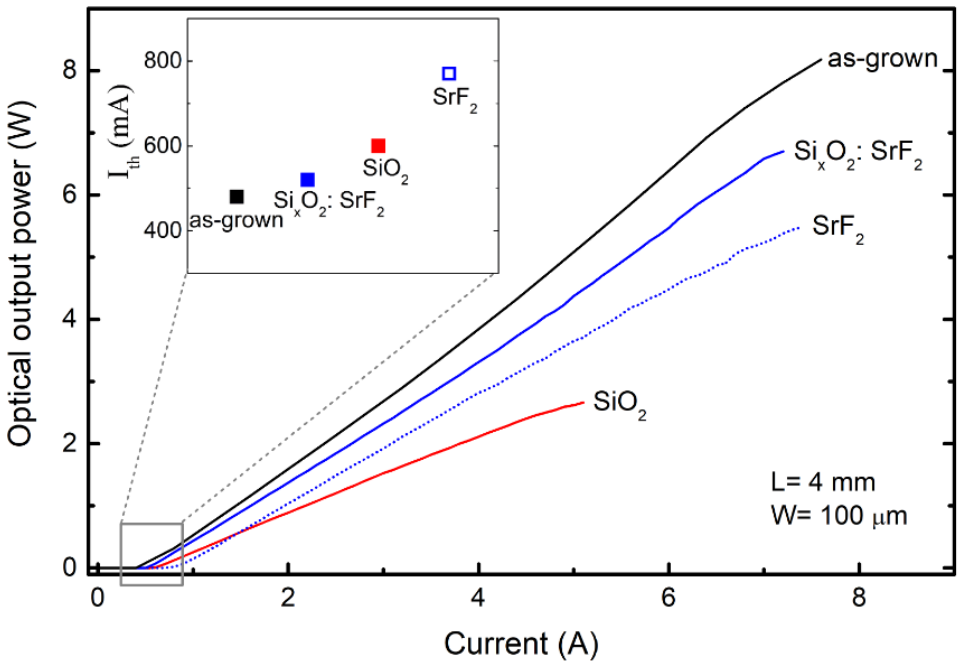

Figure 4.27: The CW output power of the SiO_2, SrF_2, Si_xO_2: SrF_2 and as-grown lasers. Inset shows the threshold currents of these lasers (Copyright 2018 IOP [56]).

the Si_xO_2: SrF_2 lasers with as-grown lasers demonstrate the significant impacts of stress management in IFVD based laser performance.

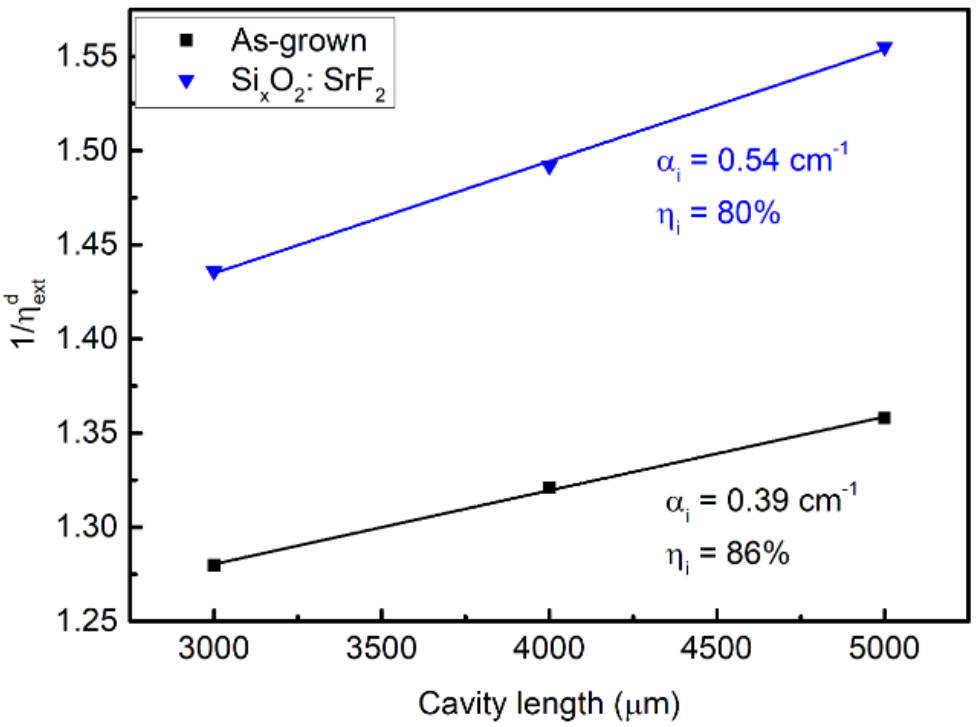

Figure 4.28: Inverse external differential quantum efficiency of the Si_xO_2: SrF_2 and as-grown lasers as a function of cavity length (Copyright 2018 IOP [56]).

Chapter 5

Conclusions and future work

The aim of this work was to demonstrate novel concepts which allow increasing COMD threshold. To this effect, two approaches were undertaken. On the one hand, we increased the local band gaps in the vicinity of the facets while employing a three electrode design to keep the facets cold. Thus, we designed, microfabricated and characterized both conventional and biased window lasers, as well as lasers with selective band gap engineering near the facets.

We fabricated high power broad area ridge waveguide lasers with 100 μm ridge width and the various cavity length of 3.00, 4.00 and 5.00 mm. We optimized the micro-fabrication processes for different types of lasers. In addition, we developed mounting and soldering techniques to improve the heat dissipation which is crucial for laser lifetime and reliability.

We built the experimental setups for pulsed and cw electro-optical measurements. In addition, we constructed a far-field measurement set-up using galvo mirrors and a photodiode.

In order to have a better understanding of cold facet formation as well as the best design parameters, we modeled heat dissipation in biased window lasers using heat transfer module of the COMSOL. This shows that facet temperature decreases as the biased window length increases. We, also show that smaller

window lengths are needed for the laser with low thermal resistance. We fabricated 100 μm width and 5.00 mm long biased window lasers with various window lengths ranging from 0.75 mm and 1.00 mm. We compared the performance of the 4.00+ 1.00 mm long biased window lasers with that of the 4.00 mm and 5.00 mm long conventional lasers when the window was biased up to 170 mA which is beyond transparency current of the 1.00 mm long window section. The threshold current of the 4.00 mm long conventional laser is smaller and the slope efficiency of this laser is higher than that of the 5.00 mm long conventional laser as expected. The threshold current and slope efficiency of the biased window lasers were shown to be slightly better at 170 mA bias current. We built a thermoreflectance set-up to map the facet temperature distribution of the lasers. We compared the temperature of the waveguide region including active region of the 5.00 mm long laser with that of the 4.25+ 0.75 mm and 4.00+ 1.00 mm long biased window lasers at 5A pump current. We conclude that the biased window approach allows decreasing the facet temperature and which decreases further as a function of the window length. We analyzed the performance of the biased window lasers as a function of the bias current. At zero bias condition, although the facet temperature of the 4.00+ 1.00 mm long laser is $\sim$40% below that of the 5.00 mm long conventional laser, the front facet power of the laser decreases 40% due to the absorption loss of the window region. When the window biased at transparency current or above, the laser power becomes similar or slightly higher than that of the conventional 5.00 mm long laser.

During selective band gap engineering of the facet region for larger band gaps, we used the SiO_2 thin films for intermixing and a special bilayer of Si_xO_2: SrF_2 for the suppression of intermixing instead of single layers SrF_2 thin films which causes cracking and defect formation due to high thermal stresses associated with the dielectric/semiconductor interface. We found that high tensile stresses on the laser epitaxial layer exists, based on stress measurement using the profilometer. Through photoluminescence measurements, we could track band gap shifts between intermixed and suppressed regions. We optimized the layer thicknesses of SiO_2, Si_xO_2 and SrF_2 as 250 nm, 10 nm and 30 nm, respectively and the RTA conditions of 880°C for 6 min. to obtain high band gap difference between the

intermixed and suppressed region. Record high band gap difference of 75 nm (125 meV) was achieved. We fabricated 100 μm width and 3.00, 4.00 and 5.00 mm long conventional lasers and RTA processed lasers using 250 nm SiO_2, 30 nm single layer of SrF_2 and bilayer of Si_xO_2: SrF_2 under the 880°C 4 min. RTA process to demonstrate the stress management in IFVD process. We compared the performance of 4.00 mm long conventional laser with that of the 4.00 mm long RTA processed lasers. The threshold current, the slope efficiency and the differential quantum efficiency of the conventional laser are 480 mA, 1.02 W/A, and 76%, respectively. The corresponding values for SiO_2 deposited lasers are 600 mA, 0.65 W/A and 46 %, for SrF_2 are 770 mA, 0.82 W/A and 61% and for Si_xO_2: SrF_2 are 520 mA, 0.91 W/A and 67%. Thus, we show that laser performance of the SrF_2 deposited laser, which had deteriorated due to crack formation can be overcome using the bilayer of Si_xO_2: SrF_2 resulting in comparable laser performance with conventional lasers. The internal loss and internal quantum efficiency of the conventional lasers are 0.39 cm^{-1} and 86%, respectively and corresponding values for bilayer deposited RTA processed lasers are 0.54 cm^{-1} and 80%, respectively.

Further work is going to be focused on the improvement of the laser output power, hence the COMD threshold with epi-down mounting and facet dielectric coating of the biased window lasers. The sub-mount for biased window lasers need to be designed. Epi-up lasers have higher thermal resistance which causes heating of the active region. The window coating is needed to passivate the mirror surface and decrease the non-radiative recombination further. In the case of IFVD process, the stress associated with dielectric/semiconductor interface and its components can be further optimized to increase in the band gap even larger while keeping the surface quality high as achieved in this work, in line with the findings in the literature that the larger the band gap difference the longer is the lifetime. The output power can be increased with the coherent beam combining or vertical stacking of the lasers.

Bibliography

[1] S. L. Chuang, *Physics of Photonic Devices*. WILEY, 2009.

[2] P. W. Epperlein, *Semiconductor Laser Engineering, Reliability and Diagnostics*. WILEY, 2013.

[3] J. I. Pankove, *Optical Processes in Semiconductors*. Courier Corporation, 1975.

[4] R. Diehl, *High-power diode lasers fundamentals, technology, applications*. Springer, 2000.

[5] P. Crump, G. Blume, K. Paschke, R. Staske, A. Pietrzak, U. Zeimer, S. Einfeldt, A. Ginolas, F. Bugge, K. Häusler, P. Ressel, H. Wenzel, and G. Erbert, "20w continuous wave reliable operation of 980nm broad-area single emitter diode lasers with an aperture of 96m," in *High-Power Diode Laser Technology and Applications VII* (M. S. Zediker, ed.), SPIE, feb 2009.

[6] H. Wenzel, P. Crump, A. Pietrzak, C. Roder, X. Wang, and G. Erbert, "The analysis of factors limiting the maximum output power of broad-area laser diodes," *Optical and Quantum Electronics*, vol. 41, pp. 645–652, jul 2009.

[7] P. Crump, H. Wenzel, G. Erbert, and G. Tränkle, "Progress in increasing the maximum achievable output power of broad area diode lasers," in *High-Power Diode Laser Technology and Applications X* (M. S. Zediker, ed.), SPIE, feb 2012.

[8] B. S. Ryvkin and E. A. Avrutin, "Effect of carrier loss through waveguide layer recombination on the internal quantum efficiency in large-optical-cavity laser diodes," *Journal of Applied Physics*, vol. 97, p. 113106, jun 2005.

[9] D. A. Vinokurov, V. A. Kapitonov, A. V. Lyutetskiĭ, N. A. Pikhtin, S. O. Slipchenko, Z. N. Sokolova, A. L. Stankevich, M. A. Khomylev, V. V. Shamakhov, K. S. Borshchev, I. N. Arsent'ev, and I. S. Tarasov, "Saturation of light-current characteristics of high-power laser diodes (= 1.0–1.8 m) under pulse operation," *Semiconductors*, vol. 41, pp. 984–990, aug 2007.

[10] A. Pietrzak, P. Crump, H. Wenzel, R. Staske, G. Erbert, and G. Tränkle, "55 w peak power from 1100 nm wavelength 60 μm broad-area laser diodes enabled by reduced carrier accumulation in the waveguide," *Semiconductor Science and Technology*, vol. 24, p. 035020, feb 2009.

[11] H. Wenzel, P. Crump, A. Pietrzak, X. Wang, G. Erbert, and G. Tränkle, "Theoretical and experimental investigations of the limits to the maximum output power of laser diodes," *New Journal of Physics*, vol. 12, p. 085007, aug 2010.

[12] D. A. Vinokurov, V. A. Kapitonov, A. V. Lyutetskiĭ, D. N. Nikolaev, N. A. Pikhtin, A. V. Rozhkov, N. A. Rudova, S. O. Slipchenko, A. L. Stankevich, N. V. Fetisova, M. A. Khomylev, V. V. Shamakhov, K. S. Borshchev, and I. S. Tarasov, "Studying the characteristics of pulse-pumped semiconductor 1060-nm lasers based on asymmetric heterostructures with ultrathick waveguides," *Technical Physics Letters*, vol. 32, pp. 712–715, aug 2006.

[13] P. Ressel, G. Erbert, U. Zeimer, K. Hausler, G. Beister, B. Sumpf, A. Klehr, and G. Trankle, "Novel passivation process for the mirror facets of al-free active-region high-power semiconductor diode lasers," *IEEE Photonics Technology Letters*, vol. 17, pp. 962–964, may 2005.

[14] D. C. Hall, L. Goldberg, and D. Mehuys, "Technique for lateral temperature profiling in optoelectronic devices using a photoluminescence microprobe," *Applied Physics Letters*, vol. 61, pp. 384–386, jul 1992.

[15] D. Pierścińska, "Thermoreflectance spectroscopy—analysis of thermal processes in semiconductor lasers," *Journal of Physics D: Applied Physics*, vol. 51, p. 013001, nov 2017.

[16] P. K. L. Chan, K. P. Pipe, J. J. Plant, R. B. Swint, and P. W. Juodawlkis, "Temperature mapping and thermal lensing in large-mode, high-power laser diodes," *Applied Physics Letters*, vol. 89, p. 201110, nov 2006.

[17] H. Naito, T. Nagakura, K. Torii, M. Takauji, H. Aoshima, T. Morita, J. Maeda, and H. Yoshida, "Long-term reliability of 915-nm broad-area laser diodes under 20-w CW operation," *IEEE Photonics Technology Letters*, vol. 27, pp. 1660–1662, aug 2015.

[18] A. Pietrzak, *Realization of High Power Diode Lasers with Extremely Narrow Vertical Divergence*. PhD thesis, Technischen Universität Berlin, 2011.

[19] M. Ziegler, M. Hempel, H. E. Larsen, J. W. Tomm, P. E. Andersen, S. Clausen, S. N. Elliott, and T. Elsaesser, "Physical limits of semiconductor laser operation: A time-resolved analysis of catastrophic optical damage," *Applied Physics Letters*, vol. 97, p. 021110, jul 2010.

[20] M. Hempel, J. W. Tomm, M. Ziegler, T. Elsässer, N. Michel, and M. Krakowski, "Catastrophic optical damage at front and rear facets of 975 nm emitting diode lasers," in *CLEO:2011 - Laser Applications to Photonic Applications*, OSA, 2011.

[21] J. Tomm, M. Ziegler, M. Hempel, and T. Elsaesser, "Mechanisms and fast kinetics of the catastrophic optical damage (COD) in GaAs-based diode lasers," *Laser & Photonics Reviews*, vol. 5, pp. 422–441, mar 2011.

[22] D. Botez, "Design considerations and analytical approximations for high continuous-wave power, broad-waveguide diode lasers," *Applied Physics Letters*, vol. 74, pp. 3102–3104, may 1999.

[23] D. A. Ross, *Optoelectronic Devices and Optical Imaging Techniques*. Macmillan International Higher Education, 1979.

[24] J. Piprek, *Handbook of Optoelectronic Device Modeling and Simulation*. CRC Press, 2017.

[25] JenOptik website: https://www.jenoptik.com/.

[26] J. M. Gilperez, F. Gonzalez-Sanz, E. Calleja, E. Munoz, J. M. Calleja, N. Mestres, J. Castagne, and E. Barbier, "Photoluminescence and raman analysis of strain and composition in InGaAs/AlGaAs pseudomorphic heterostructures," *Semiconductor Science and Technology*, vol. 7, pp. 562–566, apr 1992.

[27] I. Suemune, L. A. Coldren, M. Yamanishi, and Y. Kan, "Extremely wide modulation bandwidth in a low threshold current strained quantum well laser," *Applied Physics Letters*, vol. 53, pp. 1378–1380, oct 1988.

[28] A. Larsson, J. Cody, and R. J. Lang, "Strained-layer InGaAs/GaAs/AlGaAs single quantum well lasers with high internal quantum efficiency," *Applied Physics Letters*, vol. 55, pp. 2268–2270, nov 1989.

[29] E. Yablonovitch and E. Kane, "Band structure engineering of semiconductor lasers for optical communications," *Journal of Lightwave Technology*, vol. 6, no. 8, pp. 1292–1299, 1988.

[30] F. Baiutti, G. Christiani, and G. Logvenov, "Towards precise defect control in layered oxide structures by using oxide molecular beam epitaxy," *Beilstein Journal of Nanotechnology*, vol. 5, pp. 596–602, may 2014.

[31] Wikipedia website: https://en.wikipedia.org/wiki/Metalorganic$_v apour - phase_e pitaxy$.

[32] A. Demir, M. Peters, R. Duesterberg, V. Rossin, and E. Zucker, "Semiconductor laser power enhancement by control of gain and power profiles," *IEEE Photonics Technology Letters*, vol. 27, pp. 2178–2181, oct 2015.

[33] X. Liu, M. Hu, H. Nguyen, C. Caneau, M. Rasmussen, R. Davis, and C.-E. Zah, "Comparison between epi-down and epi-up bonded high-power single-mode 980-nm semiconductor lasers," *IEEE Transactions on Advanced Packaging*, vol. 27, pp. 640–646, nov 2004.

[34] P. Crump, C. M. Schultz, A. Pietrzak, S. Knigge, O. Brox, A. Maaßdorf, F. Bugge, H. Wenzel, and G. Erbert, "975-nm high-power broad area diode lasers optimized for narrow spectral linewidth applications," in *High-Power Diode Laser Technology and Applications VIII* (M. S. Zediker, ed.), SPIE, feb 2010.

[35] T. R. Chen, L. E. Eng, Y. H. Zhuang, and A. Yariv, "Experimental determination of transparency current density and estimation of the threshold current of semiconductor quantum well lasers," *Applied Physics Letters*, vol. 56, pp. 1002–1004, mar 1990.

[36] S. Arslan, S. Gundogdu, A. Demir, and A. Aydinli, "Facet cooling in high power InGaAs/AlGaAs lasers," *IEEE Photonics Technology Letters*, pp. 1–1, 2018.

[37] P. G. Piva, "Reduced 980 nm laser facet absorption by band gap shifted extended cavities," *Journal of Vacuum Science & Technology B: Microelectronics and Nanometer Structures*, vol. 16, p. 1790, jul 1998.

[38] M. Farzaneh, K. Maize, D. Lüerßen, J. A. Summers, P. M. Mayer, P. E. Raad, K. P. Pipe, A. Shakouri, R. J. Ram, and J. A. Hudgings, "CCD-based thermoreflectance microscopy: principles and applications," *Journal of Physics D: Applied Physics*, vol. 42, p. 143001, jun 2009.

[39] J. Michaud, P. D. Vecchio, L. Bechou, D. Veyrie, M. A. Bettiati, F. Laruelle, and S. Grauby, "Precise facet temperature distribution of high- power laser diodes: Unpumped window effect," *IEEE Photonics Technology Letters*, vol. 27, pp. 1002–1005, may 2015.

[40] P. W. Epperlein, G. L. Bona, and P. Roentgen, "Local mirror temperatures of red-emitting (al)GaInP quantum-well laser diodes by raman scattering and reflectance modulation measurements," *Applied Physics Letters*, vol. 60, pp. 680–682, feb 1992.

[41] P. M. Mayer, D. Lüerßen, R. J. Ram, and J. A. Hudgings, "Theoretical and experimental investigation of the thermal resolution and dynamic range of

CCD-based thermoreflectance imaging," *Journal of the Optical Society of America A*, vol. 24, p. 1156, mar 2007.

[42] P.-W. Epperlein, "Micro-temperature measurements on semiconductor laser mirrors by reflectance modulation: A newly developed technique for laser characterization," *Japanese Journal of Applied Physics*, vol. 32, pp. 5514–5522, dec 1993.

[43] S. Arslan, S. Gündoğdu, A. Demir, and A. Aydınlı, "Facet temperature reduction by separate pumped window in high power laser diodes," in *Semiconductor Lasers and Laser Dynamics VIII* (K. Panajotov, M. Sciamanna, and R. Michalzik, eds.), SPIE, may 2018.

[44] J. S. Yu, J. D. Song, Y. T. Lee, and H. Lim, "Influence of dielectric deposition parameters on the in0.2ga0.8as/GaAs quantum well intermixing by impurity-free vacancy disordering," *Journal of Applied Physics*, vol. 92, pp. 1386–1390, aug 2002.

[45] A. Kahraman, E. Gür, and A. Aydınlı, "Impurity-free quantum well intermixing for large optical cavity high-power laser diode structures," *Semiconductor Science and Technology*, vol. 31, p. 085013, jul 2016.

[46] T. Morita, T. Nagakura, K. Torii, M. Takauji, J. Maeda, M. Miyamoto, H. Miyajima, and H. Yoshida, "High-efficient and reliable broad-area laser diodes with a window structure," *IEEE Journal of Selected Topics in Quantum Electronics*, vol. 19, pp. 1502104–1502104, jul 2013.

[47] F. Rinner, J. Rogg, M. T. Kelemen, M. Mikulla, G. Weimann, J. W. Tomm, E. Thamm, and R. Poprawe, "Facet temperature reduction by a current blocking layer at the front facets of high-power InGaAs/AlGaAs lasers," *Journal of Applied Physics*, vol. 93, pp. 1848–1850, feb 2003.

[48] J. Hendrix, G. Morthier, and R. Baets, "Influence of laser parameters and unpumped regions near the facets on the power level for catastrophic optical damage in short wavelength lasers," *IEE Proceedings - Optoelectronics*, vol. 144, pp. 109–114, apr 1997.

[49] P. N. K. Deenapanray, B. Gong, R. N. Lamb, A. Martin, L. Fu, H. H. Tan, and C. Jagadish, "Impurity-free disordering mechanisms in GaAs-based structures using doped spin-on silica layers," *Applied Physics Letters*, vol. 80, pp. 4351–4353, jun 2002.

[50] Z. Qiao, X. Tang, X. Li, B. Bo, X. Gao, Y. Qu, C. Liu, and H. Wang, "Monolithic fabrication of InGaAs/GaAs/AlGaAs multiple wavelength quantum well laser diodes via impurity-free vacancy disordering quantum well intermixing," *IEEE Journal of the Electron Devices Society*, vol. 5, pp. 122–127, mar 2017.

[51] P. N. K. Deenapanray and C. Jagadish, "Effect of stress on impurity-free quantum well intermixing," *Electrochemical and Solid-State Letters*, vol. 4, no. 2, p. G11, 2001.

[52] S. Doshi, P. N. K. Deenapanray, H. H. Tan, and C. Jagadish, "Towards a better understanding of the operative mechanisms underlying impurity-free disordering of GaAs: Effect of stress," *Journal of Vacuum Science & Technology B: Microelectronics and Nanometer Structures*, vol. 21, no. 1, p. 198, 2003.

[53] J. Yu, J. Song, Y. Lee, and H. Lim, "Fabrication of multi-wavelength in0.2ga0.8as/GaAs multiple quantum well laser diodes by area-selective impurity-free vacancy disordering using SiOx capping layers with different stoichiometries," *Applied Physics A*, vol. 80, pp. 847–850, feb 2005.

[54] B. Johs, J. A. Woollam, C. M. Herzinger, J. N. Hilfiker, R. A. Synowicki, and C. L. Bungay, "Overview of variable-angle spectroscopic ellipsometry (VASE): II. advanced applications," in *Optical Metrology: A Critical Review*, SPIE, jul 1999.

[55] H. Fujiwara, *Spectroscopic ellipsometry: principles and applications*. John Wiley Sons, 2007.

[56] S. Arslan, A. Demir, S. Şahin, and A. Aydınlı, "Conservation of quantum efficiency in quantum well intermixing by stress engineering with dielectric

bilayers," *Semiconductor Science and Technology*, vol. 33, p. 025001, jan 2018.

[57] N. Shimada, Y. Fukumoto, H. Uemukai, T. Suhara, H. Nishihara, and A. Larsson, "Monolithic integration of laser and passive elements using selective QW disordering by RTA with SiO/sub 2/ caps of different thicknesses," *IEEE Journal of Selected Topics in Quantum Electronics*, vol. 7, no. 2, pp. 350–354, 2001.

[58] P. L. Gareso, M. Buda, L. Fu, H. H. Tan, and C. Jagadish, "Influence of SiO2 and TiO2 dielectric layers on the atomic intermixing of InxGa1-xAs/InP quantum well structures," *Semiconductor Science and Technology*, vol. 22, pp. 988–992, jul 2007.

[59] A. Pépin, "Evidence of stress dependence in SiO2/si3n4 encapsulation-based layer disordering of GaAs/AlGaAs quantum well heterostructures," *Journal of Vacuum Science & Technology B: Microelectronics and Nanometer Structures*, vol. 15, p. 142, jan 1997.

[60] P. Waters, *Stress Analysis and Mechanical Characterization of Thin Films for Microelectronics and MEMS Applications*. PhD thesis, University of South Florida, 2008.

[61] M. F. M. Costa, "Thin films residual stress measurement by optical profilometry," in *Advanced Photonic Sensors and Applications II*, SPIE, oct 2001.

[62] S. Arslan, S. Sahin, A. Demir, and A. Aydinli, "IFVD-based large intermixing selectivity window process for high power laser diodes," in *Semiconductor Lasers and Laser Dynamics VIII* (K. Panajotov, M. Sciamanna, and R. Michalzik, eds.), SPIE, may 2018.